UNIVERSIDADE FEDERAL DO CEARÁ

CENTRO DE TECNOLOGIA

DEPARTAMENTO DE ENGENHARIA QUÍMICA

PROGRAMA DE PÓS-GRADUAÇÃO EM ENGENHARIA QUÍMICA

MESTRADO EM ENGENHARIA QUÍMICA

JOÃO HENRIQUE BESSA GOMES

A COUPLED GEOMECHANICAL MODEL FOR COMPOSITIONAL RESERVOIR SIMULATION WITH THE FINITE VOLUME METHOD AND UNSTRUCTURED GRIDS

FORTALEZA

2019

JOÃO HENRIQUE BESSA GOMES

A COUPLED GEOMECHANICAL MODEL FOR COMPOSITIONAL RESERVOIR SIMULATION WITH THE FINITE VOLUME METHOD AND UNSTRUCTURED GRIDS

Dissertação apresentada ao Curso de Mestrado em Engenharia Química do Programa de Pós-Graduação em Engenharia Química do Centro de Tecnologia da Universidade Federal do Ceará, como requisito parcial à obtenção do título de mestre em Engenharia Engenharia Química. Área de Concentração: Processos Químicos e Bioquímicos

Orientador: Prof. Dr. Francisco Marcondes

FORTALEZA

2019

Dados Internacionais de Catalogação na Publicação
Universidade Federal do Ceará
Biblioteca Universitária
Gerada automaticamente pelo módulo Catalog, mediante os dados fornecidos pelo(a) autor(a)

G614c Gomes, João Henrique Bessa.
A coupled geomechanical model for compositional reservoir simulation with the finite volume method and unstructured grids / João Henrique Bessa Gomes. – 2019.
96 f. : il. color.

Dissertação (mestrado) – Universidade Federal do Ceará, Centro de Tecnologia, Programa de Pós-Graduação em Engenharia Química, Fortaleza, 2019.
Orientação: Prof. Dr. Francisco Marcondes.

1. Geomechanics. 2. Pore pressure-stress analysis. 3. Geomechanical Coupling. 4. EbFVM. 5. Unstructured Grids. I. Título.

CDD 660

JOÃO HENRIQUE BESSA GOMES

A COUPLED GEOMECHANICAL MODEL FOR COMPOSITIONAL RESERVOIR SIMULATION WITH THE FINITE VOLUME METHOD AND UNSTRUCTURED GRIDS

Dissertation presented to the Masters in Chemical Engineering course of the Graduate Program in Chemical Engineering of the Center of Technology of Federal University of Ceará, as a partial requirement to the obtaining of the title of master in Chemical Engineering. Concentration Area: Chemical and Biochemical Processes.

Approved on: August 29, 2019

EXAMINATION BOARD

Prof. Dr. Francisco Marcondes (Supervisor)
Federal University of Ceará (UFC)

Prof. Dr. Luis Glauber Rodrigues
Federal University of Ceará (UFC)

Prof. Kamy Sepehrnoori, Ph.D.
The University of Texas at Austin

ACKNOWLEDGEMENTS

I would like to thank first and foremost my family, specially my grandmother Francisca Acácio, for the providing me with the conditions to pursue this degree. I have always felt extremely lucky to have such an unconditional support and will always return it in any way I can.

I would also like to thank my girlfriend Marília Candido, for the love, patience and companionship. Words fall short to describe how grateful I am for having such an incredible person in my life.

I am very thankful for all the friendships I have made and maintained throughout the years. They have kept me both grounded and motivated and driven me to be the best I can. Special thanks to: Júnior Paiva, Leonardo Pereira and Marcelo Farias, for the memorable adventures and undying fellowship; to my former colleagues at LDFC, in special to Ivens Costa and Paulo Pimenta, whose contributions and insights were fundamental for the completion of this work; to my colleagues at the Institute of Petroleum and Natural Resources (IPR/PUCRS) for the comprehension and moral support during the making of this work.

I would like to express my gratitude to Prof. Francisco Marcondes, for the supervision and the valuable lessons taught throughout my tenure at LDFC. I would also like to thank the members of the defense and qualification committees: Prof. Luis Glauber Rodrigues, Prof. Kamy Sepehrnoori and Prof. Sebastião Mardônio P. Lucena for the time dedicated and the valuable suggestions that greatly improved the quality of this work.

I would like to acknowledge PETROBRAS S/A for the financial support for this work and to the Center for Petroleum and Geosystems Engineering at The University of Texas at Austin for conceding access to UTCOMP-RS.

This study was financed in part by the Coordenação de Aperfeiçoamento de Pessoal de Nível Superior - Brasil (CAPES) - Finance Code 001.

"It is those who know little, and not those who know much, who so positively assert that this or that problem will never be solved by science."

(Charles Darwin)

RESUMO

A modelagem tradicional de reservatórios de petróleo utiliza um único parâmetro constante, a compressibilidade da formação, para considerar o efeito de adição ou remoção de fluidos dos meios porosos. Essa abordagem tem se mostrado imprecisa na representação da evolução do comportamento estrutural do reservatório durante a injeção ou produção de fluidos, especialmente para formações sensíveis à tensão. O efeito geomecânico em reservatórios é, portanto, um fenômeno mais complexo e que precisa ser analisado minuciosamente. A produção de fluidos do reservatório causa a compactação da formação, a qual irá modificar propriedades, como porosidade e permeabilidade, que são importantes parâmetros nos cálculos de fluxo em meio poroso. O principal objetivo desse trabalho é desenvolver uma solução acoplada entre um simulador composicional de reservatórios e um modelo geomecânico, e aplicá-la a diferentes processos de recuperação de hidrocarbonetos. O simulador de código aberto UTCOMP foi usado para a implementação do modelo geomecânico e acoplamento ao modelo de fluxo. UTCOMP é um simulador composicional de reservatórios baseado em equações de estado desenvolvido pela University of Texas at Austin. A abordagem de discretização usada tanto para o modelo de fluxo quanto para o modelo geomecânico é o Método de Volumes Finitos baseado em Elementos, que permite o uso de malhas não-estruturadas para a representação do domínio físico. A implementação é validada através de problemas com soluções analíticas disponíveis na literatura. Uma vez validado, o simulador acoplado é aplicado a diferentes casos de processos de recuperação de hidrocarbonetos para avaliar as diferenças nos resultados de produção causadas pela inclusão do modelo geomecânico.

Palavras-chave: Análise poroelástica. Acoplamento geomecânico. EbFVM. Malhas não-estruturadas.

ABSTRACT

Traditional petroleum reservoir modeling normally uses a single constant parameter, formation compressibility, to account for the effect of addition or removal of fluid from porous media. This single parameter approach has been shown to inaccurately depict the structural evolution of the reservoir during injection or production of fluids, especially for stress-sensitive formations. The geomechanical effect on the reservoir is therefore a more complex phenomenon that has to be analyzed thoroughly. Reservoir production causes formation compaction, which will modify some of its properties, such as porosity and permeability, that are important parameters for the calculations of fluid flow through porous media. The main objective of this work is to develop a coupled solution between a compositional reservoir simulator and a geomechanical model and apply it to different oil recovery processes. The open-code simulator UTCOMP was used for the implementation of the geomechanical model and its coupling with the reservoir model. UTCOMP is an equation of state compositional reservoir simulator developed by the University of Texas at Austin. The discretization approach used for both the reservoir and the geomechanical models is the Element-based Finite Volume Method, that allows the use of unstructured grids for the representation of the physical domain. The implementation is validated through problems with analytical solution available on the literature. Once validated, the coupled simulator is applied for different cases hydrocarbon recovery processes to evaluate the differences in production results caused by the use of the coupled geomechanical model.

Keywords: Geomechanics. Pore pressure-stress analysis. Geomechanical Coupling. EbFVM. Unstructured Grids.

LIST OF FIGURES

LIST OF TABLES

LIST OF SYMBOLS

a	Peng-Robinson Equation of State parameter
A	Area
b	Peng-Robinson Equation of State parameter
C	Compressibility
D	Reservoir depth
D_{ij}	Elastic properties tensor
E	Young's modulus
f	Fugacity
g	Gravity
G^T	Total Gibbs free energy
$\vec{\vec{k}}$	Absolute permeability tensor
k_{rj}	Relative permeability
MW_i	Molecular Weight
n_p	Number of phases
n_c	Number of hydrocarbon components
N	Shape function
N_i	Number of moles
P	Pressure
P_c	Capillary pressure
$\dot{q}_i$	Component molar flow rate
R	Universal gas constant
S_j	Phase saturation
T	Temperature
t	Time
u_i	Displacement
$\vec{u}_j$	Phase velocity

V_p	Pore volume
V_T	Total fluid volume
WI	Well Index
x_{ij}	Component phase molar fraction
Z	Gas compressibility factor
α	Biot-Willis coefficient
δ_{ij}	Kronecker delta
ε_{ij}	Strain tensor
ε_v	Volumetric strain
η	Transformed plane coordinate
λ_l	Second Lamé's constant
μ_j	Phase viscosity
μ_l	First Lamé's constant
ν	Poisson's ratio
ξ	Transformed plane coordinate
ξ_j	Phase molar density
ρ	Bulk density
ρ_j	Phase mass density
σ_{ij}	Total stress tensor
σ'_{ij}	Effective stress tensor
ϕ	Reservoir porosity
ϕ^*	True porosity
Φ_j	Phase hydraulic potential
ω	Acentric factor

SUMMARY

1 INTRODUCTION

This chapter intends to present an overview of Petroleum Reservoir Engineering and simulation, as well as introducing the importance of geomechanical analysis prior to and during the exploration of field. Furthermore, the main objectives of the work are presented, and a brief outlook on the ensuing chapters is given.

1.1 Reservoir Simulation and Geomechanical Analysis

Petroleum reservoir engineering applies physical, chemical, geological and mathematical principles with the objective of describe, as accurately as possible, the behavior of the reservoir and of the fluids contained in it during the processes of exploration and production of an oil field. Some of the most used tools for these types of studies are reservoir modeling and simulation, which aim to infer the performance of the reservoir based on previously established model. These models are mostly mathematical, more specifically, a set of differential equations capable of describing the fluid flow in porous media and other phenomena occurring in the reservoir (PEACEMAN, 1977).

Reservoir simulation has become a fundamental component in the petroleum industry supply chain, given its precision and the practicality that it provides when observing the influence that parameters, such as well configuration, injection fluid composition and rate, will have on the reservoir production performance, specially when lab tests are not a feasible option. The combination of such parameters determines the production strategy that results in the highest oil recovery possible and, as a consequence, the highest economic return possible.

The evolution of the processing capability of computers enables the development of more robust simulators, that are able to handle more detailed and sophisticated models. Therefore, traditional reservoir models, developed based on a set of limiting assumptions, have been improved and expanded. One of the limitations that have been addressed concerns the geomechanical effects experienced by the reservoir during the injection or production of fluids.

In traditional approaches, the only parameter used to evaluate the effect of addition or removal of fluids in porous media on the rock stress and strain state is the formation compressibility. This parameter describes the variation in pore volume caused by a pressure variation in the reservoir and is normally kept constant during the simulation. Therefore, a linear relation between pore volume variation and pressure is assumed, which not always represent accurately

the real stress and strain behavior.

The geomechanical effect in porous media was first studied by Terzaghi (1923 apud RIBEIRO, 2016), through his soil consolidation theory. According to this theory, there is, in an initial state, mechanical equilibrium established in the porous rock between the force exerted by the rock column weight and the pressure from fluid inside the pores. When the fluid is removed and, therefore, its pressure drops, the rock column weight will act to compact the porous medium. Figure 1 shows a schematic of the effect caused by fluid removal. In the case of a petroleum reservoir, this fluid removal will be represented by hydrocarbon and water production. By modifying the rock structure itself, compaction will be responsible for changes in reservoir properties, most importantly porosity and permeability.

Figure 1 – Geomechanical effect in porous medium

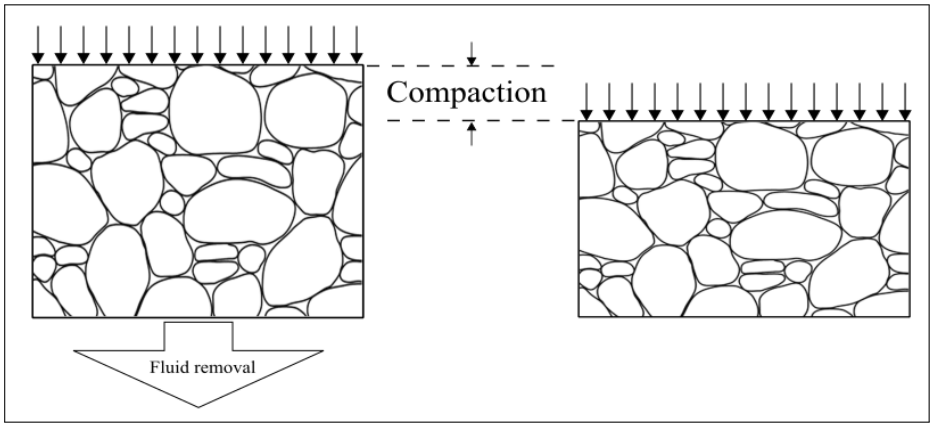

Source: Author.

It is thus evident the coupling that exists between the phenomena of fluid flow in porous media and the geomechanical: fluid production from the reservoir will result in rock compaction, which causes changes in rock properties that are used in the fluid flow calculations. One can infer then that the geomechanical effect will impact, whether positively or negatively, hydrocarbon recovery in reservoirs with a certain degree of stress sensitivity. The positive impact is due to the fact that compaction is also a primary drive mechanism for reservoirs (MUSKAT, 1949). The pores, when compressed, tend to expel part of fluid contained in them towards the well, resulting in a production increase.

The negative impact of the geomechanical effect concerns structural aspects that extend way beyond the reservoir. When rock compaction reaches a high degree, which can be fairly common in soft rocks, subsidence can occur and is represented by the lowering of the surface level. This phenomenon can cause structural damage to surface facilities, platforms and

pipelines, causing operational and environmental hazards. One of the most reported cases of subsidence in literature is the Ekofisk maritime oil field, in Norway (SULAK; DANIELSEN, 1988; HERMANSEN, 1997). In the mid 1980s, subsidence was detected, having reached, in 1984, 10 feet of seabed level lowering. In an effort to avoid the possibility of accidents, the affected platforms were lifted and a water injection operation was started in order to repressurize the compacting formations, delaying the seabed downward displacement. Furthermore, wells in Ekofisk were found with structural damages in their casing and it is believed that these damages were caused by the field subsidence too.

As seen, the geomechanical effect in petroleum reservoir has several consequences on a field productive life, whether it is positively affecting hydrocarbon recovery or causing structural damage that might require a well to be shut down. Therefore, it is necessary to perform a detailed analysis of the stress and strain behavior during the reservoir production. This is done through a coupled solution of the flow model with a geomechanical model capable of calculating stress and strain on the rock. With these data, it is possible to determine changes in porosity and permeability, that, as mentioned previously, will be used for the solution of the flow equations.

1.2 Objectives

The objective of this work is to present a coupled solution between multiphase fluid flow in a porous medium and reservoir geomechanics, with the Element-based Finite Volume Method (EbFVM) as the discretization methodology used for both models, allowing for the same grid to be used for both models. The geometric description of the reservoir will be accomplished with two-dimensional unstructured grids. The implementation of the computational code is to be validated through comparison of its results with those obtained from benchmark cases with an analytical solution. The coupled code will be applied to hydrocarbon recovery processes in order to evaluate the influence of the geomechanical effect on the pressure field and on the recovery itself.

In-house simulator UTCOMP-RS will be used for programming. UTCOMP-RS is a multiphase and multicomponent compositional reservoir simulador developed by the University of Texas at Austin in Fortran programming language (CHANG, 1990). The simulator applies the Finite Volume Method for the discretization of cartesian or corner-point grids and the Element-based Finite Volume Method (EbFVM) for unstructured grids, which are the focus on this work. The coupling between the solutions of the flow and geomechanics models will be of the iterative

type. In this approach, for each time step, there is a convergence loop between the solution of the models, with the update of the coupling parameters for each iteration of the loop.

Simulations will be run on a SGI®cluster in the Laboratory of Computational Fluid Dynamics of Federal University of Ceará. The cluster is composed by 20 nodes, with each having 12 Intel Xeon x5560 processors with 2.8GHz base frequency, adding up to 240 processing cores.

1.3 Overview of this work

Chapter 2 presents a literature review on reservoir simulation and geomechanical coupling, covering since earlier works until most recent developments. The chapter is divided in three sections: geomechanical approach, geomechanics coupling with the reservoir model and numerical approach.

Chapter 3 shows the description of the equations that make up both the reservoir and geomechanical models. For the reservoir compositional model, the material balance equations that lead up to the flow equations are shown, as well as complementary equations, such as Equation of State, permeability models and viscosity models. For the geomechanical model, a similar demonstration is made, based on a force balance to obtain the displacement equations. The coupling method between the flow and geomechanical models is shown in this chapter as well.

Chapter 4 discusses the discretization of the models presented in the previous chapter. The EbFVM discretization approach is detailed and the numerical equations for the flow and geomechanical models are obtained. The numerical coupling methods used in this work are also presented in detail.

Chapter 5 brings the results and its discussion. Initially, the implementation is validated through benchmark cases. Then, case studies are presented for different oil recovery processes, focusing on the influence of the geomechanical effect on the production results.

Chapter 6 presents the conclusions to this work, as well as recommendations for future work.

2 LITERATURE REVIEW

This chapter contains a bibliographic review of the state of the art regarding the fields of study that are encompassed by this work. The chapter is divided in three main sections: geomechanical approach, in which the evolution of the geomechanical description of the reservoir is presented; reservoir and geomechanics coupling, presenting the different ways of coupling the solution of both models; and numerical approach, that focuses on the development of EbFVM and its application with unstructured grids.

2.1 Geomechanical approach

The first theoretical approach developed in an attempt to describe the behavior of porous media under load was done by Terzaghi, as cited in the previous chapter, with the soil consolidation theory. He considered that the particles that compose the soil are bound by molecular interactions, creating a porous medium with elastic properties, and with voids filled with water. Terzaghi (1943) divided soil mechanics problems in two groups: stability problems, that deal with equilibrium conditions for soils immediately before suffering failure by plastic flow; and elasticity problems, that deal with soil deformation caused by the action of either its own weight or external forces. To solve this type of problem, it is mandatory to determine the relationship between stress and strain of the soil.

The biggest contribution of Terzaghi to geomechanics studies was the proposition of the of effective stress law, as an attempt to describe elasticity problems. This law defines effective stress on a porous medium as the difference between the total stress applied on the porous medium and the fluid pressure in the pores. Effective stress, therefore, would represent the fraction of total stress responsible for effects such as compaction on porous medium (TERZAGHI, 1943). Generally, the value for total stress is known in problems, being either kept constant or varying at a known rate. Since pore pressure can be obtained from the flow model solution, effective stress can be calculated. In such fashion, variations in effective stress are responsible for changes in rock properties, mainly porosity and permeability, which, in turn, will affect the fluid flow in the reservoir (PAN, 2009).

This treatment, however, is restricted to one-dimensional problems, since it was developed for the case of a column of water-saturated soil under constant load. Rendulic (1936 apud VERRUIJT, 1969) proposed the first extension of the approach for three-dimensional

situations, considering as time-independent the total stress generated by a constant external load applied to the material. The equation derived was analogue to the three-dimensional heat diffusion equation. This proposition, however, had a more mathematical basis than a physical one.

The extension of Terzaghi's approach was carried out by Biot (1941), by formulating a three-dimensional general consolidation theory. Despite being a more rigorous and in-depth proposition, this theory had limiting assumptions concerning material isotropy, reversibility and linearity of the stress-strain relation, small deformations, incompressible water phase and flow in porous medium described by Darcy's law. These hypotheses, that were also the bases for Terzaghi's theory, were considered by Biot as satisfactory for practical engineering requirements. Resuming the concept of total stress mentioned previously, the full form of the effective stress law can be written, in tensor notation, as:

$$\sigma_{ij} = \sigma'_{ij} - \alpha P \delta_{ij} \tag{2.1}$$

where σ_{ij} is the total stress tensor, σ'_{ij} is the effective stress tensor, P is fluid pressure and δ_{ij} is the Kronecker delta:

$$\delta_{ij} = \begin{cases} 1, & \text{if } i = j \\ 0, & \text{otherwise} \end{cases} \tag{2.2}$$

subscripts i and j represent the tensor components. Constant α is the Biot-Willis coefficient, which represents the fraction of fluid pressure that counterbalances the applied stress and is determined experimentally through compression tests or estimated base on seismic data (BIOT; WILLIS, 1957; CHO *et al.*, 2016). The isotropic material assumption restricted the application of Biot's poroelastic theory, although further developments in subsequent works extended the approach to encompass anisotropic materials and fluid-solid media with non-linear behavior (BIOT, 1955; BIOT, 1956; BIOT, 1962; BIOT, 1973).

The relation between effective stress and strain is given by a constitutive law, that, in a general fashion, can be written as:

$$\sigma'_{ij} = f(\varepsilon_{ij}) \tag{2.3}$$

where ε_{ij} s the strain tensor. The actual equation will depend on the constitutive model assumed for the material, such as linear elastic, non-linear elastic, plastic or viscoplastic (DESAI; SIRI-WARDANE, 1984 apud RIBEIRO, 2016). Strain, in turn, can be expressed as a function of displacement by the kinematic relationship:

$$\varepsilon_{ij} = \frac{\nabla\vec{u} + (\nabla\vec{u})^T}{2} \tag{2.4}$$

where $\vec{u}$ is the displacement vector of the deforming solid.

Several reinterpretations of Biot's theory were presented throughout the years, such as the one by Geerstma (1957), focused on petroleum reservoirs, and Verruijt (1969), concerning aquifers. Ghaboussi and Wilson (1973) proposed one of the first formulations to consider the effect of pore fluid compressibility, enabling the modeling of partially saturated soils, i.e., when the pores are filled in part with air, in part with water. Rice and Cleary (1976) presented a model that fully considered the effect of compressibility of both solid and liquid constituents of the system, also presenting the equations in terms of material parameters with a more accessible physical understanding, like Poisson's ratio.

Small *et al.* (1976) proposed a new consolidation theory in which a elasto-plastic behavior was assumed for the solid medium. According to the authors, the way soil mechanics problems were divided in stability and consolidation problems, as proposed by Terzaghi, is artificial, in a sense that the isolated treatment of problems, by either of two types, can incur in erroneous results for certain situations. The new proposed elasto-plastic theory, therefore, could create ways for a coupled analysis of the plastic yielding and soil consolidation, also enabling studies on time-dependent consolidation. Coussy (1989) presented a consolidation theory based on the thermodynamics of open systems and irreversible processes. The thermal effect due to the fluid contained in the porous medium is taken into account. This model assumes the elasto-plasticity of the solid medium as well as the effects of fluid compressibility.

The development of models that dealt with multiphase flow was fundamental to the application of geomechanical analysis to petroleum reservoir simulation. Tortike and Ali (1987) presented a non-isothermal multiphase flow model for reservoirs under deformation. The development was motivated by the study of steam injection process for oil recovery from bituminous sands in Canada. The simulated model was able to predict stresses and strains associated with steam injection. The calculation of these variables is important to explain the occurrence of supposed errors in material balance calculations and also to determine regions in

the reservoir where there is the possibility of suffering shear failure, a very important information for well design.

Lewis and Sukirman (1993) proposed a model for three-phase immiscible flow in a deforming oil reservoir. The behavior of the solid medium was assumed as elasto-plastic with yielding based on Mohr-Coulomb theory. The model was coupled to a reservoir flow model and the system was solved in a fully implicit approach. The coupled model was tested for different case studies, from which the authors noted the positive effect of reservoir compaction on oil recovery as well as the effect of water flood as a subsidence mitigation mechanism.

2.2 Reservoir and geomechanics coupling

The emergence of models capable of thoroughly describing the geomechanical effect in petroleum reservoir incurred in a search for methodologies for an integrated reservoir analysis. This integration is achieved by coupling the solution of flow in porous media and geomechanical phenomena. The first proposals in this sense presented a rather decoupled solution of the models. Sulak *et al.* (1991) presented the modeling of Ekofisk field compaction. Through a pore pressure history obtained from reservoir simulation, a stress transient solution was calculated. This approach, however, is unpractical, given that two separate simulations are required. A way found to work around this issue, i.e., unifying the simulation, was a fully coupled solution of the models. In this approach, a single linear system encompassing all the equations of both models, would be solved. Examples of this method are found in the previously mentioned works of Tortike and Ali (1987) and Lewis and Sukirman (1993). The development of fully coupled models, however, generally require large programming effort as well as generating high computational loads.

Gutierrez and Lewis (1998) used a fully coupled model to demonstrate the difference in results generated by simulations with and without the geomechanical coupling in terms of pore pressure prediction along the simulation. It was observed the occurrence of the Mandel-Cryer effect, that is characterized by an increase in pore pressure near the reservoir boundaries when the fluid-saturated porous medium is submitted to a load. The pressure increases for a while, then beginning to decrease because of fluid production (CRYER, 1963). This phenomenon is the result of interaction between the reservoir and the sealing rocks surrounding it and also of the difference in physical properties between them. Traditional reservoir simulation cannot predict the Mandel-Cryer effect, due to the use of only the rock compressibility to account for the geomechanical effects.

One of the first alternatives to the fully coupled methodology was proposed by Settari and Mourits (1998), consisting of a iterative coupling. The reservoir and geomechanical modules are run separately, with information exchange between them. The iteration convergence parameters are pressure, calculated in the reservoir module, and porosity, obtained from the geomechanical module. In each time step of the simulation, these parameters are calculated and recalculated until a convergence is reached. The most relevant feature of the iterative coupling is its modularity. Since the reservoir and geomechanical models are treated independently, changes and enhancements to one model would not affect the solution of the other. Apart from that, the iterative approach are robust and also easier to handle in comparison with the fully coupled approach.

One of the main ideas behind modular couplings is that different methodologies could possibly be applied using the same reservoir and geomechanical simulators. The only difference between the methodologies would be in how the two models are interconnected. Settari and Walters (2001) summarized the coupling methods between geomechanics and reservoir in four types:

- Decoupled: only one of the models is solved in the simulation;
- Explicit Coupling: the flow model is solved for pressure, whose value is passed to the geomechanical model, which is solved for stress and strain. This process is carried out only once for each time step. Therefore, the explicit coupling can be seen as a particular case of the iterative coupling;
- Iterative Coupling: as mentioned previously, in each time step, the flow and geomechanical models are solved sequentially until convergence for pressure and porosity is reached;
- Fully Coupled: both models compose a single system to be solved.

In the same work, the authors compared computational performance for explicit, iterative and full couplings for different case studies. They verified that best balance between computational efficiency and results precision was achieved with the explicit approach. The lower computing effort demanded by this methodology is due to the fact that the equations are solved only once for each time step, in comparison with the iterative coupling, that must solve the equations until convergence, and the fully coupled approach, that solves a larger linear system. In turn, the fully coupled methodology obtains exact solutions for the equations, by solving them simultaneously. The iterative coupling can obtain solutions that are almost identical to the exact

ones, depending on the convergence parameters selected, while the explicit approach can yield more imprecision in its solutions.

Subsequent studies brought significant contributions concerning the improvement of coupling techniques and the comparison between them. Chin *et al.* (2002) presented a modified version of the iterative coupling algorithm, in an effort to increase its robustness and computational efficiency. A flow chart of the algorithm is presented in 2.

Figure 2 – Iterative coupling algorithm

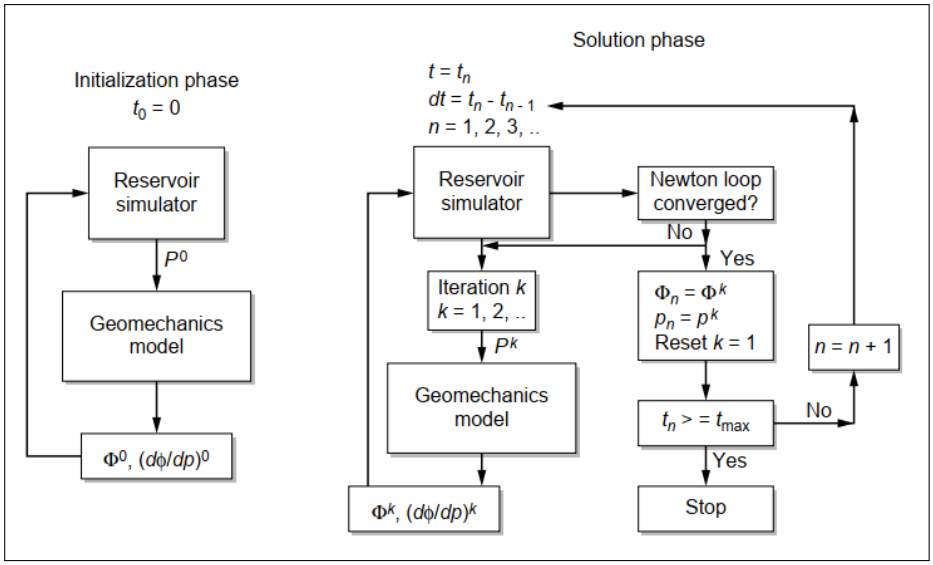

Source: Chin *et al.* (2002).

The authors divided the procedure in two phases. In the initialization phase, which occurs only on the first simulation time step, the geomechanical module will use the initial pressure field to calculate the initial stress state in the reservoir as well as initial values for porosity and its derivative with respect to pressure. Both of these variables are used in the flow model equations. In the solution phase, the process is similar to what was previously described for iterative couplings, having both models solve their equations by the Newton method. The main difference resides in the fact that the Newton iterative loop for the flow model coincides with the coupling iteration loop. In such way, as shown in Fig. 2, for any k coupling iteration, the reservoir module solves its system for the same k iteration of its Newton loop, while the geomechanical model solves its systems until convergence is reached. The procedure continues until the reservoir Newton loop converges. Thus, by sharing the same iteration counter, the convergence of the reservoir model means also the convergence of the coupling. The geomechanical model used in this study was implemented for parallel run, so the computational load was divided for more than one processor, which reduced the simulation time for the geomechanical code in up to 10 times.

Gai (2004) reformulated the iterative coupling methodology between a multiphase black oil simulator and a geomechanical model based on Biot's theory. This new methodology applied preconditioning schemes to the flow model equations to linearize them, in an effort to, according to the author, guarantee a faster convergence. The parallel simulation proposition presented by Chin *et al.* (2002) was extended in this work to both models and for the solvers used in the systems solution, resulting in a significant improvement in simulation performance.

The work by Tran *et al.* (2009) brings a modification to the iterative coupling that allowed the use of dual-grid discretizations, which is when the flow and geomechanical models use different grids. The grid for the geomechanical model tends to cover larger volumes, since it also needs to model the sealing rocks that surround the reservoir. Another feature of the dual-grid approach is the fact that the geomechanical grid can be coarser than the reservoir one, as long as the strains are not extreme. In this case, a mapping algorithm is necessary so the information transfer between models is done correctly. The modification proposed in this work is exactly the mapping between the two grids of output variables of each model. According to the authors, the use of the dual-grid discretization can significantly reduce simulation times in large scale cases.

Pan (2009) presented the implementation of different coupling methodologies for a parallel compositional simulator, specifically the iterative and full couplings, and tested them for several case studies. The results obtained for both couplings were virtually the same. As for simulation times, the iterative approach allowed simulation around 3 times faster than the full coupling, verifying the higher computational effort demanded by the latter method. The author also presented a coupling between the geomechanical model and a dual porosity model developed by Tarahhom (2008), enabling the study of fractured reservoir. In a case study for this situation, it was verified a large impact caused by the addition of the geomechanical analysis in pore pressure prediction and oil recovery.

Tonelli (2016) accomplished a comparison between explicit, iterative and full couplings for a two-dimensional monophase flow. This comparison, carried out in terms of error convergence analysis and simulation time, verified that the errors for the explicit coupling are severely dependent of the time step selected, given the non-iterative aspect of this coupling. In such approach, the non-linearities yielded by the model equations are not properly treated and, in order to obtain an adequate solution, a thorough selection of the time step must be done. For the iterative and full couplings, it was noted that, given the tolerance criteria adopted, both methods produce the same errors and the solutions, differing only in the computing time required.

Simulation times for these methods varied according to the case being studied, such that the author exempted himself from positively stating which coupling approach would be the best, with the problem under study being fundamental for the coupling selection.

The inclusion of fractured reservoir modeling is one of the most covered topics in recent works involving the reservoir and geomechanics coupling (BABAZADEH; MCCLURE, 2015; WANG *et al.*, 2015; LEI *et al.*, 2017; LEE *et al.*, 2017; MORADI *et al.*, 2017). The increasing exploration of unconventional resources, such as shale reservoirs, through hydraulic fracturing, as well as the natural fractures present in part of these reservoirs, bring up the necessity of modeling the stress behavior around the fractures, whose presence in the reservoir requires a different analysis than the one used in conventional reservoirs.

According to Wang *et al.* (2015), the geomechanical effect on rock deformation and on its permeability has a higher impact on the fractures than it has on the rock matrix. In this work, the author presented a fully coupled model capable of modeling a fractured shale gas reservoir. Empirical correlations between effective stress and fracture properties were used in the modeling. In the case studies, it was verified that the closure of the fractures induced by a production-driven change in the reservoir stress state is one the main mechanics responsible for the steep decline in production that has been frequently observed in shale gas reservoirs.

2.3 Numerical approach

One of the fundamental aspects of modeling and simulating physical phenomena, in a general sense, is the choice of numerical methodology to be applied in solving the model equations. Deriving these equations themselves is also a sensible task, since it is necessary to determine a set of limiting assumptions that will depend on the characteristics of the problem being studied. The assumptions adopted can affect the quality and the robustness of the model. In petroleum reservoir modeling, one of the first models developed, the one by Buckley e Leverett (1942), had an analytical solution, although, by considering a linear flow pattern and other limiting assumptions, was rather simple, presenting a low degree of fidelity in the representation of the fluid flow in porous media phenomenon.

Advances in reservoir modeling quality were brought by the proposal of the black oil model (MUSKAT, 1949), in which the three phases assumed are oil, gas and water and their properties are considered as functions of pressure only. Black oil modeling still finds applications in recent modeling works (KHOSHKBARCHI *et al.*, 2015; IOGNA *et al.*, 2017),

although it has not been the main focus, especially after the development of the compositional model. In this formulation, the chemical components of the reservoir fluids are lumped in pseudocomponents for properties calculation. This calculation was initially carried out through fitting of experimental data (ROEBUCK, 1969) or empirical correlations (NOLEN, 1973). It was with the proposed use of equations of state for more precise determination of fluid properties (FUSSELL; FUSSELL, 1979) that the compositional model became prominent, becoming of the most used modeling paradigms for petroleum reservoirs.

Both black oil and compositional models describe the flow in the reservoir through sets of differential equations with the pressure as variable to be solved for. These equations are generally difficult to solve analytically, except in simplified cases, which seldom happens in dealing with realistic models. The alternative to that is to obtain numerical solutions for the problems. The differential equations are discretized, that is, manipulated to become algebraic equations that are solved for discrete portions of the physical domain (PATANKAR, 1980).

The methods traditionally used for numerical solution of differential equations are the Finite Difference Method (FDM), Finite Element Method (FEM) and the Finite Volume Method (FVM). All three approaches have been frequently applied in petroleum reservoir modeling (THOMAS *et al.*, 2003; FERNANDES, 2014; ABUSHAIKHA *et al.*, 2017). FDM was, at an initial moment, widely used in the fluid mechanics field of study, although the difficulty in treating the non-linear terms of the equations has limited the use of this technique to orthogonal systems, such as cartesian, cylindrical and spherical. FEM , in turn, is broadly disseminated for structural and other diffusion-dominated problems. Its standard approximations are based upon the method of weighted residuals and, initially, was not applied to fluid flow phenomena, due to its advection-dominated feature, causing poor stability. The proposal of the Petrov-Galerkin methods were some of the earliest attempt to adequately treat the advective terms of the models. Enhancements and new techniques to accomplish this task have been proposed ever since (ZIENKIEWICZ; TAYLOR, 2000; DONEA; HUERTA, 2003). The main limitation of FEM is not always satisfying conservation principles at a discrete level, which hinders its robustness (MALISKA, 2004).

Limitations presented by both FDM and FEM motivated the use and enhancement of the Finite Volume Method. On FVM, the approximate equations are obtained by conservation balances in control volumes. This conservative feature, that associates a physical interpretation to the problem as well as a mathematical one, has made, according to Maliska (2004), the FVM

stand out in comparison to FDM.

An important development for FVM was the introduction of unstructured grids for discretizing the physical domain of the problem. The work by Baliga and Patankar (1980) introduced a hybrid approach between FVM and FEM. This new methodology combined the concepts of element and shape function, previously intrinsic to FEM, with the conservative feature of FVM, enabling the integration of the equations in control volumes for usntructured grids. The new approach was firstly named Control Volume Finite Element Method (CVFEM). Maliska (2004) suggested renaming the method as Element-based Finite Volume Method (EbFVM), arguing that the new nomenclature better translated the essence of the method, that is a finite volume approach that appropriates itself of some concepts from FEM.

It is necessary now to highlight the difference between structured and unstructured grids. According to Maliska (2004), structured grids are obtained by discretizations that follow global coordinate systems, such as cartesian, and therefore each internal grid volume will have the same number of neighbors. Unstructured grids do not have such restriction, meaning that the number of neighbors of internal volumes can vary. Figure 3 shows examples of structured and unstructured two-dimensional grids. One can infer that unstructured grids are more versatile, being for adequate for modeling irregular geometries, a situation that can occur frequently when dealing with petroleum reservoirs.

Figure 3 – Examples of structured (a) and unstructured (b) grids.

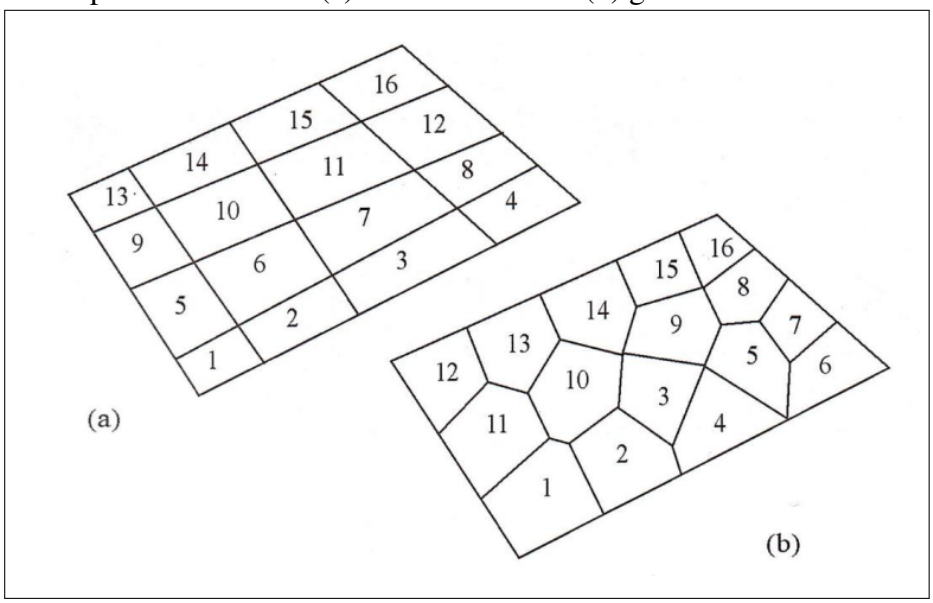

Source: Maliska (2004).

The EbFVM procedure is described by Baliga e Patankar (1980). Initially, the

physical domain of the problem is divided in discrete elements. In the two-dimensional case, the elements can be triangles or quadrilaterals and for the three-dimensional case hexahedrons, tetrahedrons, pyramids and prysms can be used. Each of the elements is then divided in subelements, according to the number of vertices in the element. These subelements are named Subcontrol volume (SCV). The differential equations that model the problem are integrated for each SCV of each element. Then, control volumes are assembled around each vertex in the mesh, by adding up the contribution of each SCV that shares the same vertex.

Since each vertex in the mesh accounts for one control volume, the variables for which the model is being solved, that is, pressure for the reservoir model and displacement for the geomechanical model, are obtained for each vertex (RIBEIRO, 2016). So, the trustworthiness of the results will depend on the mesh refinement, that is, the quantity of elements and vertices present in the mesh. Coarse grids, with few elements, will result in fields of variables that may fail to accurately represent the real behavior in the reservoir. Refined grids will result in more precise results, although a larger computational effort will be required.

One of the earliest applications of EbFVM in reservoir simulation was presented by Rozon (1989), that used the technique to simulate a one-phase model in a two-dimensional grid composed of quadrilateral elements. The study also presents a Taylor series-based comparison of truncation errors between EbFVM and Galerkin method for FEM. It was noted that EbFVM presented smaller truncation errors than the Galerkin formulation, showing its higher precision for the case in study.

Fung *et al.* (1992) proposed the use of EbFVM for triangular elements meshes. The authors based this proposal on the methodology presented by Forsyth (1990), that applied EbFVM to local grid refinements. This feature allowed the precise modeling of geological occurrences in the reservoir, such as faults and pinchouts, proving the EbFVM capability for treating complex geometries.

Cordazzo (2006) simulated a two-phase water-oil flow with EbFVM, using meshes with triangles and quadrilaterals. The multigrid method was implemented to solve the linear systems originated in the discretized equations. It was verified that this solution method presented positive features that would encourage its use in reservoir simulation. Among the features is the linear increase in computational effort caused by the increase in the number of variables, which is not observed in other solution techniques commonly used. The robustness of the multigrid approach was also verified, given the small performance variations suffered by the simulator

when dealing with anisotropic or heterogeneous problems, that generally decrease simulation performance.

Developments in the use of EbFVM for reservoirs with anisotropy or heterogeneity for properties, such as porosity and permeability, were presented by Marcondes and Sepehrnoori (2010) for two-dimensional cases and by Marcondes *et al.* (2013) for three dimensions. In both works, the approach assumed reservoir properties as constant for each element in the mesh, but allowed to vary between elements. For two-dimensional cases, it was verified that EbFVM requires a coarser grid in comparison with traditional FVM, that uses a cartesian grid. The same feature was observed for three-dimensional cases. It was also noted that the numerical error associated with the use of tetrahedral and pyramidal elements was significantly higher than the one associated with hexahedra and prisms.

The aforementioned works discuss an important feature brought by EbFVM that is the attenuation of the grid orientation effects on the simulation results. This phenomenon, as described by Brand *et al.* (1991), concerns the variation on results obtained as the orientation and size of the grid is changed and it can be attributed to a combination of numerical diffusion errors and physical instability of the fluid displacement front in the reservoir. This effect is generally observed in cases in which the mobility ratio between the fluids is high, that is, when one of the fluids encounters less resistance to flow through the pores than the others, whether because it has a higher relative permeability or because it has a lower viscosity. The effect is not entirely dissipated by grid refinement, but is barely present when EbFVM is used, which represents a considerable advantage for this method in reservoir simulation, especially in cases that simulate secondary or enhanced oil recovery, since these processes tend to present high mobility ratios.

Applications of EbFVM are not restricted to traditional reservoirs. Vale (2014) implemented a two-dimensional oil-water model for simulation naturally fractured reservoirs using the discrete fracture model presented by Moinfar *et al.* (2011). This method is based on unstructured grids with local refinement around the fractures, where the porous matrix is modelled three-dimensionally and the fractures are treated as two-dimensional interfaces between neighbour elements in the grid. Apart from maintaining an accurate representation of the fracture network, the methodology also requires a smaller computation time in comparison with other methods for describing fractures, presenting itself as a feasible option also for the study of fractures induced by hydraulic fracturing.

The EbFVM approach has also been used to treat the couple the reservoir and

geomechanical models. Ribeiro (2016) presented a coupled solution for the models, in which both were discretized with EbFVM and a black oil model was used to model the reservoir. Most works that touch this subject use the Finite Element Method to discretize the geomechanical model and another method, such as traditional Finite Volumes, for the flow model (GAI, 2004; PAN, 2009; HADDAD; SEPEHRNOORI, 2017). An unified approach with EbFVM exempt the necessity of interpolations between computational grids, since the same discretization is applied for both models. The work presented an iterative coupling approach and dealt only with two-dimensional cases. The author also compared the unified EbFVM implementation with a methodology that used FEM for the geomechanical model, verifying a similar behavior concerning the numerical error convergence, even though the values between implementations had some discrepancy. This trend ratifies the capacity of EbFVM to proficiently solve not only flow problems, but also structural problems.

The majority of the studies previously presented rely on a dual-grid approach, using a finite volume formulation for the fluid flow model and FEM for the geomechanical model. This approach requires interpolations between the grids, since the variables are calculated in different locations of the grid, that can bring inaccuracy to the coupled solution. Motivated by that, the present work has, as main contribution, the use of the same grid for both models, allowing for more straightforward calculations. Also, the equation-of-state compositional modelling approach used makes up a more realistic evaluation of fluid properties than the alternative black oil model. The following chapters will discuss in detail the derivation of the mathematical and numerical models used for the coupled solution.

3 PHYSICAL MODEL

This chapter presents the physical models that attempt to describe the phenomena of fluid transport through porous media and the geomechanical effect of such transport on the reservoir matrix structure. For the flow model, a pressure equation is obtained, alongside complementary equations for the model, such as an equation of state and calculations of fluid and reservoir properties. For the geomechanical model, a displacement equation is developed from a force balance combined with a constitutive equation. Finally, the coupling between the models is presented, as well as the variables used to properly link the two sets of equations.

3.1 Fluid Flow Model

The task of accurately describing the fluid behavior inside a reservoir is intrinsically complicated, as several chemical components are present in different phases, generally water, oil and gas, distributed in an nonuniform fashion across the porous medium. The rock properties and its interaction with the fluid can also vary through the reservoir. Modeling such a complex phenomenon can only be feasibly accomplished by applying a set of constraints and limiting assumptions that, while simplify the mathematical treatment, do not substantially compromise the accuracy of the results. The fluid flow model used in this work considers the following assumptions, as devised by Chang (1990):

1. Isothermal system;
2. Slightly compressible formation;
3. No fluid flow through reservoir boundaries;
4. No chemical reaction of precipitation occurring;
5. Fluid flow is described by multiphase Darcy's law;
6. Physical dispersion is neglected;
7. Local phase equilibrium;
8. There is a maximum of two hydrocarbon phases in equilibrium.

Four separate phases can coexist simultaneously: water, oil, gas and a second liquid hydrocarbon phase. This additional hydrocarbon phase has been observed in mixtures of CO_2 and hydrocarbons at low temperatures and must be accounted for.

The starting point for obtaining the fluid flow model equations is a material balance for each component that make up the reservoir fluid. After neglecting the physical dispersion

term, the balance results in:

$$\frac{\partial}{\partial t}\left(\phi \sum_{j=2}^{n_p} \xi_j S_j x_{ij}\right) + \vec{\nabla} \cdot \left(\sum_{j=2}^{n_p} \xi_j x_{ij} \vec{u}_j\right) + \frac{\dot{q}_i}{V_b} = 0, \quad i = 1, ..., n_c, \tag{3.1}$$

where ϕ represents reservoir porosity, ξ_j is the phase molar density, S_j is the phase saturation, x_{ij} is the molar fraction of component i in phase j, $\vec{u}_j$ represents the phase velocity vector, q_i is the molar well flow rate of component i, V_b represents the reservoir bulk volume, n_c is the number of components excluding water and n_p is the number of phases. A similar equation is presented for the water phase:

$$\frac{\partial}{\partial t}(\phi \xi_w S_w) + \vec{\nabla} \cdot (\xi_w \vec{u}_w) + \frac{\dot{q_w}}{V_b} = 0, \tag{3.2}$$

where the w subscript denotes the properties are being evaluated for either the water phase or water component. Since the water is not included in any phase equilibrium calculation and there is no mass transfer between hydrocarbon and water phases, the molar fraction of the water component in the water phase is equal to unity.

The expressions denoted by Eqs. (3.1) and (3.2) are classic mass conservation equations. The first term in each of the equations represents the variation of the number of moles of a component with respect to time. For convenience, one can define:

$$N_i = V_b \phi \sum_{j=2}^{n_p} \xi_j S_j x_{ij}, \quad i = 1, ..., n_c, \tag{3.3}$$

$$N_w = V_b \phi \xi_w S_w, \tag{3.4}$$

where N_i and N_w are the number of moles of respectively component i and water. Inserting Eqs. (3.3) and (3.4) into Eqs. (3.1) and (3.2) and manipulating the resulting expression, one can arrive at:

$$\frac{1}{V_b}\frac{\partial N_i}{\partial t} + \vec{\nabla} \cdot \left(\sum_{j=2}^{n_p} \xi_j x_{ij} \vec{u}_j\right) + \frac{\dot{q}_i}{V_b} = 0, \quad i = 1, ..., n_c \tag{3.5}$$

$$\frac{1}{V_b}\frac{\partial N_w}{\partial t} + \vec{\nabla} \cdot (\xi_w \vec{u}_w) + \frac{\dot{q_w}}{V_b} = 0, \tag{3.6}$$

At this point, it is important to remember that the solid matrix is considered to be deforming during the flow of fluids through the porous medium. Therefore, some modifications must be made to the balance equations to account for that. Verruijt (1995) devised an approach with two main changes:

1. true porosity, ϕ^*, is used instead of reservoir porosity, ϕ;
2. Absolute macroscopic superficial fluid phase velocity, $\phi^* S_j \vec{v}^*_{ij}$, with respect to a fixed coordinate system, is used instead of the relative macroscopic Darcy fluid phase velocity, $\vec{v}_j$, with respect to the solid matrix.

In traditional reservoir simulation, since the solid matrix is considered to be static, both absolute and relative fluid phase velocities would be equal, but since the matrix is under deformation, this modification must be made.

So, applying the changes stated above to Eq. (3.5):

$$\frac{1}{V_b}\frac{\partial N_i}{\partial t} + \vec{\nabla}\cdot\left(\sum_{j=2}^{n_p} \xi_j x_{ij} \phi^* S_j \vec{v}^*_{ij}\right) + \frac{\dot{q}_i}{V_b} = 0, \quad i = 1, ..., n_c \tag{3.7}$$

A similar equation is obtained for the water component, but from now on it will be omitted for the sake of brevity.

Velocity $\vec{v}^*_{ij}$ is expressed in terms of component i in phase j. So, by recalling the definition of molar fraction, the absolute macroscopic interstitial velocity of phase j can be expressed by:

$$\vec{v}^*_j = \sum_{i=1}^{n_c} x_{ij} \vec{v}^*_{ij} \tag{3.8}$$

The diffusive-dispersive mass flux of component i in phase j is:

$$\vec{J}_{ij} = \xi_j x_{ij} \phi^* S_j \vec{\tilde{v}}^*_{ij} \tag{3.9}$$

in which $\vec{\tilde{v}}^*_{ij}$ is the macroscopic diffusive-dispersive velocity, defined as:

$$\vec{\tilde{v}}^*_{ij} = \vec{v}^*_{ij} - \vec{v}^*_j. \tag{3.10}$$

Inserting Eqs. (3.9) and (3.10) back into Eq. (3.7) and recalling one of the assumptions for the model that dispersion is neglected, one arrives at:

$$\frac{1}{V_b}\frac{\partial N_i}{\partial t}+\vec{\nabla}\cdot\left(\sum_{j=2}^{n_p}\xi_j x_{ij}\phi^* S_j\vec{v}_j^*\right)+\frac{\dot{q}_i}{V_b}=0,\quad i=1,...,n_c \tag{3.11}$$

The absolute macroscopic interstitial velocity can be written in terms of the solid velocity and the fluid velocity with respect to the solid matrix:

$$\vec{v}_j^*=\vec{v}_s+\vec{v}_{js}^* \tag{3.12}$$

in which $\vec{v}_s$ is the solid matrix velocity and $\vec{v}_{js}^*$ is the interstitial velocity of phase j with respect to the solid matrix. Applying Eq. (3.12) back into Eq. (3.11) results in:

$$\frac{1}{V_b}\frac{\partial N_i}{\partial t}+\vec{\nabla}\cdot\left[\sum_{j=2}^{n_p}\xi_j x_{ij}\phi^* S_j\left(\vec{v}_s+\vec{v}_{js}^*\right)\right]+\frac{\dot{q}_i}{V_b}=0,\quad i=1,...,n_c \tag{3.13}$$

Applying the product rule for derivatives and regrouping terms, the equation above can be restated as:

$$\frac{1}{V_b}\frac{\partial N_i}{\partial t}+\vec{v}_s\vec{\nabla}N_i+N_i\vec{\nabla}\cdot\vec{v}_s+\vec{\nabla}\cdot\left(\sum_{j=2}^{n_p}\xi_j x_{ij}\phi^* S_j\vec{v}_{js}^*\right)+\frac{\dot{q}_i}{V_b}=0,\quad i=1,...,n_c \tag{3.14}$$

Recalling the definition of the material derivative of a function f:

$$\frac{Df}{Dt}=\frac{\partial f}{\partial t}+\vec{v}\cdot\vec{\nabla}f, \tag{3.15}$$

it is clear that the first and second terms of Eq. (3.14) can be grouped into a material derivative, resulting in:

$$\frac{DN_i}{Dt}+V_b\vec{\nabla}\cdot\left(\sum_{j=2}^{n_p}\xi_j x_{ij}\phi^* S_j\vec{v}_{js}^*\right)+V_b N_i\left(\vec{\nabla}\cdot\vec{v}_s\right)+\dot{q}_i=0,\quad i=1,...,n_c \tag{3.16}$$

Velocity $\vec{v}_{js}^*$ can be related to the macroscopic Darcy velocity, $\vec{\tilde{v}}_{js}^*$, with respect to the solid matrix by:

$$\vec{\tilde{v}}_{js}^*=\phi^* S_j\vec{v}_{js}^* \tag{3.17}$$

Equation (3.16) can be rewritten as:

$$\frac{DN_i}{Dt} + V_b \vec{\nabla} \cdot \left(\sum_{j=2}^{n_p} \xi_j x_{ij} \vec{\vec{v}}^*_{js} \right) + V_b N_i \left(\vec{\nabla} \cdot \vec{v}_s \right) + \dot{q}_i = 0, \quad i = 1, ..., n_c \tag{3.18}$$

The term $\left(\vec{\nabla} \cdot \vec{v}_s \right)$ in Eq. (3.18) can be restated in terms of solid matrix volumetric strain, ε_v:

$$\vec{\nabla} \cdot \vec{v}_s = \vec{\nabla} \cdot \frac{D\vec{u}_s}{Dt} = \frac{D\left(\vec{\nabla} \cdot \vec{u}_s \right)}{Dt} = \frac{D\varepsilon_v}{Dt}, \tag{3.19}$$

where $\vec{u}_s$ is the solid displacement. Returning to Eq. (3.18):

$$\frac{DN_i}{Dt} + V_b \vec{\nabla} \cdot \left(\sum_{j=2}^{n_p} \xi_j x_{ij} \vec{\vec{v}}^*_{js} \right) + V_b N_i \frac{D\varepsilon_v}{Dt} + \dot{q}_i = 0, \quad i = 1, ..., n_c \tag{3.20}$$

Further manipulation of the material balance equation will lead to its final form, given by:

$$\frac{D\left[N_i (1 + \varepsilon_v) \right]}{Dt} + V_b \vec{\nabla} \cdot \left(\sum_{j=2}^{n_p} \xi_j x_{ij} \vec{\vec{v}}^*_{js} \right) - V_b \varepsilon_v \frac{DN_i}{Dt} + \dot{q}_i = 0, \quad i = 1, ..., n_c \tag{3.21}$$

Comparing the equation above to its counterparts in traditional reservoir simulators, such as the one presented by Chang (1990), it is easy to notice the influence of the addition of the geomechanical treatment. Equation (3.21) includes an additional term that is function of the volumetric strain, ε_v, and also the solid velocity, $\vec{v}_s$, that is part of the material derivatives.

One of the assumptions of the geomechanical model to be discussed later in this work is the infinitesimal strain theory, in which the displacements and their gradients are very small compared to unity. A consequence of this assumption is that (3.21) can be approximated by neglecting the term $\varepsilon_v \frac{DN_i}{Dt}$.

Another assumption used in the geomechanical model is that the solid velocity is small enough that the material derivatives can be taken as approximately equal to partial derivatives with respect to time and also that Darcy's law is valid for the fluid flow.

Since the true porosity, ϕ^*, is being used in the derivation of the model, one can then define traditional porosity, ϕ, as:

$$\phi = (1 + \varepsilon_v) \phi^* \tag{3.22}$$

When plugging Eq. (3.22) back into (3.21), along with the approximations discussed above, one finally arrives at:

$$\frac{\partial N_i}{\partial t} + V_b \vec{\nabla} \cdot \left(\sum_{j=2}^{n_p} \xi_j x_{ij} \vec{\vec{v}}^*_{js} \right) + \dot{q}_i = 0, \quad i = 1, ..., n_c \tag{3.23}$$

which is similar to the original material balance equation adopted by UTCOMP-RS. This feature allows the geomechanical model to be incorporated into already existing reservoir simulators, requiring small scale modifications to the original code.

As stated in the assumptions adopted for this model, phase velocity $\vec{\vec{v}}^*_{js}$ is calculated by the Darcy's law for multiphase flow and is given by:

$$\vec{\vec{v}}^*_{js} = -\frac{1}{\mu_j} \vec{\vec{k}}_j \cdot \vec{\nabla} \Phi_j, \quad j = 1, ..., n_p \tag{3.24}$$

where μ_j is the viscosity of phase j, $\vec{\vec{k}}_j$ is the effective permeability tensor of phase j and Φ_j is the hydraulic potential of phase j. The expression in Eq. (3.24) can be further expanded by combining it with the definitions of effective permeability and the hydraulic potential, respectively:

$$\vec{\vec{k}}_j = k_{rj} \vec{\vec{k}} \quad j = 1, ..., n_p, \tag{3.25}$$

$$\Phi_j = P_j - \rho_j g D, \quad j = 1, ..., n_p, \tag{3.26}$$

where k_{rj} is the relative permeability of phase j, $\vec{\vec{k}}$ is the formation absolute permeability tensor, P_j denotes the pressure of phase j, ρ_j is the density of phase j and D is the formation depth. When dealing with multiphase systems, in order to properly determine the pressure of each phase, the capillary pressure between phases must be accounted for. Setting the oil phase as reference, the pressure in the remaining phases can be calculated as:

$$P_j = P_r + P_{cjr} \quad j = 1, ..., n_p, \tag{3.27}$$

where P_{cjr} is the capillary pressure between phase j and reference phase r.

The equations shown previously in this section contain variables that require a constraint condition, in order for the equation to be physically correct. The molar compositions for each phase must sum up to the unity, which can be expressed by:

$$\sum_{i=1}^{n_c} x_{ij} = 1 \quad j = 1, ..., n_p. \tag{3.28}$$

A similar constraint is valid for the overall compositions:

$$\sum_{i=1}^{n_c} z_i = 1. \tag{3.29}$$

The phase saturation, by definition, represents the fractional amount of each phase that make up the total fluid volume. Therefore, it also must sum up to the unity:

$$\sum_{j=1}^{n_p} S_j = 1. \tag{3.30}$$

The saturation constraint has an important implication. It means that the entirety of the pore volume, V_p is occupied by the total volume of fluid V_T. Mathematically:

$$dV_p = dV_T. \tag{3.31}$$

Since the system is being considered isothermal, the total volume of fluid is a function only of pressure and of the total number of moles of each component. The total derivative of V_T presented in (3.31) can be written as:

$$dV_T = \left(\frac{\partial V_T}{\partial P}\right)_N dP + \sum_{k=1}^{n_c+1} \left(\frac{\partial V_T}{\partial N_k}\right)_{P,N_{i\neq k}} dN_k. \tag{3.32}$$

The first term in the right hand side of the previous equation is the definition of the total fluid compressibility. The second term is the partial molar volume of the total fluid an from here on, for simplicity, will be denoted as:

$$\left(\frac{\partial V_T}{\partial N_k}\right)_{P,N_{i\neq k}} = \bar{V}_{Tk}. \tag{3.33}$$

The other term related to Eq. (3.31), pore volume, is a function of pressure. So, its total derivative is:

$$dV_p = \frac{\partial V_p}{\partial P} dP. \tag{3.34}$$

The pore volume is, by definition, the product of porosity and reservoir bulk volume, V_b:

$$V_p = \phi^* V_b. \tag{3.35}$$

Inserting Eq. (3.35) back into (3.34):

$$dV_p = V_b \frac{\partial \phi^*}{\partial P} dP. \tag{3.36}$$

Now that expressions for the total derivatives of total volume and pore volume are obtained, they can substituted back in Eq. (3.31) and manipulated resulting in:

$$\left[\frac{\partial \phi^*}{\partial P} - \frac{1}{V_b}\left(\frac{\partial V_T}{\partial P}\right)_{N_k}\right]\frac{\partial P}{\partial t} = \frac{1}{V_b}\sum_{k=1}^{n_c+1}\left(\bar{V}_{tk}\frac{\partial N_k}{\partial t}\right), \tag{3.37}$$

in which the term inside the summation is obtained from the material balance. Finally, by replacing the equations above in (3.37) and manipulating, the final pressure equation is obtained:

$$\begin{aligned}\left[\frac{\partial \phi^*}{\partial P} - \frac{1}{V_b}\left(\frac{\partial V_T}{\partial P}\right)_{N_i}\right]\frac{\partial P}{\partial t} + \bar{V}_{tw}\vec{\nabla}\cdot(\xi_w\vec{u}_w) + \\ \sum_{i=1}^{n_c}\bar{V}_{ti}\sum_{j=2}^{n_p}\vec{\nabla}\cdot\left(\xi_j x_{ij}\vec{v}^*_{js}\right) + \sum_{i=1}^{n_c+1}\bar{V}_{ti}\frac{q_i}{V_b} = 0.\end{aligned} \tag{3.38}$$

While pressure is not explicit in (3.38), it is obtained directly from phase velocity, $\vec{u}_j$, through Eqs. (3.24) and (3.26). It is also worth mentioning that porosity and its derivative will be calculated based on the output of the geomechanical model, as will be shown further in this work.

The set of primary equations to be solved is now complete. However, auxiliary equations are needed to accurately calculate phase behavior and other rock and fluid properties.

Initially, it is necessary to approach the equilibrium considered between hydrocarbon phases. An equilibrium condition is considered to be achieved when the Gibbs free energy is minimum. For a multiphase and multicomponent system, the Gibbs free energy, G^T, can be written as:

$$G^T = \sum_{j=2}^{n_p} \sum_{i=1}^{n_c} n_{ij} \bar{\mu}_{ij}, \tag{3.39}$$

where n_{ij} is number of moles of component i in phase j and $\bar{\mu}_{ij}$ is the chemical potential of component i in phase j and is defined as:

$$\bar{\mu}_{ij} = \bar{\mu}_{ij}^0 + RT \ln \frac{f_{ij}}{f_{ij}^0}, \tag{3.40}$$

where f_{ij} is the fugacity of component i in phase j, $\bar{\mu}_{ij}^0$ and f_{ij}^0 are respectively the chemical potential and fugacity of component i in phase j at a reference state. An useful consideration, that in the reference state the chemical potential is zero and the fugacity is the unity, simplifies the previous equation and, alongside Eq. (3.39), can mathematically represent the state of minimal free energy and, therefore, thermodynamical equilibrium as:

$$\frac{\partial}{\partial n_{ij}} \left(\frac{G^T}{RT} \right) = \ln f_{ij} - \ln f_{ir} = 0, \quad i = 1, ..., n_c, \quad j = 2, ..., n_p \text{ for } j \neq r. \tag{3.41}$$

This equation states that the fugacity of component i in phase j must be equal to the fugacity of the same component in reference phase r. This postulation is also referred to as the isofugacity equilibrium criterion. In the UTCOMP-RS simulator, the oil phase is selected as reference, although choosing any other phase would yield the same result.

With the fluid flow equations laid out and the thermodynamical equilibrium criterion set, the behavior of components and phases must be looked into. The following section presents the equations that model the evolution of equilibrium phase compositions that are used in solving the fluid flow model.

3.2 Phase Behavior

The phase behavior analysis in this work is done through the application of an Equation of State (EoS). The model used in this work was developed by Peng e Robinson (1976)

and is one of the Equations of State implemented into the UTCOMP-RS simulator. Its main expression is given by:

$$P = \frac{RT}{v-b} - \frac{a}{v(v+b)+b(v-b)}, \tag{3.42}$$

in which R is the universal gas constant, v is the molar volume and a and b are equation parameters for pure substance defined by:

$$a = 0.45724\frac{\alpha(RT_c)^2}{P_c}, \tag{3.43}$$

and

$$b = 0.0778\frac{RT_c}{P_c}, \tag{3.44}$$

where

$$\alpha = \left[1 + m\left(1 - \left(\frac{T}{T_c}\right)^{0.5}\right)\right]^2, \tag{3.45}$$

where m is calculated by:

$$m = \begin{cases} 0.37464 + 1.54226\omega - 0.26992\omega^2, & \text{if } \omega \leq 0.49 \\ 0.379642 + 1.48503\omega - 0.164423\omega^2 + 0,016666\omega^3, & \text{if } \omega > 0.49 \end{cases}, \tag{3.46}$$

Alternatively, the Peng-Robinson EoS can be expressed in terms of the gas compressibility factor Z as:

$$Z^3 - (1-B)Z^2 + (A - 3B^2 - 2B)Z - (AB - B^2 - B^3) = 0, \tag{3.47}$$

where

$$A = \frac{aP}{(RT)^2}, \tag{3.48}$$

and

$$B = \frac{bP}{(RT)}, \tag{3.49}$$

In dealing with reservoir fluids, slight modifications to the Equation of State must be done, in order to accommodate for the multiphase, multicomponent system. Therefore, Eqs. (3.42) and (3.47) are modified to:

$$P = \frac{RT}{v_j - b_j} - \frac{a_j}{v_j(v_j + b_j) + b_j(v_j - b_j)}, \quad j = 2, ..., n_p \tag{3.50}$$

and

$$Z_j^3 - (1 - B_j)Z_j^2 + (A_j - 3B_j^2 - 2B_j)Z_j - (A_jB_j - B_j^2 - B_j^3) = 0, \quad j = 2, ..., n_p \tag{3.51}$$

where a_j and b_j are the equation parameters for phase j and are calculated from:

$$a_j = \sum_{i=1}^{n_c} \sum_{k=1}^{n_c} x_{ij} x_{kj} a_{ik}, \quad j = 2, ..., n_p, \tag{3.52}$$

$$b_j = \sum_{i=1}^{n_c} x_{ij} a_i, \quad j = 2, ..., n_p, \tag{3.53}$$

in which

$$a_{ik} = (1 - \kappa_{ik}) (a_i a_k)^{0.5}, \quad j = 1, ..., n_p \tag{3.54}$$

In the equations above, a_i and b_i are the EoS parameters for component i obtained from Eqs. (3.43) and (3.44), respectively; and κ_{ik} is the binary interaction coefficient between components i and k. Coefficients a_j and b_j are also used to determine A_j and B_j from (3.51).

3.3 Physical Properties

This section aims to present the equations used to model the main physical properties that make up the fluid flow model. In the following subsections, models for relative permeability, fluid viscosity and well flow rate are presented. All these variables are present in the pressure equation, Eq. (3.38), and are fundamental for the accurate description of the fluid flow.

3.3.1 Relative Permeability

Although UTCOMP-RS has several relative permeability model options available, only the modified Stone II model (STONE, 1973) is used in this work. For two-phase flow, e.g. water and oil, the relative permeability of each phase is given by

$$k_{rw} = k_{rw}^0 \left(\frac{S_w - S_{wr}}{1 - S_{wr} - S_{or}} \right)^{e_w}, \tag{3.55}$$

$$k_{ro} = k_{ro}^0 \left(\frac{S_o - S_{or}}{1 - S_{wr} - S_{or}} \right)^{e_o}, \tag{3.56}$$

where k_r^0 is the end-point relative permeability, S_r is the residual saturation and e is a model parameter. The subscripts o and w refer respectively to the oil and water phases.

For a three-phase system (oil, water and gas), the relative permeability of each phase is calculated by

$$k_{rw} = k_{rw}^0 \left(\frac{S_w - S_{wr}}{1 - S_{wr} - S_{orw}} \right)^{e_w}, \tag{3.57}$$

$$k_{rg} = k_{rg}^0 \left(\frac{S_g - S_{gr}}{1 - S_{gr} - S_{wr} - S_{org}} \right)^{e_g}, \tag{3.58}$$

$$k_{ro} = k_{row}^0 \left[\left(\frac{k_{row}}{k_{row}^0} + k_{rw} \right) \left(\frac{k_{rog}}{k_{row}^0} + k_{rg} \right) - (k_{rw} + k_{rg}) \right], \tag{3.59}$$

where k_{row}^0 is the end-point relative permeability for oil in water, and S_{orw} and S_{org} are the residual oil saturations in water and gas, respectively. The relative permeabilities of oil in water and in gas are respectively given by

$$k_{row} = k_{row}^0 \left(\frac{1 - S_w - S_{orw}}{1 - S_{wr} - S_{orw}} \right)^{e_{ow}}, \tag{3.60}$$

$$k_{rog} = k_{rog}^0 \left(\frac{1 - S_g - S_{wr} - S_{org}}{1 - S_{gr} - S_{wr} - S_{org}} \right)^{e_{og}}, \tag{3.61}$$

3.3.2 Viscosity

UTCOMP-RS has multiple methods for estimation of phase viscosities, but only the one presented by Lohrenz *et al.* (1964) is used in this work. Initially, it is necessary to evaluate the low-pressure, pure component viscosity, $\bar{\mu}_i$, according to

$$\begin{cases} \bar{\mu}_i = \frac{3.4\times10^{-4}T_{r,i}^{0.94}}{\zeta_i}, \quad i=1,...,n_c, & \text{for } T_{r,i} \leq 0.15 \\ \\ \bar{\mu}_i = \frac{1.776\times10^{-4}(4.58T_{r,i}-1.67)^{5/8}}{\zeta_i}, \quad i=1,...,n_c, & \text{for } T_{r,i} > 0.15, \end{cases} \tag{3.62}$$

in which $T_{r,i}$ is the reduced temperature of component i and ζ_i is a parameter defined by:

$$\zeta_i = \frac{5.44T_{c,i}^{1/6}}{MW_i^{1/2}P_c^{2/3}}, \quad i=1,...,n_c \tag{3.63}$$

Then, the low-pressure mixture viscosity, μ_j^* is determined via mixing rule:

$$\mu_j^* = \frac{\sum_{i=1}^{n_c} x_{ij}\bar{\mu}_i\sqrt{MW_i}}{\sum_{i=1}^{n_c} x_{ij}\sqrt{MW_i}}, \quad j=1,...,n_p \tag{3.64}$$

Finally, the viscosities at phase pressure are calculated:

$$\begin{cases} \mu_j = \mu_j^* + 2.5\times10^{-4}\frac{\xi_{jr}}{\eta_j}, \quad j=1,...,n_p, & \text{for } \xi_{jr} \leq 0.18 \\ \\ \mu_j = \frac{\mu_j^* + (\chi_j^4-1)}{10^4\eta_j}, \quad j=1,...,n_p, & \text{for } \xi_{jr} > 0.18 \end{cases} \tag{3.65}$$

where ξ_{jr} is the reduced molar density of phase j and η_j and χ_j are equation parameters. The three terms are determined by:

$$\xi_{jr} = \xi_j \sum_{i=1}^{n_c} x_{ij}V_{c,i} \tag{3.66}$$

$$\eta_j = 5.44\left(\sum_{i=1}^{n_c} x_{ij}T_{c,i}\right)^{1/6}\left(\sum_{i=1}^{n_c} x_{ij}W_i\right)^{-1/2}\left(\sum_{i=1}^{n_c} x_{ij}P_{c,i}\right)^{-2/3}, \quad j=1,...,n_p \tag{3.67}$$

$$\chi_j = 1.023, 0.23364\xi_{jr} + 0.58533\xi_{jr}^2 - 0.40758\xi_{jr}^3 + 0.093324\xi_{jr}^4, \quad j=1,...,n_p \tag{3.68}$$

3.3.3 Well Term

The well flow rates term present in the pressure equation, Eq. (3.38), requires a nuanced evaluation, given the natural complexity of the phenomenon involving the well flow from and into the porous media. For this work, the Well Index (WI) approach, as presented by Peaceman (1978) and Peaceman (1983) for cartesian grids, and later adapted to unstructured grids by Fung *et al.* (1992).

WI is defined as:

$$WI_j = \frac{\dot{q}_j}{P_w - P_j}, \quad j = 1, ..., n_p, \tag{3.69}$$

where P_w is the well pressure at the point of calculation. As proposed by Fung *et al.* (1992), WI can be calculated by

$$WI_j = \frac{2\pi\sqrt{k_x k_y}hf}{\ln(r_o/r_w)} \tag{3.70}$$

in which h is control volume thickness, f is the fraction of the well open to the reservoir, r_w is the well radius and r_o is the equivalent radius of the control volume, which is defined as the radius at which well flowing pressure is equal to the calculated pressure of the well control volume. Further calculations can be found in Fung *et al.* (1992).

As far as operational conditions are concerned, this work deals with both injection and production wells. Injection wells are treated as a constant surface volume regime with component volumetric flow rates calculated at surface conditions. These are calculated per well segment by:

$$\dot{q}_{k,s} = \frac{WI_s \sum_{j=1}^{n_p} \lambda_{j,s}}{\sum_{l=1}^{n_s} WI_l \sum_{j=1}^{n_p} \lambda_{j,l}} \dot{q}_{k,T}, \quad s = 1, ..., n_s, \quad , k = 1, ..., n_p \tag{3.71}$$

where the subscript s refers to the well segment at which the calculation is being done, n_s is the total number of well segments, $\dot{q}_{k,T}$ is the total molar flow rate for the well and $\lambda_{j,s}$ is the mobility of phase j. The mobility of a phase is defined as the ratio between relative permeability and viscosity, so

$$\lambda_j = \frac{k_{rj}}{\mu_j}. \tag{3.72}$$

Also, the phase volumetric flow rates, $\dot{Q}_{j,s}$, can be calculated by

$$\dot{Q}_{j,s} = \lambda_{j,s} WI_s \left(P_{j,s} - P_{w,s}\right), \quad s = 1,...,n_s, \quad ,k = 1,...,n_p \tag{3.73}$$

Production wells, in turn, are only considered under the constant bottom-hole pressure condition. In this case, the molar flow rates for each well segment is given by

$$\dot{q}_{k,s} = \sum_{j=2}^{n_p} x_{kj,s} \xi_{j,s} \dot{Q}_{j,s}, \quad s = 1,...,n_s, \quad ,k = 1,...,n_p \tag{3.74}$$

$$\dot{q}_{w,s} = \xi_{w,s} \dot{Q}_{w,s}, \tag{3.75}$$

respectively for hydrocarbon components and water. The volumetric flow rates are also calculated by Eq. (3.73).

3.4 Geomechanical Model

After the full description of the fluid flow model, this section aims to present the full scope of the model used to evaluate the geomechanical interactions in the reservoir. Similarly as seen with the fluid flow model, the accurate description of the mechanical evolution of reservoir rocks can be a complicated task, given the intrinsic nature of the phenomenon. Therefore, it is necessary to come up with a set of constraints, so the solution of the final equations is feasible, while not giving up on much of the accuracy. As stated by Pan (2009), the assumptions adopted for the geomechanical are as follows:

1. The infinitesimal strain theory is applied, meaning that the absolute values of displacement and its gradients are small compared to unity;
2. The solid matrix is considered an isotropic medium;
3. The stress-strain relation is linear and reversible;
4. The solid particles are incompressible, meaning that the deformation of the reservoir is a consequence solely of the rearrangement of the solid particles, and not by their compression. A natural consequence of this assumption is that the solid grain density is constant, even though the medium is experiencing compression;
5. The solid velocity is negligibly small, meaning that Darcy's law is still valid for the fluid flow.

The last two assumptions were previously discussed during the derivation of the material balance equation for the coupled model and are also substantial for obtaining the equations for the geomechanical model.

The starting point for obtaining the model is to perform a linear momentum balance on a discrete control volume in the reservoir. The balance, readopting tensor notation, reads as

$$\nabla \cdot \sigma_{ij} + \rho g_i = 0, \tag{3.76}$$

in which ρ is the bulk density of the control volume and g_i is the gravity acceleration vector. The bulk density is function of both the fluid and solid densities and is given by

$$\rho = \phi^* \rho_f + (1 - \phi^*)\rho_s, \tag{3.77}$$

where ρ_f and ρ_s are respectively the fluid and the solid matrix densities.

The terms in the right-hand side of Eq. (3.76) represent, in order, the force applied to the control volume and its body forces. The applied load term can be expanded by recalling the effective stress law, Eq. (2.1), resulting in

$$\nabla \cdot \left(\sigma'_{ij} - \alpha P \delta_{ij}\right) + \rho g_i = 0. \tag{3.78}$$

It is important to state that the sign convention adopted for this work is of positive stresses for tension and negative stresses for compression.

Equation (3.78) is an important first step for deriving a geomechanical model, but not enough in terms of mechanical description of the solid matrix. According to the assumptions for this formulation, a linear stress-strain relationship is considered, meaning that the effective stress experienced by the rock will always yield a linearly proportional strain as response. The proportionality constant for the relationship is the Young's modulus, E, and is a property of the rock. Mathematically,

$$E = \frac{\sigma'_{ij}}{\varepsilon_{ij}}. \tag{3.79}$$

The behavior described in Eq. (3.79) is similar to the one described by Hooke's law for springs under load. While this approach means a significant simplification of an intrinsically

complex process, as Zoback (2007) argues, the use of a linear relationship for well-cemented rocks is still accurate enough in representing the rock behavior until its failure. For less consolidated solid matrices, however, the non-linearities are more apparent and the use of a linear constitutive relationship is not recommended.

Several non-linear relationships have been developed over the year to attempt to describe the non-linear behavior of reservoir rocks, focusing mainly in two tasks. The first is to determine at which moment the irreversible plastic deformation begins and second is to describe the behavior of this plastic deformation. Among the several non-linear models, the criteria most used for reservoir rocks include Mohr-Coulomb, Tresca (1864), Drucker e Prager (1952) and Mises (1913). The work of Souza Neto *et al.* (2008) brings a thorough discussion of these criteria. In this work, however, the focus will be solely the linear elastic constitutive relationship. Therefore, for a plane strain formulation, Eq. (3.79) can be expressed in a different fashion by

$$\sigma'_{ij} = 2\mu_l \varepsilon_{ij} + \lambda_l \mathrm{tr}(\varepsilon_{ij})\delta_{ij}, \tag{3.80}$$

where μ_l and λ_l are respectively the first and second Lamé's constants and tr$(\cdot)$ represents the trace operator of a tensor. The Lamé's constants are defined in terms of Young's modulus, E, and Poisson's ratio, ν, by

$$\mu_l = \frac{E}{2(1+\nu)}, \tag{3.81}$$

and

$$\lambda_l = \frac{E\nu}{(1+\nu)(1-2\nu)}, \tag{3.82}$$

,

also relating to each other through

$$\mu_l = \frac{\lambda_l(1-2\nu)}{2\nu}. \tag{3.83}$$

The first constant, μ_l, is also referred to as shear modulus, G, and represents the stiffness of a material when submitted to shear stresses. The second constant, λ_l, does not have a direct physical representation.

With the stress-strain relationship well defined, it is necessary to specify the relation between the strain tensor and the displacement vector. Considering the assumptions made for infinitesimal strains and incompressible solid grain, a kinematic relation arises as

$$\varepsilon_{ij} = \frac{1}{2}\left(\frac{\partial u_i}{\partial x_j} + \frac{\partial u_j}{\partial x_i}\right). \tag{3.84}$$

Equation (3.84) represents the final step in assembling the equations for the geomechanical model. This equation is substituted back into the constitutive equation, Eq. (3.80), and its result is then plugged into the linear momentum balance equation, Eq. (3.78), resulting in an equation with displacement as the variable to be solved for. Doing the procedure above, the equation obtained is given by:

$$\nabla \cdot \left[\mu_l \left(\frac{\partial u_i}{\partial x_j} + \frac{\partial u_j}{\partial x_i}\right) + \lambda_l \mathrm{tr}(\varepsilon_{ij})\delta_{ij} - \alpha P \delta_{ij}\right] + \rho g_i = 0. \tag{3.85}$$

By integrating it and finding the solution for displacement, it is then possible to calculate strain and stress from Eqs. (3.84) and (3.80).

3.5 Coupled Model

In laying out the reservoir and geomechanical models in the previous sections, it is clear that the equations for both models have terms that depend on each other and, therefore, must be coupled. The pressure equation, Eq. (3.38), depends on porosity, which naturally will vary as the deformation on the solid matrix causes the grains to rearrange. The relation between true porosity and deformation can be quantified, according to Chin *et al.* (2002), as

$$\phi^* = 1 - (1 - \phi_o)e^{-\varepsilon_v}, \tag{3.86}$$

in which ϕ_o is the initial porosity and the volumetric strain, ε_v, is equal to trace of the strain tensor

$$\varepsilon_v = \mathrm{tr}(\varepsilon_{ij}) = \varepsilon_{ii}, \tag{3.87}$$

where the last term means, in tensor notation, the summation of all terms of the main diagonal of tensor ε_{ij}. Along with the variation in porosity, the changes in the mechanical state of the

reservoir can also cause variations in permeability. Its behavior, however, can be affected by several different parameters, such as pore pressure, porosity, effective mean normal stresses, effective shear stresses and normal strain (CHIN *et al.*, 1998b), making it difficult to obtain an equation that aggregates all these parameters. A power-law model (CHIN *et al.*, 1998a; CHIN *et al.*, 1998b) has been shown to be satisfactory in predicting the behavior of permeability. The equation is given by

$$\frac{k}{k_o} = \left(\frac{\phi^*}{\phi_o^*}\right)^n, \tag{3.88}$$

in which the subscript o refers to the initial values of either porosity or permeability and n is an empirical exponent determined from experimental data. By definition, the rock compressibility is also a function of porosity and could also be used as a coupling parameter, but this approach, while possible, is not pursued in this work.

For the geomechanical model, Eqs. (3.78), (3.80) and (3.84), the pore pressure calculated from the fluid flow model is used as an input parameter, reinforcing the coupled nature of the models. The main coupling variables are pore pressure, output from the fluid flow model and input into the geomechanical model, and porosity, output from the geomechanical model and input back into the fluid flow model. Further in this work, the approaches used to link the solution of both models will be discussed in detail.

4 NUMERICAL MODEL

The mathematical models for fluid flow model and the geomechanical model were presented in detail in Chapter 3. They represent a set of partial differential equations being also strongly non-linear, considering the coupling between models. Therefore, the task to solve these equations analytically is often unfeasible, leading to a numerical solution as the most efficient method. In this work, both models are discretized through the Element-based Finite Volume Method (EbFVM), which, as discussed in Chapter 2, is at its core a Finite Volume formulation, but also aggregates some concepts from the Finite Element Method. This chapter will first present the fundamentals of EbFVM and then discuss the details of the discretization of both the fluid flow model and the geomechanical model. Finally, the chapter will also discuss the coupling approaches most used to associate the solutions of the two models.

4.1 EbFVM Approach

As previously discussed, the Element-based Finite Volume Method (EbFVM) is an extension of the traditional Finite Volume Method that applies concepts from the Finite Element Method to allow for more flexibility in terms of gridding without losing the conservative attribute of traditional method. EbFVM accepts the use of unstructured grids, such as the one depicted in Figure 4. It is comprised of eight vertices, numbered in black, that connect to form five elements, numbered in red, between triangles and quadrilaterals. In three-dimensional grids, the possible element types are hexahedrons, tetrahedrons, prisms and pyramids.

In order to form the control volumes in EbFVM, the grid elements are first subdivided in sub-control volumes (SCVs), as Figure 5 shows. The number of SCVs of each element is proportional to the number of vertices that element has. The control volume for each vertex is then formed by combining the SCVs that belong to that same vertex. The procedure is illustrated in Figure 5. In order to assemble the control volume around vertex 3, one must sum the contributions of all SCVs around this vertex, namely, SCV 3 from element 1, SCV 2 from element 4, SCV 1 from element 3, SCV 1 from element 5 and SCV 2 from element 2. These subelements are colored in Figure 5.

The differential equations from both the fluid flow and geomechanical models are integrated in each SCV. Therefore, the algebraic equations to be solved for each vertex are composed by summing the contributions of each SCV that makes up its control volume.

Figure 4 – Sample two-dimensional unstructured grid.

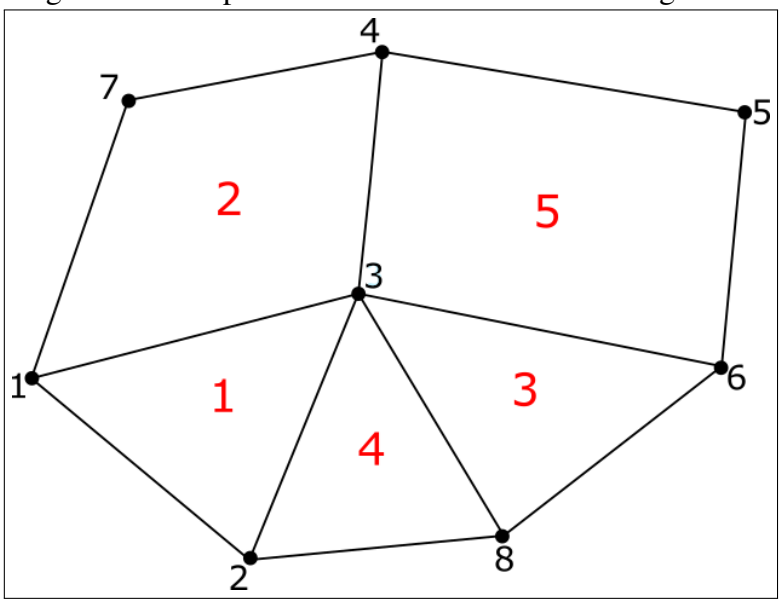

Source: Prepared by the author.

Figure 5 – Sample two-dimensional unstructured grid with control volume highlighted.

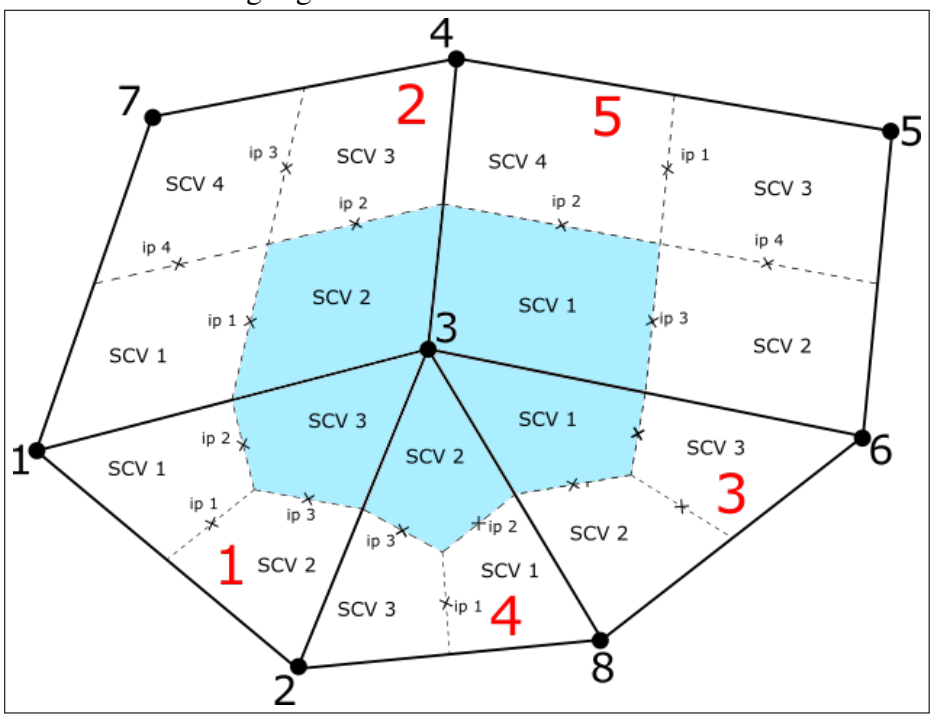

Source: Prepared by the author.

The elements and its SCVs shown in 5 have some degree of distortion. In fact, there is no limit to this distortion, which can appear depending on the physical features of the domain and the grid generation algorithm used. However, in practical terms, it is advised to avoid elements with extremely sharp angles, as numerical divergences might arise. The reason that distortions are allowed is that the calculations are not done on the physical plane that has

been presented until now, but rather on a transformed plane in each all elements have the same dimensions and have no distortions. The relationship between the elements on the physical plane and its transformed version is given by shape functions, N. In a two-dimensional case, for triangle elements, the shape functions are defined by:

$$N_1(\xi,\eta) = 1-\xi-\eta; \quad N_2(\xi,\eta) = \xi; \quad N_3(\xi,\eta) = \eta, \tag{4.1}$$

and for quadrilaterals,

$$\begin{aligned} N_1(\xi,\eta) &= \frac{1}{4}(1-\xi)(1-\eta); \quad N_2(\xi,\eta) = \frac{1}{4}(1+\xi)(1-\eta); \\ N_3(\xi,\eta) &= \frac{1}{4}(1+\xi)(1+\eta); \quad N_4(\xi,\eta) = \frac{1}{4}(1-\xi)(1+\eta); \quad , \end{aligned} \tag{4.2}$$

where ξ and η are the coordinates for the transformed plane. A visual comparison between the elements in the physical and transformed planes is shown in Figure 6.

Figure 6 – Two-dimensional elements in the physical and transformed planes. (a) Triangle element; (b) Quadrilateral element.

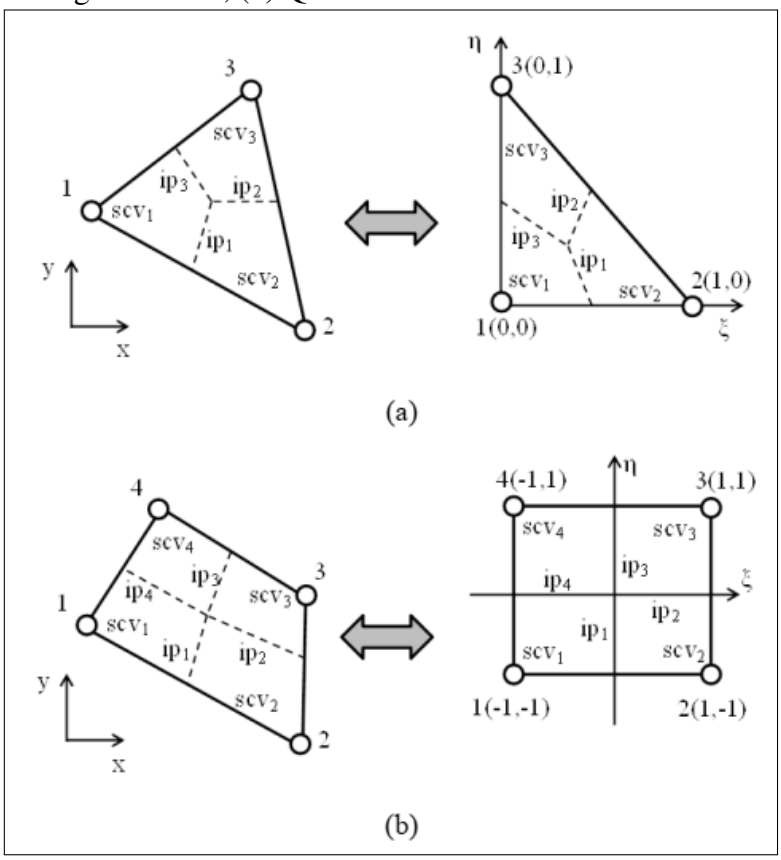

Source: Fernandes (2014).

The shape functions are also used to interpolate any property, or its gradient, inside an element. Supposing an arbitrary function ϕ, its value at any coordinate pair (ξ, η) inside the transformed element can be evaluated by

$$\phi(\xi,\eta) = \sum_{i=1}^{n_v} N_i(\xi,\eta)\Phi_i, \tag{4.3}$$

where n_v is the number of vertices of the element and Φ_i is the value of the property evaluated at the vertices. Gradients of function ϕ are given by

$$\frac{\partial \phi(\xi,\eta)}{\partial x_j} = \sum_{i=1}^{n_v} \frac{N_i}{\partial x_j}\Phi_i, \tag{4.4}$$

where the derivatives of the shape functions with respect to the coordinates are given by

$$\frac{\partial N_i}{\partial x} = \frac{1}{\det(J)}\left(\frac{\partial y}{\partial \eta}\frac{\partial N_i}{\partial \xi} - \frac{\partial y}{\partial \xi}\frac{\partial N_i}{\partial \eta}\right); \quad \frac{\partial N_i}{\partial y} = \frac{1}{\det(J)}\left(\frac{\partial x}{\partial \xi}\frac{\partial N_i}{\partial \eta} - \frac{\partial x}{\partial \eta}\frac{\partial N_i}{\partial \xi}\right), \tag{4.5}$$

where $\det(J)$ is the determinant of the coordinate transformation matrix and is calculated by

$$\det(J) = \frac{\partial x}{\partial \xi}\frac{\partial N_i}{\partial \eta} - \frac{\partial x}{\partial \eta}\frac{\partial N_i}{\partial \xi}. \tag{4.6}$$

In Figure 6, the indication *ip* refers to the integration points, the midpoint of the interfaces between SCVs inside a single element. These interfaces are also represented in Figure 5 by dashed lines and also make up the interface between neighboring control volumes. Therefore, when integrating the equations for each control volume, the flux terms of the model equations must be evaluated at the integration point. To do that, it is necessary to define the area through which the flux will happen. Assuming h as the element cross-sectional thickness, the flux interface area is given by

$$d\vec{A} = h(dy\hat{i} - dx\hat{j}). \tag{4.7}$$

Now that the EbFVM discretization approach has been described in detail, it is time to present the discrete versions of the mathematical models presented in the previous chapter. The equations are to be integrated in a SCV level and summed up to form the equation for each control volume, as previously described.

4.2 Discretized Fluid Flow Equations

This section concerns the integration of the material balance and pressure equations of the fluid flow model, specifically Eqs. (3.23) and (3.38), respectively the material balance and pressure equations. As previously stated, the equations will be integrated over each sub-control volume (SCV) and over time, in order to obtain the equations for each control volume. So, by doing just that to the material balance equation, Eq.(3.23):

$$\int_t \int_{SCV} \frac{\partial N_i}{\partial t} dV dt + \int_t \int_{SCV} V_b \vec{\nabla} \cdot \left(\sum_{j=2}^{n_p} \xi_j x_{ij} \vec{v}^*_{js} \right) dV dt + \int_t \int_{SCV} \dot{q}_i dV dt = 0, \quad i = 1, ..., n_c. \tag{4.8}$$

Applying Gauss's theorem to the second integral term,

$$\int_t \int_{SCV} \frac{\partial N_i}{\partial t} dV dt + \int_t \int_A V_b \vec{\nabla} \cdot \left(\sum_{j=2}^{n_p} \xi_j x_{ij} \vec{v}^*_{js} \right) d\vec{A} dt + \int_t \int_{SCV} \dot{q}_i dV dt = 0, \quad i = 1, ..., n_c. \tag{4.9}$$

The term in which the theorem was applied is a flux term, as the fluid phase velocity, $\vec{v}^*_{js}$, is present in the equation. The importance of this step lies in the fact that now the fluxes can be evaluated at the SCV interfaces, i.e., integration points, whose areas are known from Eq. (4.7). Performing the integration of Eq. (4.9), the final discretized equation assumes the following general form:

$$Acc_{i,k} - F_{i,k} + S_{i,k} = 0, \quad i = 1, ..., n_c \quad k = 1, ..., n_v, \tag{4.10}$$

in which $Acc_{i,k}$ is the accumulation term, $F_{i,k}$ is the net advective flux term and $S_{i,k}$ is source term. The expressions for each term are given by

$$Acc_{i,k} = \frac{V_{scv,k}}{V_{b,k}} \left(N^{n+1}_{i,k} - N^n_{i,k} \right), \quad i = 1, ..., n_c \quad k = 1, ..., n_v, \tag{4.11}$$

$$F_{i,k} = \Delta t \int_A \sum_{j=2}^{n_p} \xi^m_j x^m_{ij} \frac{k^m_{rj}}{\mu^m_j} \vec{\vec{k}} \cdot \vec{\nabla} \Phi^m_j \cdot d\vec{A}_k, \quad i = 1, ..., n_c \quad k = 1, ..., n_v, \tag{4.12}$$

$$S_{i,k} = \Delta t \frac{V_{scv,k}}{V_{b,k}} \dot{q}_{i,k}, \quad i = 1, ..., n_c \quad k = 1, ..., n_v, \tag{4.13}$$

where n and $n+1$ denote the previous and current time steps, respectively. It is still necessary to evaluate the integral and gradient terms in Eq. (4.12). For the surface integral, a plausible approximation is to consider it as the sum of the integrating terms across all integration points in the control volume. Since these points are located at the center of each interface, as previously defined, the flux properties are also evaluated at the integration points. Hence,

$$F_{i,k} = \Delta t \sum_{l=1}^{n_{ip}} \sum_{j=2}^{n_p} \left[\xi_j^m x_{ij}^m \frac{k_{rj}^m}{\mu_j^m} \vec{k} \cdot \vec{\nabla} \Phi_j^m \cdot d\vec{A}_k \right]_l, \quad i = 1, ..., n_c \quad k = 1, ..., n_v, \tag{4.14}$$

in which n_{ip} denotes the number of integration points of each SCV. The gradient term of Eq. (4.12) can be manipulated by evoking Eq. (4.4) and using the shape functions, yielding

$$F_{i,k} = \Delta t \sum_{l=1}^{n_{ip}} \sum_{j=2}^{n_p} \left[\xi_j^m x_{ij}^m \frac{k_{rj}^m}{\mu_j^m} \vec{k} \cdot \sum_{h=1}^{n_v} \vec{\nabla} N_h \Phi_{j,h}^m \cdot d\vec{A}_k \right]_l, \quad i = 1, ..., n_c \quad k = 1, ..., n_v, \tag{4.15}$$

The discrete hydraulic potential of phase j evaluated at node h, $\Phi_{j,h}$ is given by

$$\Phi_{j,h} = P_h^{n+1} + P_{cjr,h}^m - \rho_{j,el}^m g D_h, \quad j = 1, ..., n_p. \tag{4.16}$$

All terms of Eq. (4.16) are evaluated at the nodes, as made possible by the use of shape functions. The only exception is the phase mass density, $\rho_{j,el}^n$, which is evaluated at the elements. Therefore, all SCVs inside a single element share the same value for phase mass density when calculating the flux terms. The same process is applied to absolute permeability and reservoir porosity and, since the calculations are all done at SCV level, no problem arises from this approach.

The integration of the pressure equation results in an equation with a similar format to Eq. (4.10). Each term, however, is given by:

$$Acc_{i,k}^P = \left[V_{scv,k} \phi_{o,el} C_f - \frac{V_{scv,k}}{V_{b,k}} \frac{\partial V_{T,k}^n}{\partial P} \right] \left(P_k^{n+1} - P_k^n \right) - \frac{V_{scv,k}}{V_{b,k}} \left(V_{T,k}^n - V_{p,k}^n \right), \quad k = 1, ..., n_v, \tag{4.17}$$

$$\begin{aligned} F_{i,k}^P = {} & \Delta t \bar{V}_{Tw,k}^n \sum_{l=1}^{n_{ip}} \left[\xi_j^m \frac{k_{rw}^m}{\mu_w^m} \vec{k} \cdot \sum_{h=1}^{n_v} \vec{\nabla} N_h \Phi_{w,h}^m \cdot d\vec{A}_k \right]_l + \\ & \Delta t \sum_{i=1}^{n_c} \bar{V}_{Ti,k}^n \sum_{l=1}^{n_{ip}} \sum_{j=2}^{n_p} \left[\xi_j^m x_{ij}^m \frac{k_{rj}^m}{\mu_j^m} \vec{k} \cdot \sum_{h=1}^{n_v} \vec{\nabla} N_h \Phi_{j,h}^m \cdot d\vec{A}_k \right]_l, \quad k = 1, ..., n_v, \end{aligned} \tag{4.18}$$

$$S_k^P = \Delta t \sum_{i=1}^{n_c+1} \bar{V}_{Ti,k}^n \frac{V_{scv,k}}{V_{b,k}}, \quad k = 1, ..., n_v, \tag{4.19}$$

The superscript m used in the flux terms for both material balance and pressure discretized equations denote that the property can either be evaluated at the current time step, $n+1$, or at the previous time step, n, depending on the formulation being used. In this work, an IMPEC (Implicit Pressure, Explicit Compositions) formulation is used. This approach, proposed by Acs *et al.* (1985), solves only the pressure equation implicitly, that is, the equations for all control volumes are solved for simultaneously. These equations form a system that has the format:

$$[A][P] = [B], \tag{4.20}$$

that should be solved by an adequate numerical solver package. The material balance equations are solved explicitly, meaning they are solved one by one with values from the previous time step. Therefore, for the IMPEC formulation, all m superscripts are considered as n.

4.3 Discretized Geomechanical Equations

This section presents the discretization of the geomechanical model presented in Chapter 3. The sequence of this section will be similar to the one used in the previous one that presented the discretized fluid flow equations. We begin by integrating the force balance equation, Eq. (3.78) and applying Gauss's theorem, yielding

$$\int_A \sigma'_{ij} d\vec{A} - \int_{SCV} \alpha \nabla P dV + \int_{SCV} \rho g_i = 0. \tag{4.21}$$

Again, tensor notation is being used to present the geomechanical model to show the equations in a more compact fashion. The result of the integration is an equation that assumes the general form

$$Ef_{i,k} - Pr_{i,k} + Gr_{i,k} = 0, \quad k = 1, ..., n_v, \quad i = x, y, z \tag{4.22}$$

where $Ef_{i,k}$ is the effective stress term, $Pr_{i,k}$ is the pressure term and $Gr_{i,k}$ is the gravity term. Each is given by

$$Ef_{i,k} = \int_A D_{ij} \left(\frac{\partial u_{i,k}}{\partial x_j} + \frac{\partial u_{j,k}}{\partial x_i} \right) dA_i, \quad k = 1, ..., n_v, \tag{4.23}$$

$$Pr_{i,k} = \alpha \sum_{h=1}^{n_v} \nabla N_h P_k V_{scv,k}, \quad k = 1, ..., n_v, \tag{4.24}$$

$$Gr_{i,k} = g_i \rho_k V_{scv,k}, \quad k = 1, ..., n_v, \tag{4.25}$$

where D_{ij} is the elastic properties matrix given by

$$D_{ij} = \begin{bmatrix} \lambda_l \left(\frac{1-\nu}{\nu}\right) & \lambda_l & 0 \\ \lambda_l & \lambda_l \left(\frac{1-\nu}{\nu}\right) & 0 \\ 0 & 0 & \mu_l \end{bmatrix}. \tag{4.26}$$

The use of D_{ij} is another way to represent the application of (3.80) into the effective stress term. It is clear that (4.23) still needs further manipulations. As was performed to the flux terms of the discretized fluid flow model, an accurate approximation of the surface integral is to take the sum of the integrating terms through all integration points in the control volume. As for the derivatives of displacements u, (4.4) is used once again. Finally,

$$Ef_{i,k} = \sum_{l=1}^{n_{ip}} \left[D_{ij} \sum_{h=1}^{n_v} \left(\frac{\partial N_{h,k}}{\partial x_j} u_{i,k} \right) + \sum_{h=1}^{n_v} \left(\frac{\partial N_{h,k}}{\partial x_i} u_{j,k} \right) dA_{i,k} \right]_l, \quad k = 1, ..., n_v, \tag{4.27}$$

The evaluation of Eq. (4.22) at each SCV of each control volume will yield a matrix system of the following form:

$$\left[A_{ij}\right] \left[u_i\right] = \left[B_i\right], \quad i, j = x, y, z \tag{4.28}$$

For example, for a two-dimensional x-z domain, the system will have the format:

$$\begin{bmatrix} A_{xx} & A_{xz} \\ A_{zx} & A_{zz} \end{bmatrix} \begin{bmatrix} u_x \\ u_z \end{bmatrix} = \begin{bmatrix} B_x \\ B_z \end{bmatrix}, \tag{4.29}$$

The solution of the system yields the displacements at each node. Once they are determined, stress and strain can be updated, as mentioned in Chapter 3. Recalling the definition of strain, Eq. (3.84), the only parameter necessary for its evaluation is the displacement, which at this point has been determined. Therefore, using the shape functions, the calculation of strain becomes straightforward as

$$\varepsilon_{ij,l} = \frac{1}{2}\left[\sum_{h=1}^{n_v}\left(\frac{\partial N_{h,k}}{\partial x_j}u_{i,k}\right) + \sum_{h=1}^{n_v}\left(\frac{\partial N_{h,k}}{\partial x_i}u_{j,k}\right)\right], \quad l = 1,...,n_{ip} \tag{4.30}$$

Since the shape functions are evaluated relative to the integration points, the strain and, consequently, stress are also calculated at the integration point. For the two-dimensional case, a plane-strain formulation is used. This approach sets the normal strain in z-direction, ε_{zz}, as zero, since the displacements in this direction are not taken into account as well.

The stress calculation is similar. From Eq. (3.80), once the strain is evaluated, the stress can be found. Rewriting Eq. (3.80) to accommodate the use of the elastic properties matrix, D_{ij}, the stress at each integration point will be given by

$$\sigma'_{ij,l} = D_{ij}\varepsilon_{ij,l} \quad l = 1,...,n_{ip} \tag{4.31}$$

The update of porosity, the main objective of the coupled geomechanical model, requires the calculation of strain, which, as seen on Eq. (4.30), is evaluated at the integration points. Porosity, however, is calculated at element level. This mismatch is solved by using instead an element volumetric strain, which is simply an average of the volumetric strain at all integration points of a single element. So,

$$\phi^*_{el} = 1 - \left(1 - \phi_{o,el}\right)e^{-\varepsilon_{v,el}} \quad el = 1,...,n_{el} \tag{4.32}$$

where $\varepsilon_{v,el}$ is the arithmetic average volumetric strain of element el. The update of permeability is straightforward, since both porosity and permeability are evaluated at element level. It becomes a direct application of Eq. (3.88) for each element.

Now that the discretized geomechanical model has been presented, it is necessary to discuss aspects of the boundary conditions used for the solution.

4.3.1 Boundary Conditions for the Geomechanical Model

The coupled geomechanical model in study can accept two types of boundary conditions: Dirichlet and Neumann conditions. Dirichlet conditions specify the value of a function itself, i.e., the displacement. Therefore, if a Dirichlet boundary condition is applied to a node, the displacement at that node will remain constant throughout the simulation.

Numerically, the matrix lines and columns refering to that node are removed from the system, as well as its term on the right-hand side vector, meaning that the displacement on that node does not need to be solved for.

Neumann conditions specify a normal derivative of a function, in this case, the total stress applied to a node. This can be thought as the overburden stress applied to the top of a reservoir. Since total stress is composed by effective stress and pressure terms, it must be converted before being input into the equations. From the effective stress law,

$$\sigma'_{ij,b} = \sigma_{ij,b} + \alpha P_b \tag{4.33}$$

where b is a Neumann boundary node. Once the effective stress is determined, the condition is applied by adding the resulting force to the right-hand vector of the system. So, at a Neumann boundary vertex b,

$$B_{i,b} = B_{i,b} + \sigma'_{ij,b} \sum_{k=1}^{n_{scv}} A_{k,b} \tag{4.34}$$

where the final term represents the total area around boundary node b in which the stress is applied.

4.4 Coupling Techniques

Different approaches have been developed to properly associate the geomechanical and fluid flow models attempting to balance accuracy and computing load, in order to obtain solutions that are both precise and not too computationally demanding. As previously presented, the coupling methodology can be explicit, iterative or full. In the explicit coupling, the models are solved only once per time step. In the iterative coupling, both models are solved sequentially until convergence for each time step. The fully coupled approach lumps both models in a single system, solving them simultaneously.

A discussion regarding the accuracy and computing load of each technique and how they compare to each other was presented in Chapter 2, but it is important to recall that both the explicit and iterative methods present higher versatility, since they are easier to a pre-existing reservoir simulator code. This is the case of this work and, for this reason, only these techniques were explored. The fully coupled approach would require further adaptations of the original UTCOMP-RS code and therefore is not adopted in this work.

Figure 7 presents a simplified algorithm for the explicit coupling. For any time step, the simulator code follows its usual procedure up until the solution of the fluid flow model. The pressure obtained is passed to the geomechanical model, which uses it as an input parameter. The output of the geomechanical model, the volumetric strain, is then used to update porosity and, optionally, permeability. The updated values are only applied back into the fluid flow model in the next time step. This procedure is repeated until the simulation ends. It is important to note that is not necessary for the geomechanical module to be called in each time step. For subsidence simulations, for example, the changes in the mechanical state of the reservoir are spread out along a large time frame, meaning that it is feasible to solve the geomechanical equations at a different time scale than the one used for the fluid flow model. Other types of problems, like the ones featuring fast propagating fluid fronts, may present changes in short time frames, requiring a higher frequency for the geomechanical module.

The iterative coupling algorithm is presented in Figure 8, although an additional step required by the technique is not presented in the figure. This step, done in the initialization phase of the code, regards an initial solution of the geomechanical model, using the initial pressure distribution in the reservoir, in order to obtain the initial stress state of the domain. Then, the initialization phase is complete and the code proceeds to the calculations of the first time step. First, the reservoir model is solved for pressure, which is then passed to the geomechanical model. Then, an iterative loop begins. For each iteration, the geomechanical model is solved, updating the porosity and permeability. These values are passed back to the fluid flow model for updating pressure. This loop is repeated until the pressure converges. Then, the final values obtained for pressure, porosity and permeability are stored and the code advances to the next time step.

The pressure convergence is checked by taking the relative variation of pressure between two consecutive iterations. So, for a iterative step $k+1$, the convergence criterion is

Figure 7 – Algorithm for the explicit coupling.

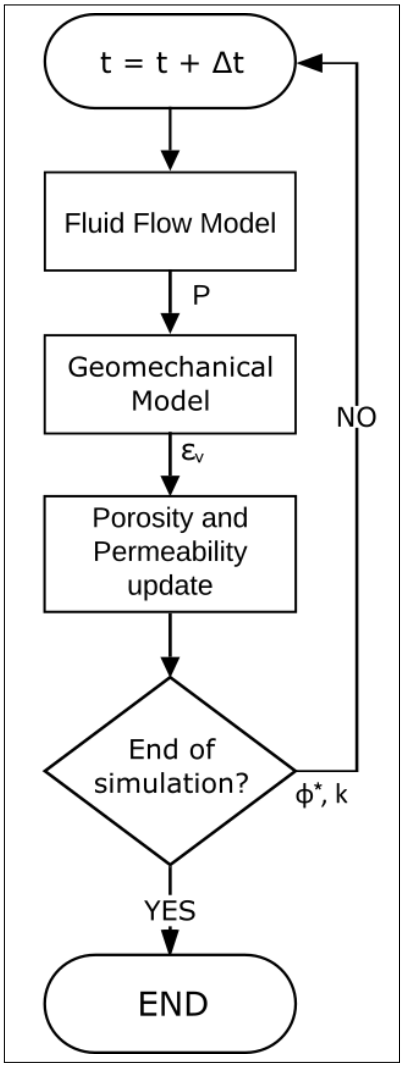

Source: Prepared by the author.

given by:

$$\left| \frac{P^{k+1} - P^k}{P^k} \right| \leq \tau \tag{4.35}$$

where τ is the tolerance factor. If the criterion is met, pressure is considered converged and its value at iteration $k+1$ is taken as the value for that time step. If convergence is not met, the iterative process is repeated, as shown in Fig. 8. For this work, a tolerance value of 10^{-7} was used.

It is clear that the iterative coupling presents more accuracy and stability than the explicit coupling, which is a particular case of the iterative approach, when the maximum number of iterations is kept at one. The improved overall response of the iterative coupling comes at a cost of higher computational loads. The looping nature of the approach and the low tolerance

Figure 8 – Algorithm for the explicit coupling.

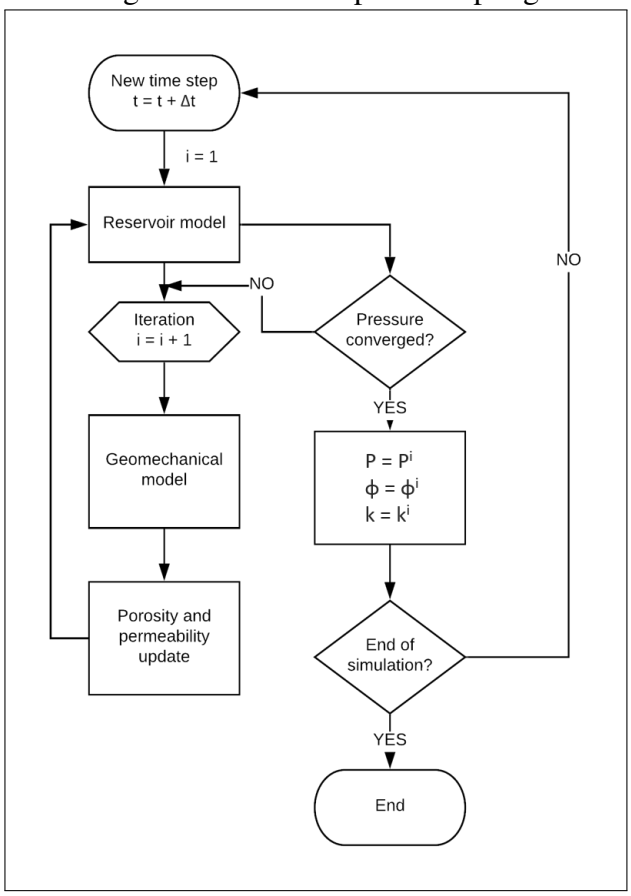

Source: Prepared by the author.

value used for pressure convergence can significantly increase simulation wall clock times.

5 RESULTS

This chapter will present the results from the simulations ran with the UTCOMP-RS simulator coupled with the geomechanical model. Initially, two validation cases are presented. The numerical solution obtained for pressure and displacement is compared to analytical solutions available for these specific cases. The validation intends to show if the implementation presented in this work was done correctly. After that, case studies should be presented for situations that aim to emulate hydrocarbon recovery processes.

All simulations presented in this work were run on the SGI® cluster at the Computational Fluid Dynamics Laboratory, located at the Metallurgical and Materials Engineering Department of Federal University of Ceara.

5.1 Validation

5.1.1 Terzaghi Problem

The first validation case presented was developed by Terzaghi (1923). It is composed of a column of porous rock saturated with water. The column is confined in all its boundaries, except for the top, which is open to the atmosphere. Initially, the domain is at atmospheric pressure, until a constant load σ_0 is instantly applied at the top boundary, immediately increasing the fluid pressure, as an attempt to balance the external stress applied. The pressure gradient will force the water out of the porous medium and, given a large enough time, alleviate the pore pressure back to atmospheric level. Figure 9 presents a schematics of the case.

It is important now to present the boundary conditions used for each model. For the fluid flow equations, the column has no-flow boundaries, except for the top one. This boundary is open to the atmosphere and will allow the water inside the pores to flow out of the domain. In terms of the equations presented in the previous chapters, this can be interpreted as a production well running along all nodes on the top boundary. This well operates at a constant bottom-hole pressure equal to the atmospheric pressure.

For the geomechanical model, the lateral boundaries have Dirichlet conditions of constant horizontal displacement equal to zero, while the bottom boundary has a Dirichlet condition of constant vertical displacement equal to zero. The top boundary is under a Neumann condition for constant stress applied to it.

Figure 9 – Physical domain for the Terzaghi problem.

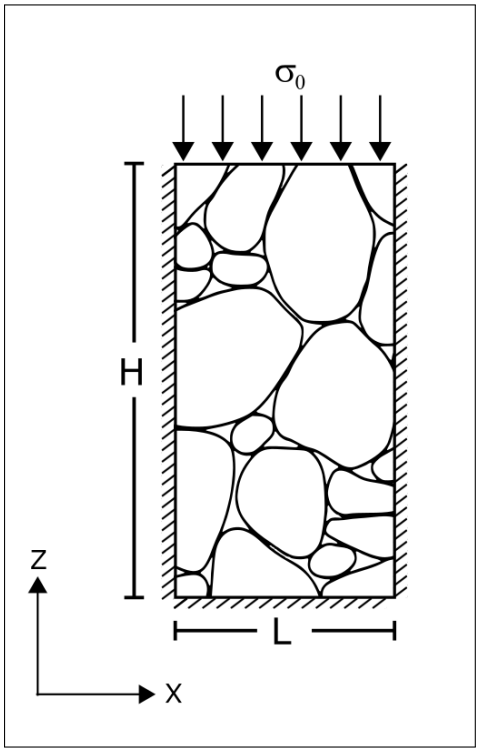

Source: Prepared by the author.

Input properties for the case are the same used by Ribeiro (2016) and are presented in Table 1.

Table 1 – Physical properties for the Terzaghi problem.

Property	Symbol	Value	Unit
Column height	H	6.0	m
Column length	L	1.0	m
Column thickness	D	0.25	m
Applied stress	σ_0	10^6	Pa
Porosity	ϕ_o	0.19	-
Absolute permeability	k	1.9	md
Initial water saturation	S_w	1.0	-
Water viscosity	μ_w	1.0	cP
Water density	ρ_w	62.343	lb/ft^3
Initial pressure	P	63.12	psi
Young's modulus	E	14.4×10^9	Pa
Poisson's ratio	ν	0.2	-
Biot-Willis coefficient	α	0.778	-

Source: Ribeiro (2016).

Given the simplicity of the problem, coarse grids, with both triangular and quadrilateral elements, were proven adequate to obtain an accurate result. All grids used in this work were obtained using the mesh generation software GiD® v. 14.0. The properties of the two-dimensional meshes used in this case are shown in Table 2 and are represented in Figure 10.

Table 2 – Mesh properties for the Terzaghi problem.

Mesh	Element type	Number of vertices	Number of elements
1	Quadrilateral	15	8
2	Triangle	32	38

Source: Author.

Figure 10 – Quadrilateral (a) and triangular (b) meshes used for the Terzaghi problem.

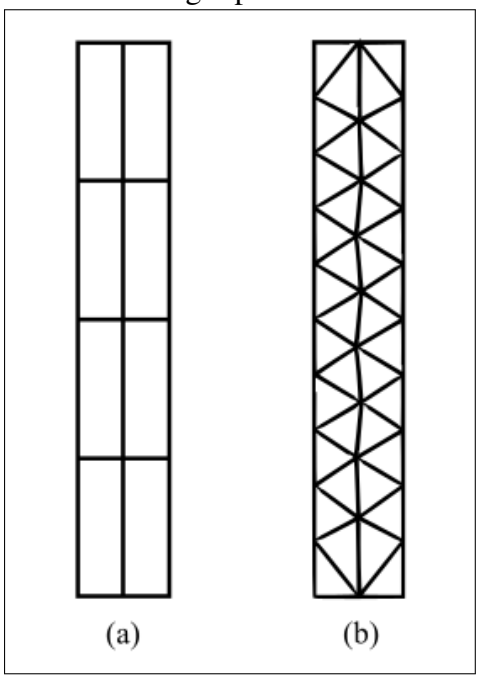

Source: Prepared by the author.

The analytical solution for pressure and displacement is presented by Schiffmann (1960) and the equations are presented in A. The pressure behaves in an intuitive manner. After rise in pore pressure induced by the external load, the pressure gradient between the column and the atmosphere will drive out the water in the pores, leading to the pressure alleviation. Figure 11 presents the results for pore pressure at the base of the column *versus* time for both the analytical solution and the numerical results obtained from the coupled model for the quadrilateral mesh, showing the rapid pressure decrease occurring in the column. It is worthwhile to point that the pressure values represented in the results are gauge values, meaning that it considers its zero as the atmospheric pressure, and not as perfect vacuum, as it is done for absolute pressure. The time profile provides a good description of the phenomenon, from the initial constant pressure on the column, to the top boundary kept at atmospheric pressure, gradually reducing the pressure until it becomes, given an infinite amount of time, equal to the atmospheric pressure. The results show a good match between the solutions, indicating a successful implementation.

Analytical results are also available for the behavior of displacement along y-axis on

Figure 11 – Analytical and numerical pressure results for the Terzaghi problem.

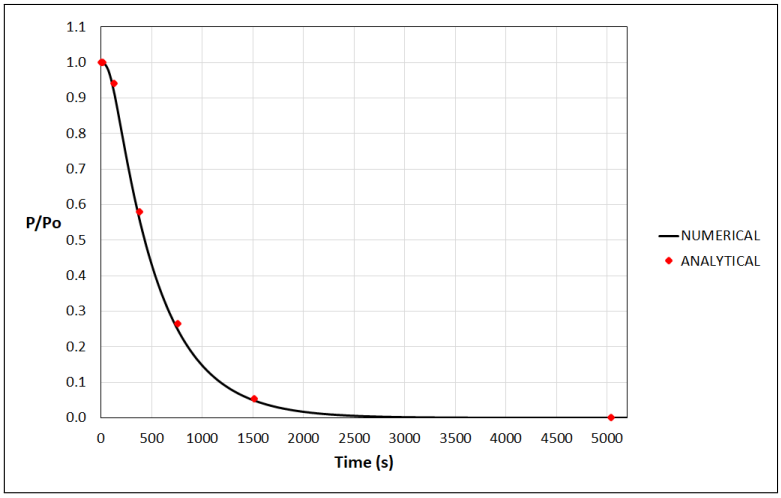

Source: Prepared by the author.

the column. Figure 12 presents the comparison between the analytical and numerical results for said displacement at the base of the column *versus* time. The axis representing displacement on the graph is inverted for a more intuitive interpretation. A satisfactory match between results can be seen, validating the implementation for this one-dimensional problem. Another takeaway from this result is the mechanical behavior of the column matrix. The column is compressed and starts to deform along the y-axis. The increase in deformation is linked to the pressure decrease, as predicted by the coupled model. This can be seen in the results as the column pressure reaches closer to zero, the displacement reaches a plateau, indicating the establishment of an equilibrium state.

Figure 12 – Analytical and numerical displacement on y-axis results for the Terzaghi problem.

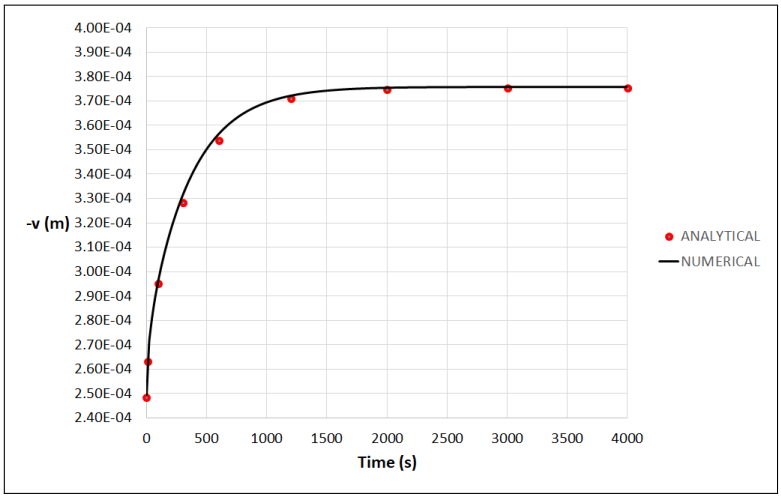

Source: Prepared by the author.

5.1.2 Mandel Problem

Another classic benchmark case for the coupled geomechanical analysis was first presented by Mandel (1953) as a solution for the three-dimensional consolidation theory, obtaining a non-monotonic pore pressure behavior. Cryer (1963) later obtained similar results for a spherical problem. The problem is composed of an infinitely long rectangular porous medium saturated with water. The medium is compressed at the top and bottom by two rigid impermeable plates, while the lateral sides are free to deform. Given the symmetrical aspect of the problem, it is reasonable to consider only one quarter of the domain for the simulation, while adjusting the boundary conditions accordingly and disregarding the gravity terms in the geomechanical model. Quantitatively speaking, the gravity terms are small enough, compared to the effective stress and pressure terms, that it is reasonable to make this assumption. Figure 13 shows the full domain and the section used for the simulations.

Figure 13 – Full symetrical domain and reduced domain used for the solution of Mandel problem.

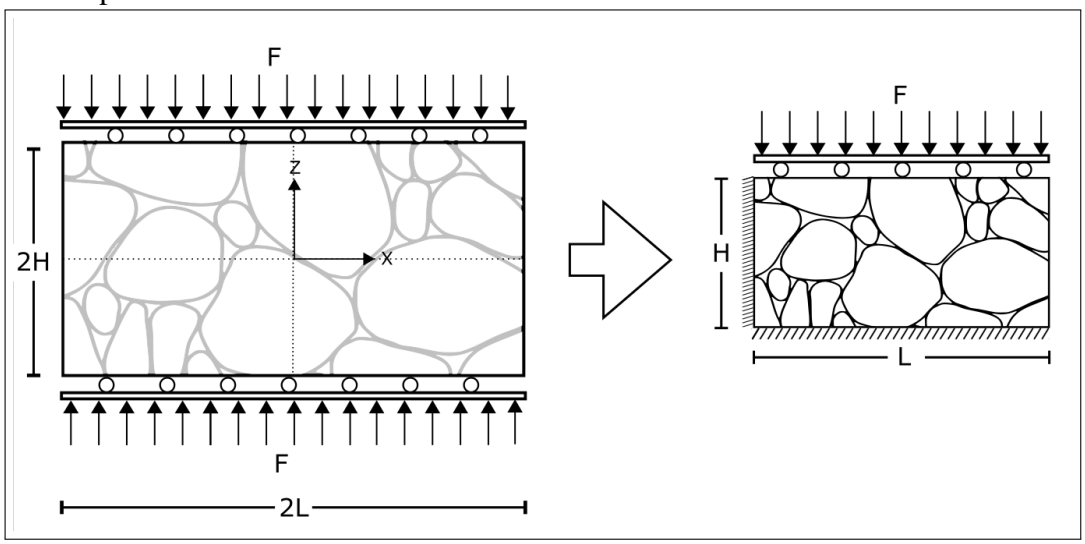

Source: Prepared by the author.

Initially, a force F is applied to both plates, prompting a pore pressure distribution to be generated. Once the fluid is allowed to flow through the lateral boundaries and out of the domain, the pressure near these regions decrease, as expected. However, near the center of the domain, there is a slight increase in pore pressure during the early moments of drainage. This can be explained by the fact that, when the initial load is applied, the sample is undrained, and the pore pressure acts to increase the apparent compressive stiffness of the matrix, in order to support the load. Once drainage begins, and the pore pressure decreases near the sides, this

stiffness decreases. In order to maintain the force balance, part of the higher compressive stress near the sides is transferred to the center of the domain. This transfer causes the pore pressure in the center to increase for some time. The continuous drainage eventually reaches the center of the domain, as the pressure is alleviated, characterizing a non-monotonic behavior that cannot be detected in simple diffusion cases, such as seen on the Terzaghi problem. This non-monotonic effect has been named Mandel-Cryer effect, after the authors that first presented this phenomenon on their aforementioned works. The effect has been also confirmed in the laboratory, as well as in actual oil fields (GIBSON *et al.*, 1963; VERRUIJT, 1969).

The boundary conditions for the geomechanical model are different from the ones used on the Terzaghi problem. For the left boundary, horizontal displacement is constant and equal to zero; for the bottom boundary, vertical displacement is constant and equal to zero; for the right boundary, the stress component normal to the boundary, σ'_{xx} is constant and equal to zero; and for the top boundary, the force applied is constant and must be used to calculate the applied stress to the boundary. From the definition of stress, it can be inferred for the boundary that:

$$\int_A \sigma_b dA = F, \tag{5.1}$$

where D is the reservoir thickness and σ_b is the stress applied to the boundary and the traditional variable used for a Neumann condition. In practical terms, for each time step, the code must check if the condition presented in Eq. (5.1) is met. This is accomplished through an iterative procedure described by Ribeiro (2016).

1. At the initial time step, an estimate for the applied stress is taken as:
$$\sigma_b^k = \frac{F}{DL}; \tag{5.2}$$
2. Solve both fluid flow and geomechanical models and obtain the total stress distribution along the boundary;
3. Check if the calculated total stress meets the criterion from Eq. (5.1):
$$\left| \frac{\sum_{i=0}^{n_b} |\sigma_{yy,i}^k| \Delta A_i - F}{F} \right| \leq \tau; \tag{5.3}$$
4. If the criterion is not met, σ_b is updated by:
$$\sigma_b^{k+1} = \sigma_b^k - \left(\frac{\sum_{i=0}^{n_b} |\sigma_{yy,i}^k| \Delta A_i - F}{LD} \right); \tag{5.4}$$

5. Return to step 2 until the criterion is met. Then, advance to the next time step.

In the above steps, n_b represents the number of control volumes adjacent to the boundary, ΔA is the areas of the faces in these control volumes that are exposed to boundary and τ is a tolerance factor, that, in this work was set as 1×10^{-4}.

Another important detail regarding the top boundary is that since it is in contact with the rigid plate, the vertical displacement must be equal at all points across the boundary.

The input properties for the case are presented in Table 3. The properties of the two-dimensional meshes used in this case are shown in Table 4 and are represented in Figure 14.

Table 3 – Physical properties for the Mandel problem.

Property	Symbol	Value	Unit
Column height	H	2.0	m
Column length	L	10.0	m
Column thickness	D	1.0	m
Applied force	F	10^8	N
Porosity	ϕ_o	0.19	-
Absolute permeability	k	0.2	md
Initial water saturation	S_w	1.0	-
Water viscosity	μ_w	1.0	cP
Water density	ρ_w	62.343	lb/ft^3
Initial pressure	P	417.2	psi
Young's modulus	E	14.4×10^9	Pa
Poisson's ratio	ν	0.2	-
Biot-Willis coefficient	α	0.79	-

Source: Author.

Table 4 – Mesh properties for the Mandel problem.

Mesh	Element type	Number of vertices	Number of elements
1	Quadrilateral	27	16
2	Quadrilateral	158	127

Source: Author.

The analytical solution was presented by Mandel (1953) only for pressure, but Abousleiman *et al.* (1996) extended it for displacement and vertical total stress. The equations for the solution are presented in A. Figure 15 presents the simulated results for pore pressure at the left border of the domain *versus* time and its comparison with the analytical solution. From the graph, it can be seen that the model implemented was able capture the non-monotonic behavior of pressure in the early stages of simulation. This behavior is characteristic of the previously mentioned Mandel-Cryer effect. The left border of the simulated domain corresponds to the center of the original domain, as seen in Figure 13, and is the region where the effect

Figure 14 – Quadrilateral meshes used for the Mandel problem.

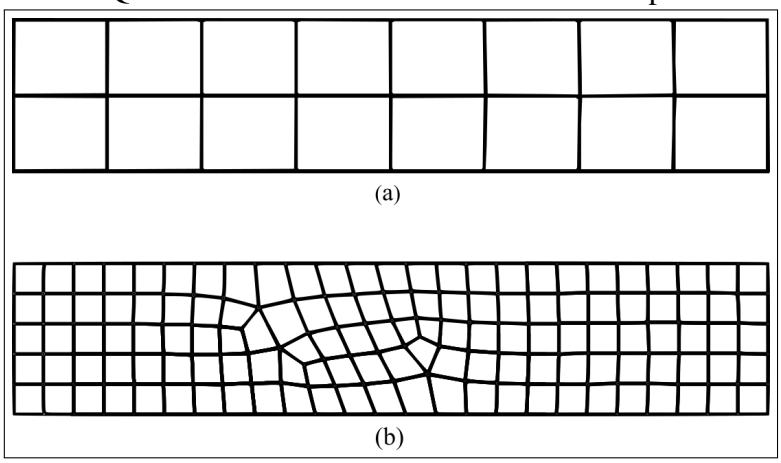

Source: Prepared by the author.

is most clearly detected. Despite achieving the expected behavior, the values obtained for the pressure field are considerably different than the ones for the analytical solution. Despite starting from the same initial pressure, the numerical results seem to indicate the reservoir tends to reach a new equilibrium pressure below 400 psi early in the simulation.

Figure 15 – Numerical and analytical pressure results for the Mandel problem.

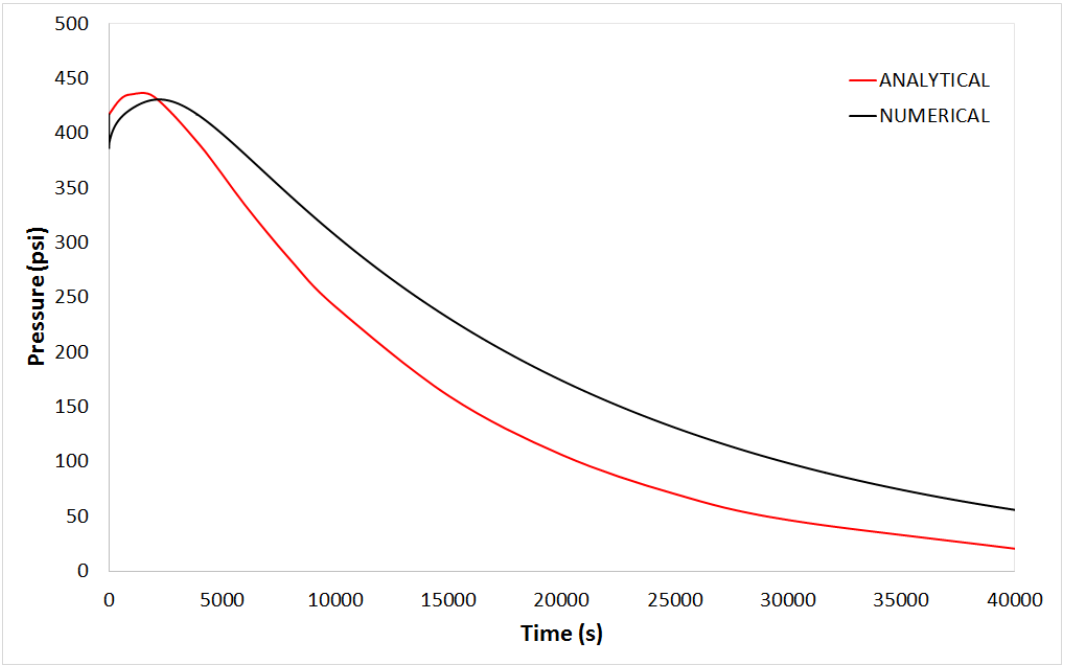

Source: Prepared by the author.

Other variables can be inspected as well. Figure 16 shows the results for vertical total stress, σ_{yy}, *versus* time at the left border of the domain. The behavior shows similarities to the analytical solution, although they also do not match. As expected by the Mandel-Cryer effect, there was a transference of compressive strength from the right border to the left border

of the domain although it happens at a slower rate, in comparison with the analytical results. As pressure is alleviated further in the simulation the stress tends to return to the initial value and the numerical results will eventually approximate the analytical curve.

Figure 16 – Numerical and analytical vertical total stress results for the Mandel problem.

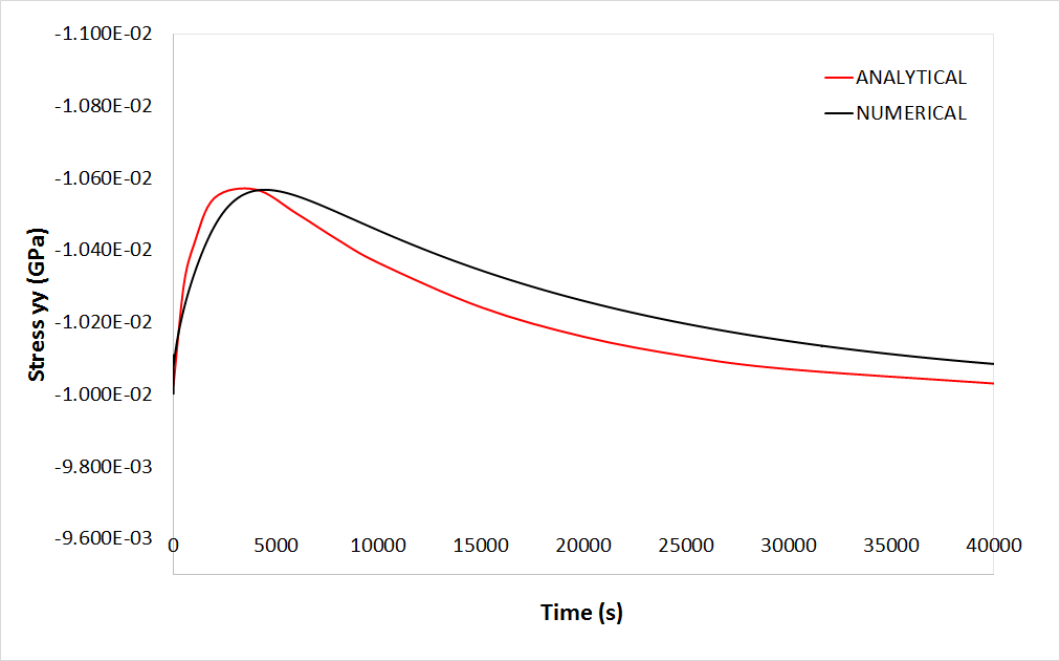

Source: Prepared by the author.

The results for displacement show a similar outcome. Figures 17 and 18 present respectively the horizontal and vertical displacements *versus* time. While the initial equilibrium profiles obtained closely approach the analytical solution, they separate after few time steps. For displacements at both x and z-axis direction, the behavior with time is in agreement with the one displayed by the analytical solution.

5.2 Case Studies

This section presents case studies that resemble real hydrocarbon recovery processes. The focus of the analysis will be on the effect of the geomechanical effect on the production of oil and gas and on the pressure distribution in the reservoir.

5.2.1 Primary Recovery with 3-pseudocomponent fluid mixture

This case presents a simple primary depletion case, in which a single production well is placed on one of the borders of the reservoir. A constant stress is applied to the top of

Figure 17 – Numerical and analytical horizontal displacement results for the Mandel problem.

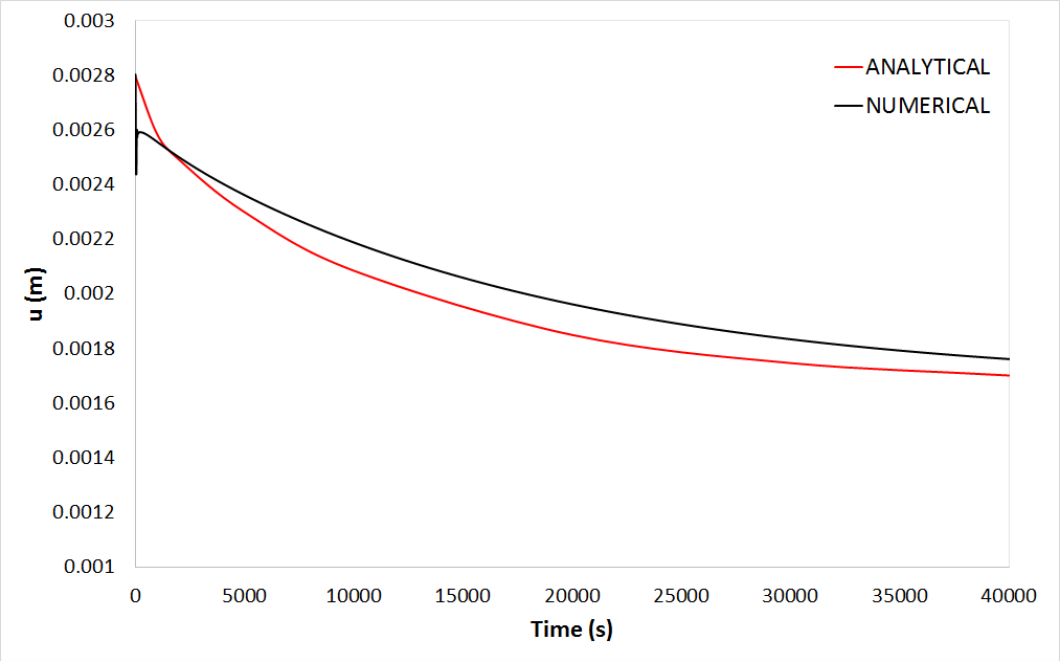

Source: Prepared by the author.

Figure 18 – Numerical and analytical vertical displacement results for the Mandel problem.

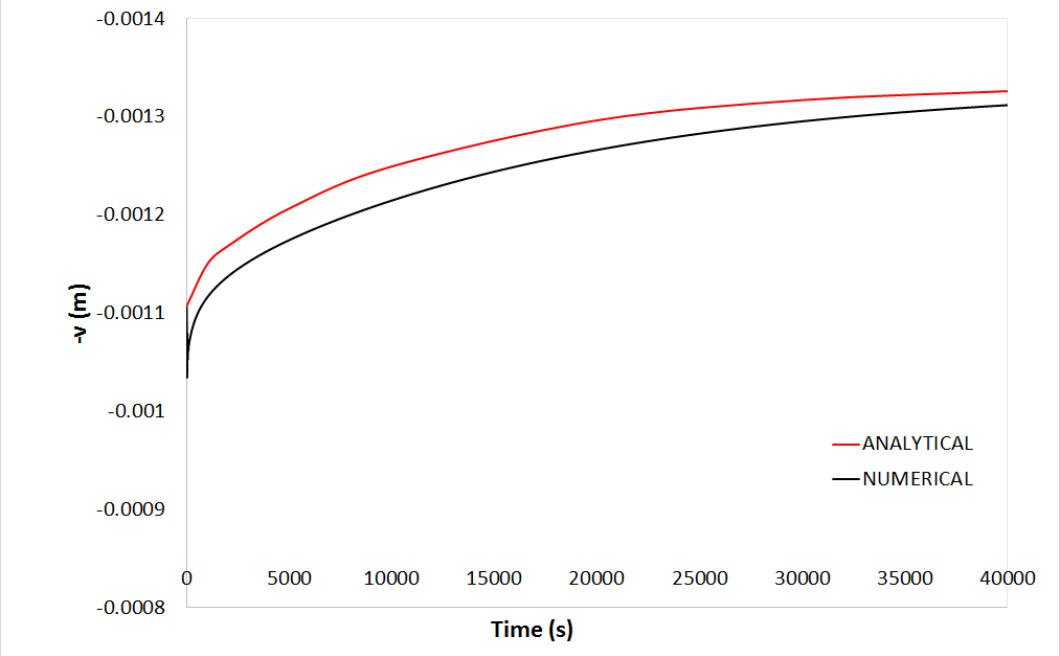

Source: Prepared by the author.

the domain. Reservoir hydrocarbon fluids are lumped in 3 pseudocomponents and up to the phases (oil, gas and water) can be found simultaneously in the pore space. This case should be able to showcase the capability of the coupled simulator to handle multiphase fluid using the compositional model. A single unstructured grid was used for the case. It is composed of 324

vertices and 240 quadrilateral elements. Figure 19 shows a schematics of the case and Tables 5 and 6 present the input properties for the reservoir and fluid.

Figure 19 – Schematics for the primary depletion case.

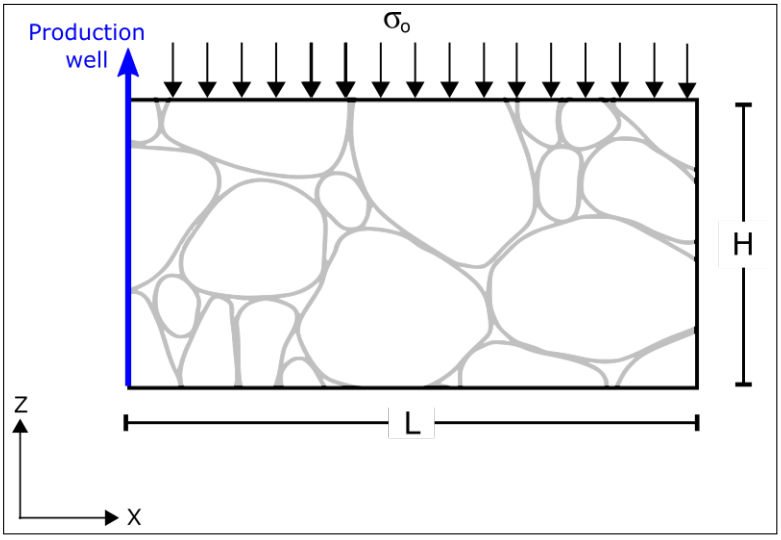

Source: Prepared by the author.

Table 5 – Physical properties for the primary depletion case.

Property	Symbol	Value	Unit
Simulation time	t	120.0	days
Reservoir height	H	40.0	ft
Reservoir length	L	1200.0	ft
Reservoir thickness	D	10.0	ft
Applied stress	σ_0	4.137×10^7	Pa
Porosity	ϕ_o	0.35	-
Absolute permeability	k	10	md
Initial water saturation	S_w	0.17	-
Water viscosity	μ_w	1.0	cP
Water density	ρ_w	62.343	lb/ft^3
Initial pressure	P	6000	psi
Well bottom-hole pressure	P_{bh}	500	psi
Young's modulus	E	9.0×10^9	Pa
Poisson's ratio	ν	0.01	-
Biot-Willis coefficient	α	0.79	-

Source: Author.

The evolution of average reservoir pressure with time is presented in Figure 20 for simulation with and without the geomechanical coupled solution. Both cases show the expected pressure for primary recovery, that is rapid pressure decline, especially when most of the reservoir fluid is composed of the heavier pseudocomponent $n-C_{16}$. When the geomechanical effect is taken into account, the pressure decline slightly slower, which is reflected on the recovery factor curve, shown in Figure 21. Since during the first 10 days of production, the average pressure

Table 6 – Fluid properties for the primary depletion case.

Property	Symbol	CO_2	C_1	n-C_{16}	Unit
Critical pressure	P_c	1071.6	667.2	252.1	psi
Critical temperature	T_c	547.6	343.1	1322.4	^oR
Critical volume	V_c	1.5	1.6	13.1	$ft^3/lb-mole$
Molecular weight	MW_i	44.01	16.04	222.0	lbm/lb-mole
Initial mole fraction	z_j	0.01	0.19	0.8	-

Source: Author.

is higher in the geomechanical case, the pressure gradient towards the well will also be higher, leading to an increased oil recovery. The values obtained for the recovery factor are expected be small, since the primary recovery method yields a fast pressure decline, as previously mentioned, and no other fluid driving force is being deployed.

Figure 20 – Average reservoir pressure versus time for the primary depletion case.

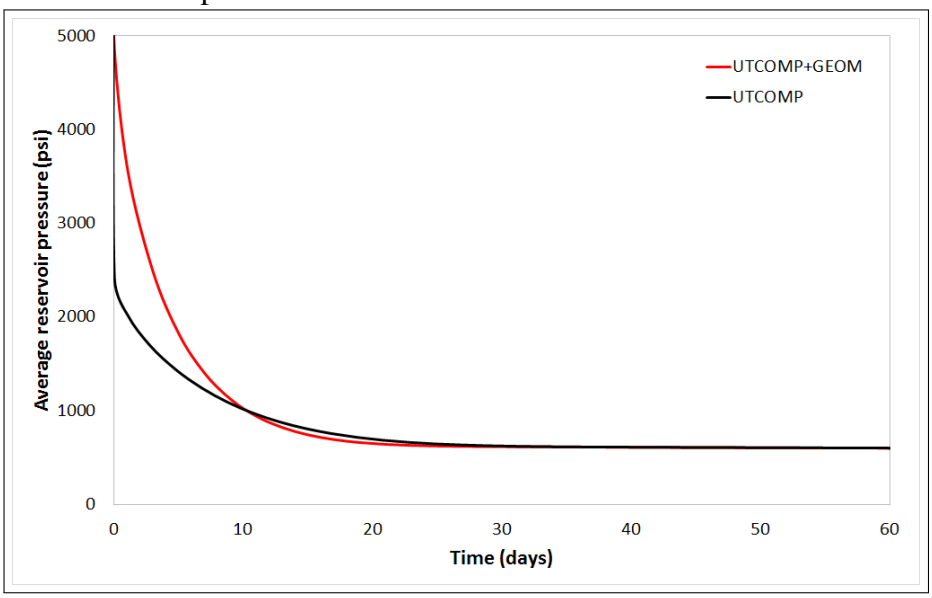

Source: Prepared by the author.

5.2.2 Gas injection with 3-pseudocomponent fluid mixture

This case presents a secondary recovery process, in which a gas mixture, predominantly CO_2, is injected into a reservoir to provide the energy necessary to drive the reservoir fluids towards the production well. Wells are placed on the borders of the domain. Given the considerable depth of the reservoir, it is a more realistic approach to place the wells in smaller segments, which emulates the real-life well completion strategies for injection and production. A completion interval of 58.8 ft was chosen for both wells. The injection well was placed near

Figure 21 – Oil recovery factor versus time for the primary depletion case.

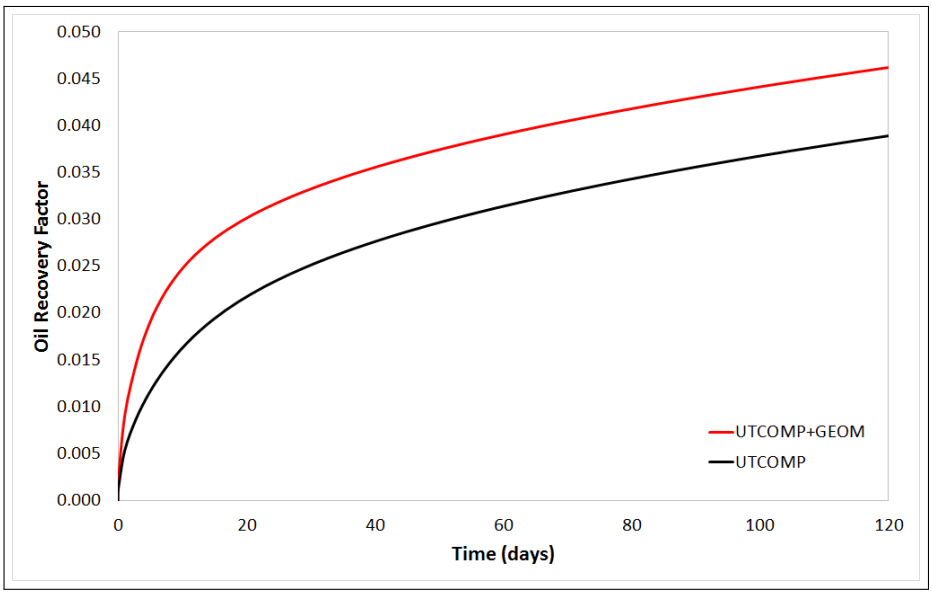

Source: Prepared by the author.

the bottom of the border and the production well placed near the top. This arrangement takes advantage of the lower density of the injected gas to to provide a better sweeping of the reservoir fluids. Again, a constant stress is applied to the top of the domain. Similarly to the previous case study, a 3-pseudocomponent fluid model was used. A single unstructured grid was used for the case. It is composed of 612 vertices and 561 quadrilateral elements. Figure 22 shows a schematics of the case and Tables 7 and 8 present the input properties for the reservoir and fluid.

Figure 22 – Schematics for the 3-component gas injection case.

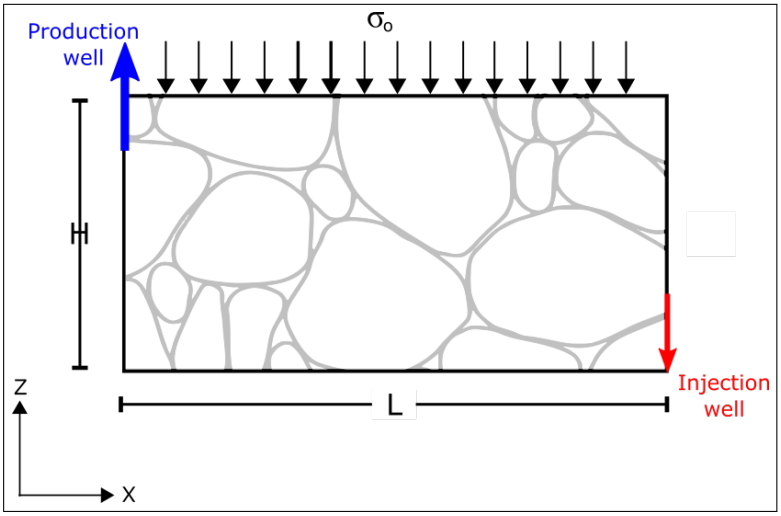

Source: Prepared by the author.

Figures 23 and 24 show respectively the production curves of oil and gas for simulation with and without the geomechanical coupling. The coupled simulation presented a similar

Table 7 – Physical properties for the 3-component gas injection case.

Property	Symbol	Value	Unit
Simulation time	t	150.0	days
Reservoir height	H	250.0	ft
Reservoir length	L	500.0	ft
Reservoir thickness	D	250.0	ft
Applied stress	σ_0	4.137×10^7	Pa
Porosity	ϕ_o	0.30	-
Absolute permeability	k	100	md
Initial water saturation	S_w	0.25	-
Water viscosity	μ_w	1.0	cP
Water density	ρ_w	62.343	lb/ft^3
Initial pressure	P	2800	psi
Production well bottom-hole pressure	P_{bh}	2800	psi
Injection well gas flow rate	$q_{g,I}$	50000	MSCF/day
Young's modulus	E	9.0×10^9	Pa
Poisson's ratio	ν	0.01	-
Biot-Willis coefficient	α	0.79	-

Source: Author.

Table 8 – Fluid properties for the 3-component gas injection case.

Property	Symbol	CO_2	C_1	n-C_{16}	Unit
Critical pressure	P_c	1071.6	667.2	252.1	psi
Critical temperature	T_c	547.6	343.1	1322.4	^{o}R
Critical volume	V_c	1.5	1.6	13.1	$ft^3/lb-mole$
Molecular weight	MW_i	44.01	16.04	222.0	lbm/lb-mole
Initial mole fraction	z_j	0.01	0.19	0.8	-
Injection fluid composition	$z_{j,I}$	0.95	0.05	-	-

Source: Author.

behavior to the uncoupled one, with slight value differences, as expected. By considering the geomechanical effect, the results predict, in comparison to the uncoupled solution, an earlier beginning of oil production, as well as a slightly earlier gas breakthrough.

Other variables showed a similar behavior. The oil recovery factor, in Fig. 25, was higher for the coupled solution, although both curves converged to close values by the end of the simulation. The same behavior is seen on the average reservoir pressure curve, in Fig. 26. Another important operational parameter for gas injection processes is the Gas-Oil Ratio (GOR), measured at the production well. Figure 27 presents the GOR evolution for the case in study. Again, the behavior of both solutions is very similar, with an increase in the coupled solution GOR, towards the end of the simulation.

In this case, only the porosity is being used as a coupling parameter between the geomechanical and fluid flow models, with permeability kept constant throughout the simulation. The compaction drive effect is benefited, translating into a slightly higher oil recovery for the

Figure 23 – Oil production rate for the 3-component gas injection case.

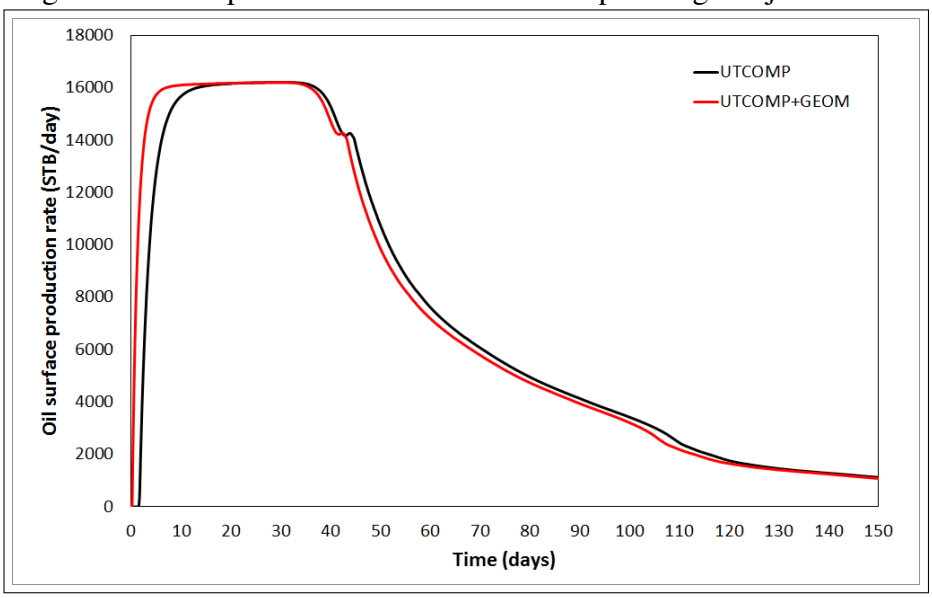

Source: Prepared by the author.

Figure 24 – Gas production rate for the 3-component gas injection case.

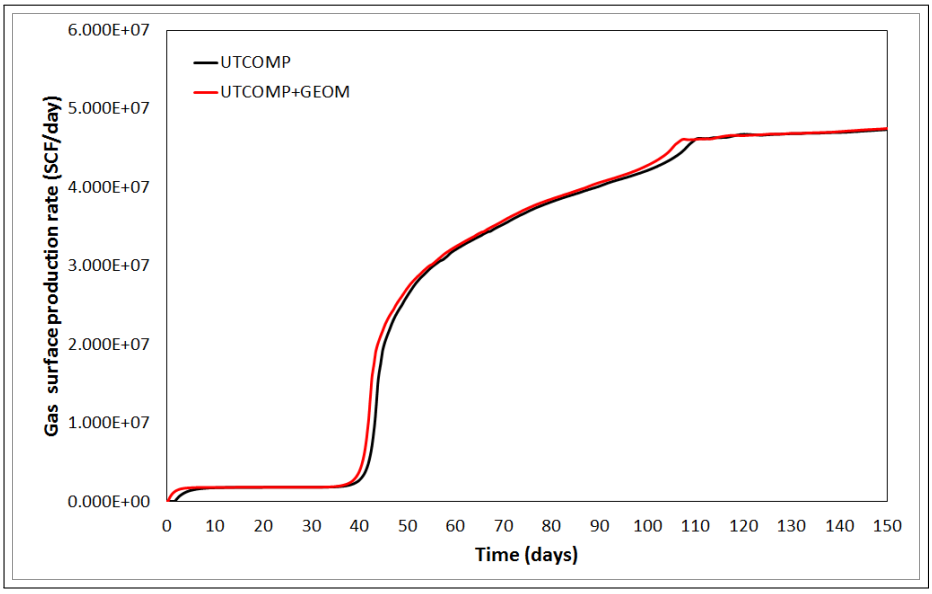

Source: Prepared by the author.

coupled solution. If the permeability was allowed to vary as well, given its power-law nature, decreases in its value were likely to be seen for the coupled solution, which could impact negatively on the oil recovery.

5.2.3 Gas injection with 6-pseudocomponent fluid mixture

This case presents a similar situation to the one studied in the previous case, in which a gas mixture is injected into a reservoir to provide the energy necessary to drive the reservoir fluids towards the production well. In the present case, however, a different composition is

Figure 25 – Oil recovery factor for the 3-component gas injection case.

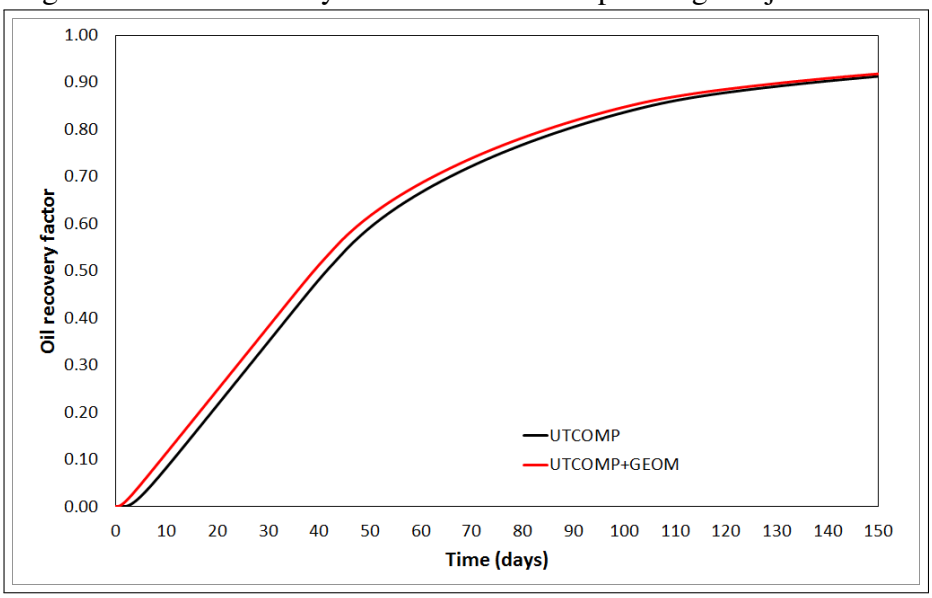

Source: Prepared by the author.

Figure 26 – Average reservoir pressure for the 3-component gas injection case.

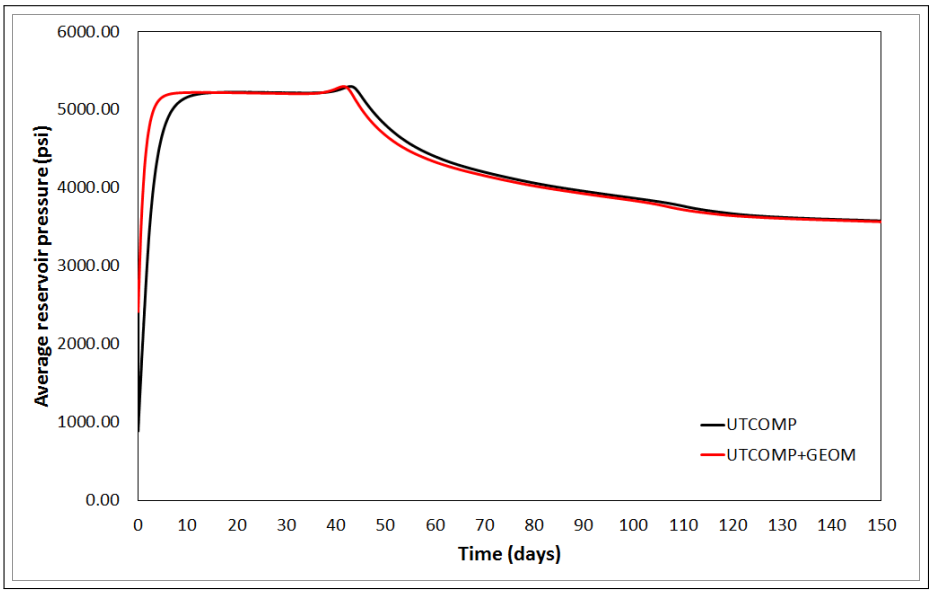

Source: Prepared by the author.

used for both the reservoir and injection fluids. A 6-pseudocomponent fluid model is used. The injection fluid represents natural gas, being mostly methane and propane. The dimensions of the reservoir and the arrangement of the wells in it is the same used for the previous case. The discrete grid used is also the same. Figure 22 shows a schematics of the case and Tables 9 and 10 present the input properties for the reservoir and fluid.

Figures 28 and 29 show respectively the production curves of oil and gas for simulation with and without the geomechanical coupling. For the geomechanical case, two situations were simulated: the first considering only the porosity as a coupling parameter ("UT-

Figure 27 – Gas-Oil Ratio results for the 3-component gas injection case.

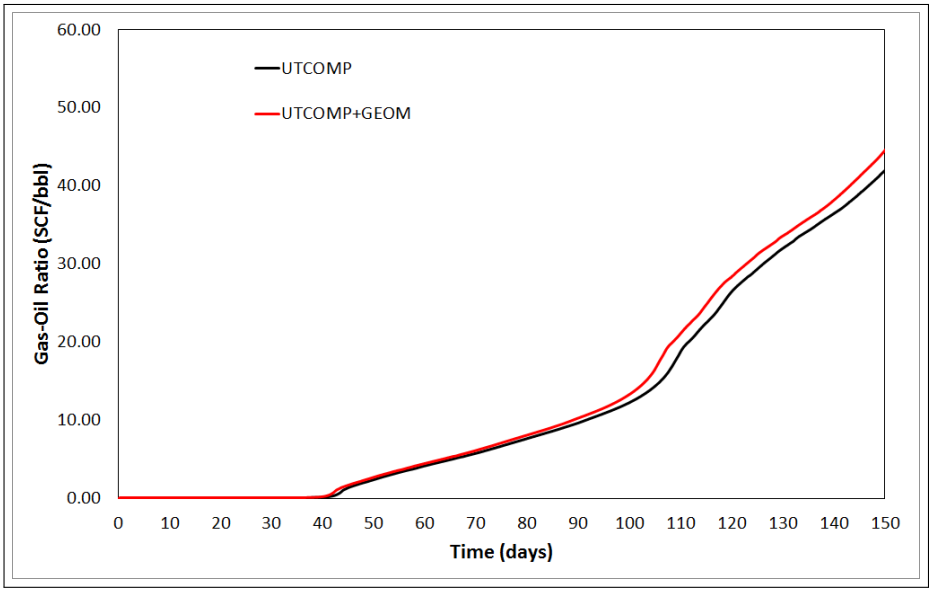

Source: Prepared by the author.

Table 9 – Physical properties for the 6-component gas injection case.

Property	Symbol	Value	Unit
Simulation time	t	1000.0	days
Reservoir height	H	250.0	ft
Reservoir length	L	500.0	ft
Reservoir thickness	D	250.0	ft
Applied stress	σ_0	5.515×10^7	Pa
Porosity	ϕ_o	0.35	-
Absolute permeability	k	10	md
Initial water saturation	S_w	0.17	-
Water viscosity	μ_w	1.0	cP
Water density	ρ_w	62.343	lb/ft^3
Initial pressure	P	1500	psi
Production well bottom-hole pressure	P_{bh}	1500	psi
Injection well gas flow rate	$q_{g,I}$	500 0	MSCF/day
Young's modulus	E	9.0×10^9	Pa
Poisson's ratio	ν	0.2	-
Biot-Willis coefficient	α	0.79	-
Permeability coupling exponent	n	30	-

Source: Author.

COMP+GEOM (POR)") and the second considering both porosity and permeability variation ("UTCOMP+GEOM (POR+PERM)"). The comparison between the coupled and uncoupled solutions show a similar behavior to the previous case, in which the coupled results are more optimistic in terms of oil recovery. The addition of the variation of permeability did not incur in discernible differences to the production results.

Other variables present a similar trend to the previous case. The oil recovery factor, in Fig. 30, was slightly higher for the coupled solutions, with no differences between the porosity

Table 10 – Fluid properties for the 6-component gas injection case.

Property	Symbol	C_1	C_3	C_6	C_{10}	C_{15}	C_{20}	Unit
Critical pressure	P_c	667.8	616.3	436.9	304.0	200.0	162.0	psi
Critical temperature	T_c	343.0	665.7	913.4	111.8	1270.0	1380.0	^{o}R
Critical volume	V_c	1.599	3.211	5.923	10.087	16.696	21.484	$ft^3/lb-mole$
Molecular weight	MW_i	16.0	44.1	86.2	142.3	206.0	282.0	lbm/lb-mole
Initial mole fraction	z_j	0.5	0.03	0.07	0.2	0.15	0.05	-
Injection fluid composition	$z_{j,I}$	0.77	0.2	0.01	0.01	0.005	0.005	-

Source: Author.

Figure 28 – Oil production rate for the 6-component gas injection case.

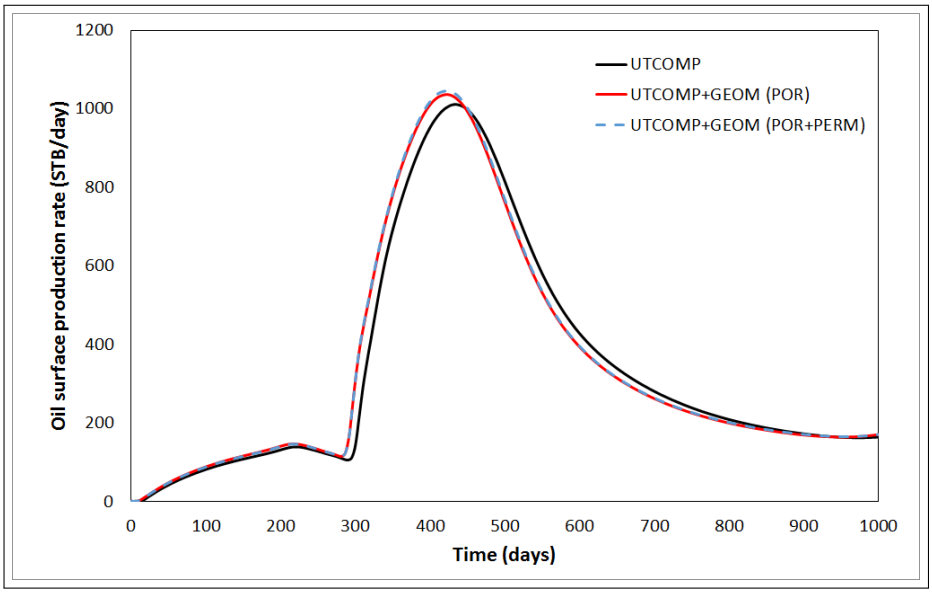

Source: Prepared by the author.

Figure 29 – Gas production rate for the 6-component gas injection case.

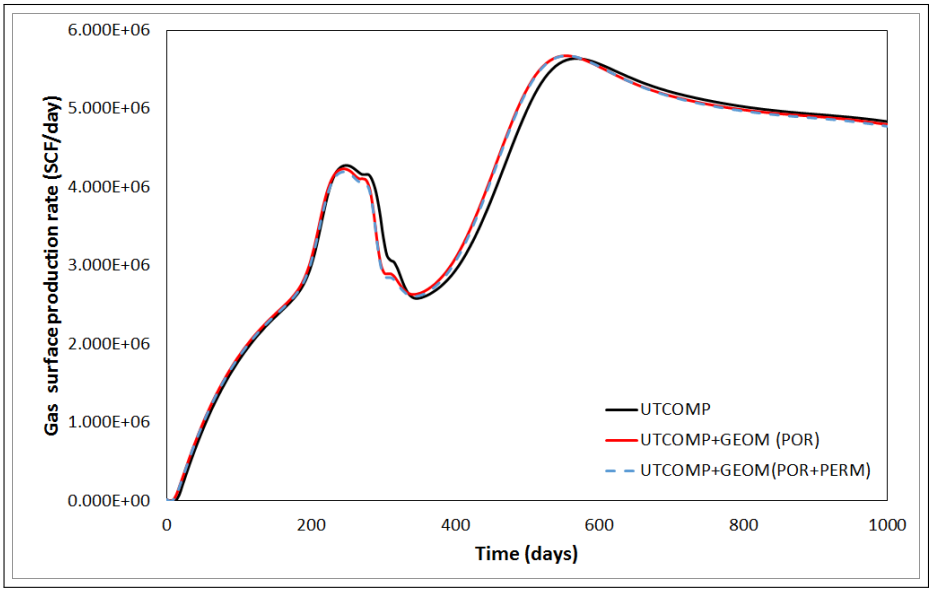

Source: Prepared by the author.

coupling and the porosity and permeability coupling. The same pattern is seen on the average reservoir pressure curve, in Fig. 31, and gas-oil ratio, measured at the production well, in Fig.

32.

Figure 30 – Oil recovery factor for the 6-component gas injection case.

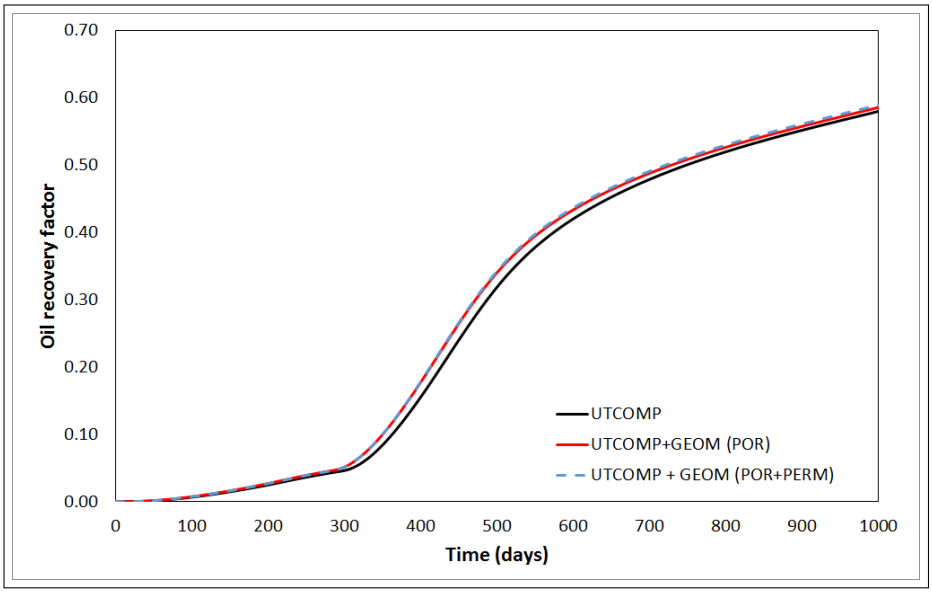

Source: Prepared by the author.

Figure 31 – Average reservoir pressure for the 6-component gas injection case.

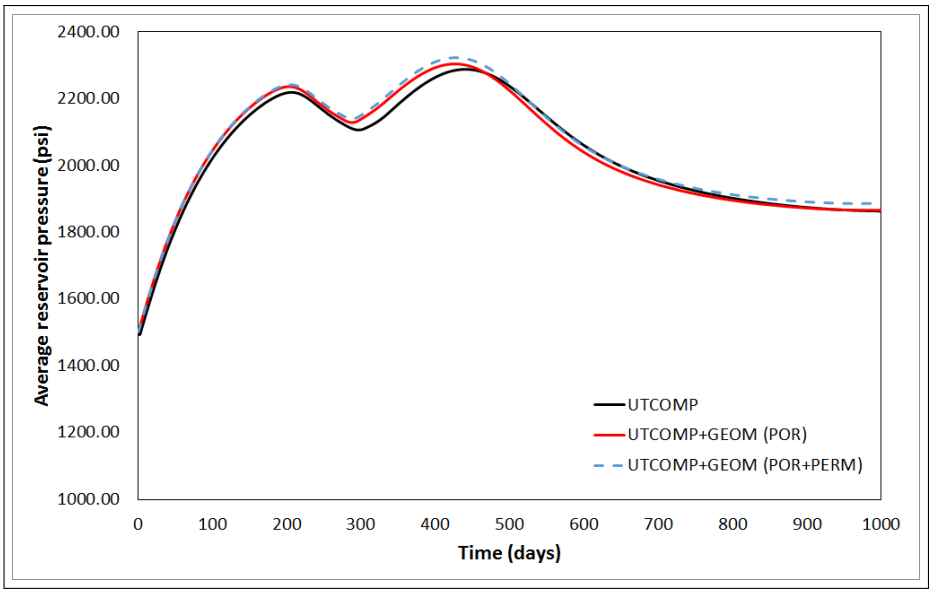

Source: Prepared by the author.

In this case, even though both porosity and permeability were used as coupling parameters and a deliberately high value for the coupling exponent was chosen, the compaction drive effect was again prevalent. The permeability decrease was not significant enough to yield any noticeable alterations on the results.

Figure 32 – Gas-Oil Ratio results for the 6-component gas injection case.

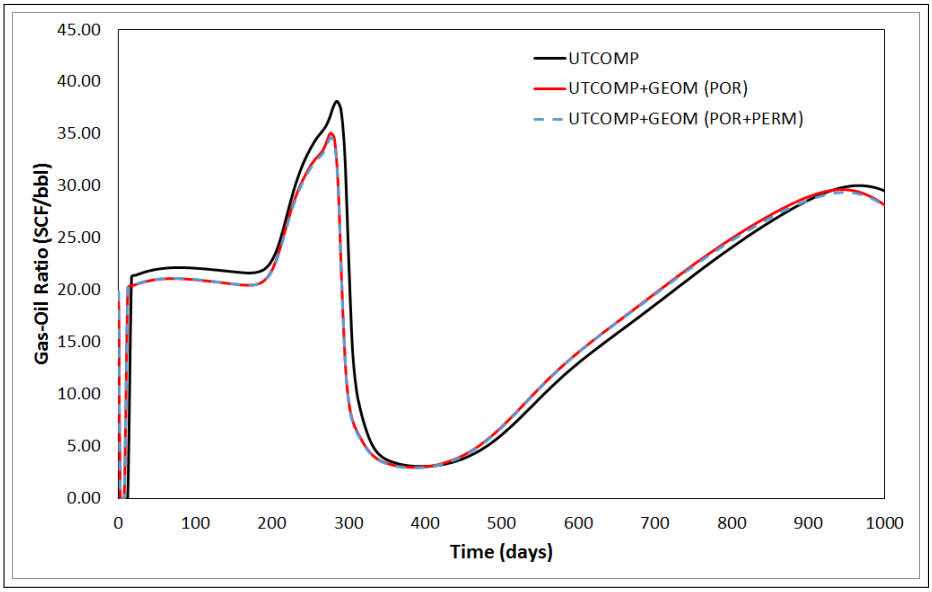

Source: Prepared by the author.

5.2.4 Water injection with single pseudocomponent fluid

This case presents a waterflood process, another common secondary recovery method. Water is injected into the reservoir to provide the pressure gradient necessary to drive the oil towards the production well. The main purpose for presenting this case is to compare the implementation presented in this work to another geomechanical approach applied in UTCOMP-RS developed by Haddad (2017). This approach employs a Finite Element discretization for the geomechanical model and the Finite Volume Method for the fluid flow model, only allowing the use of three-dimensional cartesian grids.

The fluid and reservoir properties used for this case are the same ones used by Haddad (2017) and are presented in Table 11. The only exception is the permeability coupling exponent, n, which is equal to the unity. In the original work, the value used is 15, but instabilities were found as this value was set in the current implementation. Using $n = 1$ denotes a linear variation of permeability with respect to porosity, as expressed by Eq. (3.88). Oscillations in the production curves, as will be presented further on, were reduced.

The original case is modeled in a three-dimensional cartesian 7x7x3 grid. Since the implementation presented in this work only supports a two-dimensional X-Z model, as presented previously, the grid used will differ from the one used by Haddad (2017). While maintaing the number of cells used along the X and Z directions (7 and 3, respectively), the reservoir will be represented by one single cell along the Y direction. This might incur in differences in the

simulation results in relation to the original solution, but still can be used as basis of comparison between implementations.

Table 11 – Physical properties for the water injection case

Property	Symbol	Value	Unit
Simulation time	t	2000.0	days
Reservoir height	H	600.0	ft
Reservoir length	L	350.0	ft
Reservoir thickness	D	350.0	ft
Applied stress	σ_0	2500	Pa
Porosity	ϕ_o	0.3	-
Absolute permeability	k	100	md
Initial water saturation	S_w	0.2	-
Reservoir fluid composition	z_j	100% C_{10}	-
Water viscosity	μ_w	1.0	cP
Water density	ρ_w	62.343	lb/ft^3
Initial pressure	P	600	psi
Production well bottom-hole pressure	P_{bh}	600	psi
Injection well water flow rate	$q_{w,I}$	400 0	STB/day
Young's modulus	E	8.96×10^7	Pa
Poisson's ratio	ν	0.3	-
Biot-Willis coefficient	α	0.79	-
Permeability coupling exponent	n	1	-

Source: Author.

Figure 33 shows the results for oil production rates for the EbFVM and FEM implementations. Again, the coupling was treated in two different situations: first by considering only porosity as coupling parameter and then considering both porosity and permeability. The results show a common behavior between curves for both implementations. As posed before, the different grid setup can be responsible, at least partially, for the discrepancy in results between implementations. The use of a smaller permeability coupling exponent, as previously described, in order to mitigate oscillations in the production curve, also results in discrepancies with respect to the FEM implementation curves. Figure 34 shows the comparison of results for cumulative oil production, in which a similar behavior as previously described is seen.

Figure 33 – Oil production rates results for waterflooding case.

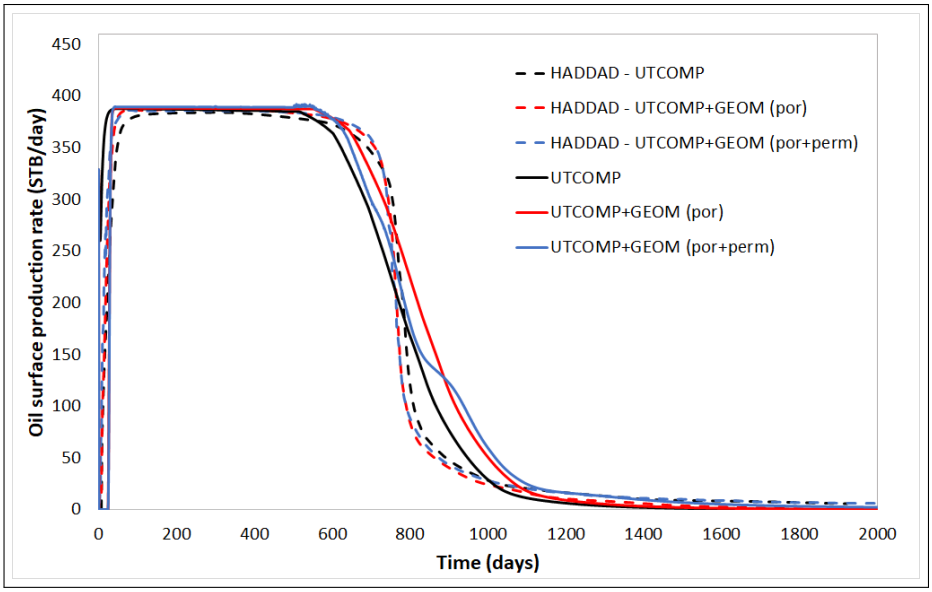

Source: Prepared by the author.

Figure 34 – Cumulative oil production results for waterflooding case.

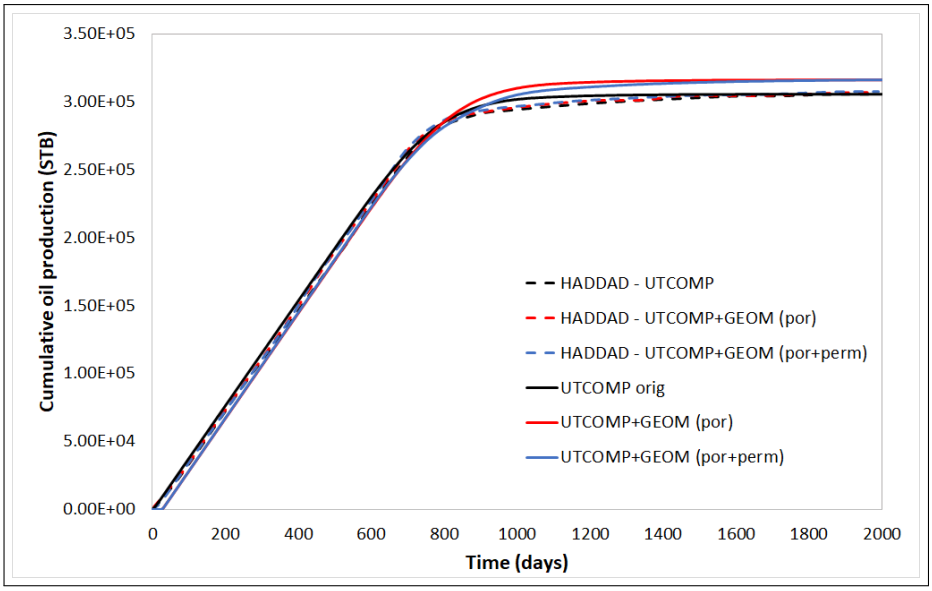

Source: Prepared by the author.

6 CONCLUSIONS

This work has presented the implementation of a coupled geomechanical model with a compositional reservoir simulator using unstructured grids and the EbFVM approach. The fluid flow model is based on the original UTCOMP-RS model, proposed by Chang (1990), and further adapted for EbFVM. The geomechanical model is based on the traditional Biot theory, using a linear elastic constitutive relationship.

After applying a set of constraining hypotheses, both models had their mathematical descriptions presented in its entirety. Then, the equations were discretized through the EbFVM, that, by accommodating for unstructured grids, presents a higher flexibility in terms of grids than the traditional Finite Volume Method, while maintaining its conservative aspect. The explicit and iterative coupling algorithms were also presented as means to link the solution of the two models. While the explicit method presents a simpler implementation and less computational load, its results might present some inaccuracy in some cases. The iterative approach tends to yield generally more accurate, in spite of its inferior performance.

In the results presented in this work, two validation cases were provided. For the Terzaghi problem, results for pressure and displacement *versus* time show a match between analytical and numerical results. The results for the Mandel case are still not desirable. The evolution of, pressure, vertical total stress and displacement with time show the expected behavior, although the values simulation results do not match the analytical solution. One possible cause might be related to a incorrect treatment of the boundary open to the atmosphere. Since this boundary condition is not supported by UTCOMP-RS, it is being emulated by placing a production well operating at zero bottom-hole pressure at the boundary nodes. This includes more variables into the model, since well indexes must be calculated. Further investigation is required in order to work around this issue to closely resemble the open boundary of the Mandel case.

The case studies presented one primary depletion case and two secondary recovery processes, namely, gas and water injection. The cases used either 3-pseudocomponent or 6-pseudocomponent fluid mixtures, showing the capability of the coupled code to handle multicomponent and multiphase situations. In all cases, the coupled solution was presented and compared to the original UTCOMP-RS solution, in terms of oil recovery factor and average reservoir pressure. The coupled results presented a similar curve behavior to the uncoupled one, with slight differences due to the addition of the geomechanical effect. For the gas injection

cases, the comparison was extended to the oil and gas production curves and gas-oil ratio, with results behaving as expected. The increase in oil recovery in both cases for the coupled solution can be attributed to the compaction drive effect, in which the reduction in pore volume drives the fluid out towards the production well, leading to a more optimistic solution. When the permeability variation was also considered, no noticeable change was seen in comparison to the porosity-only coupling. As far as the water injection case is concerned, its goal was to compare the current implementation to another geomechanical coupling approach used in conjunction with UTCOMP-RS that used a Finite Element discretization for geomechanical equations. The results for both implementations showed acceptable similarities in their behaviors, given that, while the current implementation only allows for X-Y two-dimensional domains, the FEM implementation used a three-dimensional grid.

6.1 Future work

Further improvements to the model regard the addition of support to three-dimensional grids, as only two-dimensional X-Z cross sections models are accepted now. This would allow for a more realistic and accurate studies of the coupled phenomenon. Another way to enhance the geomechanical model would be to include different constitutive equations, such as the Mohr-Coulomb, Tresca and Drücker-Prager models, that include analysis of plasticity and structural failure. In certain conditions of rock properties, plasticity might be a likely issue, especially in situations where subsidence might occur, creating environmental danger and possible damage to surface facilities.

Adding the possibility of modelling the geomechanics of the cap rock surrounding the reservoir could also make the coupled analysis more realistic. The cap rock is normally composed of different sediments in relation to the reservoir, consequently having different mechanical properties. The degree of discrepancy between cap and reservoir rock properties can lead to different behavior of pressure and stress.

REFERENCES

ABOUSLEIMAN, Y.; CHENG, A. H.-D.; CUI, L.; DETOURNAY, E.; ROEGIERS, J.-C. Mandel's problem revisited. **Géotechnique**, v. 46, n. 2, p. 187–195, 1996.

ABUSHAIKHA, A. S.; VOSKOV, D. V.; TCHELEPI, H. A. Fully implicit mixed-hybrid finite-element discretization for general purpose subsurface reservoir simulation. **Journal of Computational Physics**, v. 346, p. 514–538, 2017.

ACS, G.; DOLESCHALL, S.; FARKAS, E. General purpose compositional model. **SPE Journal**, v. 25, p. 543–553, 1985.

BABAZADEH, M.; MCCLURE, M. Coupling fluid flow and geomechanics in a three-dimensional discrete fracture network simulator. In: **49th US Rock Mechanics Symposium**. San Francisco, USA: American Rock Mechanics Association, 2015.

BALIGA, B.; PATANKAR, S. A new finite-element formulation for convection-diffusion problems. **Numerical Heat Transfer, Part B: Fundamentals**, v. 4, n. 3, p. 393,409, 1980.

BIOT, M. A. General theory of three-dimensional consolidation. **Journal of Applied Physics**, v. 12, n. 2, p. 155–164, 2 1941.

____. Theory of elasticity and consolidation for a porous anisotropic solid. **Journal of Applied Physics**, v. 26, n. 2, p. 182–185, 2 1955.

____. Theory of deformation of a porous viscoelastic anisotropic solid. **Journal of Applied Physics**, v. 27, n. 5, p. 459–467, 5 1956.

____. Mechanics of deformation and acoustic propagation in porous media. **Journal of Applied Physics**, v. 33, n. 4, p. 1482–1498, 4 1962.

____. Nonlinear and semilinear rheology of porous solids. **Journal of Geophysical Research**, v. 78, n. 4, p. 4924–4937, 8 1973.

BIOT, M. A.; WILLIS, D. G. The elastic coefficients of the theory of consolidation. **Journal of Applied Mechanics**, v. 1, n. 24, p. 594–601, 12 1957.

BRAND, C.; HEINEMANN, J.; AZIZ, K. The grid orientation effect in reservoir simulation. In: **SPE Symposium in Reservoir Simulation**. Anaheim, USA: Society of Petroleum Engineers, 1991.

BUCKLEY, S.; LEVERETT, M. Mechanism of fluid displacement in sands. **Transactions of the AIME**, v. 146, n. 1, p. 107–116, 1942.

CHANG, Y.-B. **Development and Application of an Equation of State Compositional Simulator.** 1990. 502 f. Tese (PhD in Petroleum Engineering) — Department of Petroleum and Geosystems Engineering, The University of Texas at Austin, Austin, Texas, 1990.

CHIN, L.; RAGHAVAN, R.; THOMAS, L. Fully coupled geomechanics and fluid-flow analysis of wells with stress-dependent permeability. In: **1998 SPE International Conference and Exhibition**. Beijing, China: Society of Petroleum Engineers, 1998a.

____. Fully coupled analysis of well responses in stress-sensitive reservoirs. In: **1998 SPE Annual Technical Conference and Exhibition**. New Orleans, USA: Society of Petroleum Engineers, 1998b.

CHIN, L.; THOMAS, L.; SYLTE, J.; PIERSON, R. Iterative coupled analysis of geomechanics and fluid flow for rock compaction in reservoir simulation. **Oil & Gas Science and Technology**, v. 57, n. 5, p. 485–497, 2002.

CHO, D.; MUTUAL, E.; NORTON, M.; MILLER, D.; MCHARG, D. Estimation of the biot-willis coefficient via rock-physics inversion. In: **SEG Technical Program Expanded Abstracts**. [*S. l.*: Society of Exploration Geophysicists, 2016.

CORDAZZO, J. **Simulação de reservatórios de petróleo utilizando o método EbFVM e multigrid algébrico.** 2006. 272 f. Tese (Doutorado em Engenharia Mecânica) — Programa de Pós-Graduação em Engenharia Mecânica, Universidade Federal de Santa Catarina, Florianópolis, 2006.

COUSSY, O. A general theory of thermoporoelastoplasticity for saturated porous materials. **Transport in Porous Media**, v. 4, n. 3, p. 281–293, 6 1989.

CRYER, C. A comparison of the three-dimensional consolidation theories of Biot and Terzaghi. **The Quarterly Journal of Mechanics and Applied Mathematics**, v. 16, n. 4, p. 401–412, 1963.

DONEA, J.; HUERTA, A. **Finite Element Methods for Flow Problems**. Chichester: Wiley, 2003.

DRUCKER, D.; PRAGER, W. Soil mechanics and plasticity analysis of limit design. **Quarterly Journal of Applied Mathematics**, v. 10, p. 157–162, 1952.

FERNANDES, B. R. B. **Implicit and Semi-implicit techniques for the petroleum reservoir simulation based on volume balance.** 2014. 169 f. Dissertação (Mestrado em Engenharia Química) — Programa de Pós-Graduação em Engenharia Química, Universidade Federal do Ceará, Fortaleza, 2014.

FORSYTH, P. A. A control-volume, finite element method for local mesh refinement. **SPE Reservoir Engineering**, v. 7, n. 4, p. 561–566, 1990.

FUNG, L.-K.; HIEBERT, A.; NGHIEM, L. Reservoir simulation with a control-volume finite element method. **SPE Reservoir Engineering**, v. 5, n. 3, p. 349–357, 1992.

FUSSELL, L.; FUSSELL, D. An iterative technique for compositional reservoir models. **Society of Petroleum Engineers Journal**, v. 19, n. 4, p. 211–220, 1979.

GAI, X. **A coupled geomechanics and reservoir flow model on parallel computers.** 2004. 239 f. Tese (PhD in Petroleum Engineering) — Department of Petroleum and Geosystems Engineering, The University of Texas at Austin, Austin, Texas, 2004.

GEERSTMA, J. The effect of fluid pressure decline on volumetric changes of porous rocks. **Petroleum Transactions, AIME**, v. 210, p. 331–340, 3 1957.

GHABOUSSI, J.; WILSON, E. L. Flow of compressible fluid in porous elastic media. **International Journal for Numerical Methods in Engineering**, v. 5, n. 3, p. 419–442, 1 1973.

GIBSON, R. E.; KNIGHT, K.; TAYLOR, P. W. A critical experiment to examine theories of three-dimensional consolidation. **Proceedings of the European Conference on Soil Mechanics, Wiesbaden**, v. 1, p. 69–76, 1963.

GUTIERREZ, M.; LEWIS, R. The role of geomechanics in reservoir simulation. In: **SPE/IRSM Rock Mechanics in Petroleum Engineering**. Trondheim, Norway: Society of Petroleum Engineers, 1998.

HADDAD, M. **Simulation and production evaluation of multiple-stage hydraulic fracturing in horizontal wellbores.** 2017. 630 f. Tese (PhD in Petroleum Engineering) — Department of Petroleum and Geosystems Engineering, The University of Texas at Austin, Austin, Texas, 2017.

HADDAD, M.; SEPEHRNOORI, K. Development and validation of an explicitly coupled geomechanics module for a compositional reservoir simulator. **Journal of Petroleum Science and Engineering**, v. 149, p. 281–291, 2017.

HERMANSEN, H. e. a. Twenty five years of Ekofisk reservoir management. In: **SPE Annual Technical Conference and Exhibition**. San Antonio, Texas: Society of Petroleum Engineers, 1997. p. 873 – 885.

IOGNA, A.; GUILLET-LHERMITE, J.; WOOD, C.; DEFLANDRE, J. co_2 storage and enhanced gas recovery: using extended black oil modelling to simulate co_2 injection on a North Sea depleted gas field. In: **SPE Europec featured at 79th EAGE Conference and Exhibition**. Paris, France: Society of Petroleum Engineers, 2017.

KHOSHKBARCHI, M.; KOHSE, B.; SAAF, F. Black oil modeling in a next-generation integrated production simulator. In: **SPE Reservoir Simulation Symposium**. Houston, USA: Society of Petroleum Engineers, 2015.

LEE, S.; WHEELER, M. F.; WICK, T. Iterative coupling of flow, geomechanics and adaptive phase-field fracture including level-set crack width approaches. **Journal of Computational and Applied Mathematics**, v. 314, p. 40–60, 2017.

LEI, Q.; LATHAM, J.-P.; TSANG, C.-F. The use of discrete fracture networks for modelling coupled geomechanical and hydrological behaviour of fractured rocks. **Computers and Geotechnics**, v. 85, p. 151–176, 2017.

LEWIS, R.; SUKIRMAN, Y. Finite element modelling of three-phase flow in deformed saturated oil reservoirs. **International Journal for Numerical and Analytical Methods in Geomechanics**, v. 17, n. 8, p. 577–598, 8 1993.

LOHRENZ, J.; BRAY, B. G.; CLARK, C. R. Calculating viscosities of reservoir fluids from their compositions. **Journal of Petroleum Technology**, v. 16, n. 10, p. 1171–1176, 1964.

MALISKA, C. R. **Transferência de Calor e Mecânica dos Fluidos Computacional**. Florianópolis: LTC, 2004.

MANDEL, J. Consolidation des sols (Étude mathématique). **Géotechnique**, v. 3, n. 7, p. 287–299, 1953.

MARCONDES, F.; SANTOS, L.; VARAVEI, A.; SEPEHRNOORI, K. A 3d hybrid element-based finite-volume method for heterogeneous and anisotropic compositional reservoir simulation. **Journal of Petroleum Science and Engineering**, v. 108, p. 342–351, 2013.

MARCONDES, F.; SEPEHRNOORI, K. An element-based finite-volume method approach for heterogeneous and anisotropic compositional reservoir simulation. **Journal of Petroleum Science and Engineering**, v. 73, n. 1, p. 99–106, 2010.

MISES, R. von. Mechanik der festen körper im plastiche-deformablen zustand. **Nachrichten von der Gesellschaft der Wissenschaften zu Göttingen, Mathematisch-Physikalische Klasse**, v. 1, p. 582–592, 1913.

MOINFAR, A.; NARR, W.; HUI, M.-H.; MALLISON, B. T.; LEE, S. H. Comparison of discrete-fracture and dual-permeability models for multiphase flow in naturally fractured reservoirs. In: **SPE Reservoir Simulation Symposium**. The Woodlands, USA: Society of Petroleum Engineers, 2011.

MORADI, M.; SHAMLOO, A.; DEZFULI, A. D. A sequential implicit discrete fracture model for three-dimensional coupled flow-geomechanics problems in naturally fractured porous media. **Journal of Petroleum Science and Engineering**, v. 150, p. 312–322, 2017.

MUSKAT, M. **Physical Principles of Oil Production**. New York: McGraw-Hill, 1949.

NOLEN, J. Numerical simulation of compositional phenomena in petroleum reservoirs. In: **SPE symposium on numerical simulation of reservoir performance**. Houston, USA: Society of Petroleum Engineers, 1973.

PAN, F. **Development and application of a coupled geomechanics model for a parallel compositional reservoir simulator.** 2009. 351 f. Tese (PhD in Petroleum Engineering) — Department of Petroleum and Geosystems Engineering, The University of Texas at Austin, Austin, Texas, 2009.

PATANKAR, S. V. **Numerical Heat Transfer and Fluid Flow**. [*S. l.*: McGraw-Hill, 1980.

PEACEMAN, D. W. **Fundamentals of Numerical Reservoir Simulation**. New York: Elsevier, 1977.

____. Interpretation of well-block pressures in numerical reservoir simulation. **Society of Petroleum Engineers Journal**, v. 18, n. 1, p. 183–194, 1978.

____. Interpretation of well-block pressures in numerical reservoir simulation with nonsquare grid blocks and anisotropic permeability. **Society of Petroleum Engineers Journal**, v. 23, n. 3, p. 531–543, 1983.

PENG, D.-Y.; ROBINSON, D. B. A new two-constant equation of state. **Industrial & Engineering Chemistry Fundamentals**, v. 15, n. 1, p. 59–64, 1976.

RIBEIRO, G. G. **Volumes finitos baseado em elementos para problemas de poroelasticidade.** 2016. 230 f. Tese (Doutorado em Engenharia Mecânica) — Programa de Pós-Graduação em Engenharia Mecânica, Universidade Federal de Santa Catarina, Florianópolis, 2016.

RICE, J. R.; CLEARY, M. P. Some basic stress diffusion solutions for fluid-saturated elastic porous media with compressible constituents. **Reviews of Geophysics and Space Physics**, v. 14, n. 1, p. 227–241, 5 1976.

ROEBUCK, I. The compositional reservoir simulator: case I - the linear model. **Society of Petroleum Engineers Journal**, v. 9, n. 1, p. 115–130, 1969.

ROZON, B. A generalized finite volume discretization method for reservoir simulation. In: **SPE Symposium on Reservoir Simulation**. Houston, USA: Society of Petroleum Engineers, 1989.

SCHIFFMANN, R. L. Field applications of soil consolidation under time-dependent loading and varying permeability. **Highway Research Board Bulletin**, v. 1, n. 248, p. 1–25, 1960.

SETTARI, A.; MOURITS, F. A coupled reservoir and geomechanical solution system. **SPE Journal**, v. 3, n. 3, p. 219–226, 1998.

SETTARI, A.; WALTERS, D. A. Advances in coupled geomechanical and reservoir modeling with applications to reservoir compaction. **SPE Journal**, v. 6, n. 3, p. 334–342, 2001.

SMALL, J.; BOOKER, J.; DAVIS, E. Elasto-plastic consolidation of soil. **International Journal of Solids and Structures**, v. 12, n. 6, p. 431–448, 1976.

SOUZA NETO, E. de; PERIC, D.; OWEN, D. **Computational Methods for Plasticity: Theory and Applications**. United Kingdom: John Wiley & Sons, 2008.

STONE, H. L. Estimation of three-phase permeability and residual oil data. **Journal of Canadian Petroleum Technology**, v. 12, n. 1, p. 53–61, 1973.

SULAK, R.; DANIELSEN, J. Reservoir aspects of Ekofisk subsidence. In: **Offshore Technology Conference**. , Houston, Texas: Society of Petroleum Engineers, 1988. p. 9 – 21.

SULAK, R.; THOMAS, L.; BOADE, R. 3D reservoir simulation of Ekofisk compaction drive. **Journal of Petroleum Technology**, v. 43, n. 10, p. 1272–1278, 10 1991.

TARAHHOM, F. **Development of an implicit full-tensor dual porosity compositional reservoir simulator.** 2008. 273 f. Tese (PhD in Petroleum Engineering) — Department of Petroleum and Geosystems Engineering, The University of Texas at Austin, Austin, Texas, 2008.

TERZAGHI, K. **Theoretical Soil Mechanics**. New York: John Wiley & Sons, 1943.

THOMAS, L.; CHIN, L.; PIERSON, R.; SYLTE, J. Coupled geomechanics and reservoir simulation. In: **2002 SPE Annual Technical Conference and Exhibition**. San Antonio, USA: Society of Petroleum Engineers, 2003.

TONELLI, R. **Estratégias para o tratamento do acoplamento escoamento/geomecânica utilizando volumes finitos.** 2016. 202 f. Dissertação (Mestrado em Engenharia Mecânica) — Programa de Pós-Graduação em Engenharia Mecânica, Universidade Federal de Santa Catarina, Florianópolis, 2016.

TORTIKE, W.; ALI, S. F. A framework for multiphase nonisothermal fluid flow in a deforming heavy oil reservoir. In: **SPE Symposium on Reservoir Simulation**. [*S. l.*: Society of Petroleum Engineers, 1987.

TRAN, D.; NGHIEM, L.; BUCHANAN, L. Aspects of coupling between petroleum reservoir flow and geomechanics. In: **43rd US Rock Mechanics Symposium**. Asheville, USA: American Rock Mechanics Association, 2009.

TRESCA, H. Mémoire sur l'écoulement des corps solides soumis à de fortes pressions. **Comptes rendus de l'Académie des Sciences**, v. 59, p. 754, 1864.

VALE, B. T. do. **Implementação do modelo de fratura discreta na simulação de reservatórios naturalmente fraturados utilizando o método de volumes finitos baseado em elementos (EbFVM)** 2014. 112 f. Dissertação (Mestrado em Engenharia Mecânica) — Programa de Pós-Graduação em Engenharia Mecânica, Universidade Federal de Santa Catarina, Florianópolis, 2014.

VERRUIJT, A. Elastic storage of aquifers. In: WIEST, R. D. (Ed.). **Flow through porous media**. New York: Academic Press, 1969. cap. 8, p. 331–376.

____. **Computational Geomechanics**. Derdrecht: Springer, 1995.

WANG, C.; WU, Y.-S.; XIONG, Y.; WINTERFELD, P. H.; HUANG, Z. Geomechanics coupling simulation of fracture closure and its influence on gas production in shale gas reservoirs. In: **SPE Reservoir Simulation Symposium**. Houston, USA: Society of Petroleum Engineers, 2015.

WANG, H. F. **Theory of Linear Poroelasticity with Applications to Geomechanics and Hydrogeology**. Princeton: Princeton University Press, 2000.

ZIENKIEWICZ, O.; TAYLOR, R. **The Finite Element Method:** Volume 1: The Basis. Oxford: Butterworth-Heinemann, 2000.

ZOBACK, M. D. **Reservoir Geomechanics**. New York: Cambridge University Press, 2007.

APPENDIX A – ANALYTICAL SOLUTIONS FOR VALIDATION CASES

This appendix aims to present the algebraic equations that provide the analytical solutions for the two validation cases used in this work. The equations are presented in a direct manner, omitting their detailed derivation. Such details are readily available in the referenced literature.

A.1 Terzaghi problem

The solutions presented for the one-dimensional consolidation case express the behavior of pressure and vertical displacement as functions of column height and time, $P(y,t)$ and $u_y(y,t)$, respectively. The derivation of the solutions are demonstrated by Wang (2000).

Considering a column of height H, on top of which is applied a constant load of magnitude σ_0. The pressure at the initial equilibrium condition will be

$$P(y,0) = \gamma\sigma_0, \tag{A.1}$$

in which γ is given by

$$\gamma = \frac{B(1+\nu_u)}{3(1-\nu_u)}. \tag{A.2}$$

In the equation above, ν_u is the undrained Poisson's ratio and B is the Skempton coefficient. According to Wang (2000), this coefficient measures the how the applied load is distributed between the fluid and the porous medium. Consequently, it is a function of the rock and fluid properties. In this work, the rock properties were modeled after a Berea sandstone, whose properties are listed by Wang (2000).

The solution for pressure is then given by

$$P(y,t) = \frac{4\gamma\sigma_0}{\pi}\sum_{j=0}^{\infty}\frac{1}{2j+1}\exp\left[\frac{-(2j+1)^2\pi^2 ct}{4H^2}\right]\sin\left[\frac{(2j+1)\pi y}{2H}\right], \tag{A.3}$$

in which c is the consolidation coefficient:

$$c = \frac{3k\gamma K(1+\nu)}{\mu\alpha(1-\nu)}, \tag{A.4}$$

in which K is the drained bulk modulus, a intrinsic characteristic of the solid medium.

The vertical displacement at the initial equilibrium state is determined by

$$u_y(y,0) = u_{y,0} = \frac{\sigma_0(1+\nu_u)(H-y)}{3K_u(1-\nu_u)}, \tag{A.5}$$

where K_u is the undrained bulk modulus.

The solution for vertical displacement is given by

$$\begin{aligned} u_y(y,t) = u_{y,0} + \frac{\gamma\sigma_0\alpha(1+\nu)}{3K(1-\nu)}\Bigg\{(H-y) - \frac{8H}{\pi^2}\sum_{j=0}^{\infty}\frac{1}{(2j+1)^2} \\ \exp\left[\frac{-(2j+1)^2\pi^2 ct}{4H^2}\right]\cos\left[\frac{(2j+1)\pi y}{2H}\right]\Bigg\}. \end{aligned} \tag{A.6}$$

A.2 Mandel problem

For this case, analytical solutions are presented for pressure, vertical and horizontal displacements and vertical total stress, as functions of time and space. Despite the case being presented in a two-dimensional domain, each variable is function of only one spatial dimension. Pressure, vertical stress and horizontal displacement vary along the X-axis, while vertical displacement only varies along the Y-axis. The derivation of the expressions for each variable are presented in detail by Abousleiman *et al.* (1996). For a reservoir of length L with a constant force F applied to its top boundary, pressure is given by

$$P(x,t) = \frac{2FB(1+\nu_u)}{3L}\sum_{j=0}^{\infty}\left\{\frac{\sin A_j}{A_j - \sin A_j\cos A_j}\left[\cos\left(\frac{A_j x}{L}\right) - \cos A_j\right]\exp\left(\frac{A_j^2 ct}{L^2}\right)\right\}, \tag{A.7}$$

vertical total stress is given by

$$\begin{aligned} \sigma_{yy}(x,t) = \frac{2F(\nu_u-\nu)}{L(1-\nu)}\sum_{j=0}^{\infty}\left[\frac{\sin A_j}{A_j - \sin A_j\cos A_j}\cos\left(\frac{A_j x}{L}\right)\exp\left(\frac{A_j^2 ct}{L^2}\right)\right] - \\ \frac{F}{L} + \frac{2F}{L}\sum_{j=0}^{\infty}\left[\frac{\sin A_j\cos A_j}{A_j - \sin A_j\cos A_j}\exp\left(\frac{A_j^2 ct}{L^2}\right)\right], \end{aligned} \tag{A.8}$$

horizontal displacement is given by

$$u_x(x,t) = \left\{ \frac{F\nu}{2\mu_l L} - \frac{F\nu_u}{\mu_l L} \sum_{j=0}^{\infty} \left[\frac{\sin A_j \cos A_j}{A_j - \sin A_j \cos A_j} \exp\left(\frac{A_j^2 ct}{L^2} \right) \right] \right\} x + \frac{F}{\mu_l} \sum_{j=0}^{\infty} \left[\frac{\cos A_j}{A_j - \sin A_j \cos A_j} \sin\left(\frac{A_j x}{L} \right) \exp\left(\frac{A_j^2 ct}{L^2} \right) \right], \tag{A.9}$$

and, finally, vertical displacement is expressed as

$$u_y(y,t) = \left\{ \frac{F(1-\nu_u)}{\mu_l L} \sum_{j=0}^{\infty} \left[\frac{\sin A_j \cos A_j}{A_j - \sin A_j \cos A_j} \exp\left(\frac{A_j^2 ct}{L^2} \right) \right] - \frac{F(1-\nu)}{2\mu_l L} \right\} y. \tag{A.10}$$

In the equations above, A_j represents each value in the set of roots of the equation

$$\frac{\tan A_j}{A_j} = \frac{1-\nu}{\nu_u - \nu}. \tag{A.11}$$

In Eq. A.11, the roots were determined numerically. The number of roots obtained was large enough to minimize oscillations and inaccuracies in the calculation of the analytical solutions to the model.